

MOLECULAR LEVEL INSIGHTS INTO CARBON CAPTURE AT LIQUID  
SURFACES

by

LAURA ELLEN MCWILLIAMS

A DISSERTATION

Presented to the Department of Chemistry and Biochemistry  
and the Graduate School of the University of Oregon  
in partial fulfillment of the requirements  
for the degree of  
Doctor of Philosophy

June 2016

DISSERTATION APPROVAL PAGE

Student: Laura Ellen McWilliams

Title: Molecular Level Insights into Carbon Capture at Liquid Surfaces

This dissertation has been accepted and approved in partial fulfillment of the requirements for the Doctor of Philosophy degree in the Department of Chemistry and Biochemistry by:

Marina G. Guenza	Chair
Geraldine L. Richmond	Advisor
Michael E. Kellman	Core Member
Paul J. Wallace	Institutional Representative

and

Scott L. Pratt	Dean of the Graduate School
----------------	-----------------------------

Original approval signatures are on file with the University of Oregon Graduate School.

Degree awarded June 2016

© 2016 Laura Ellen McWilliams

## DISSERTATION ABSTRACT

Laura Ellen McWilliams

Doctor of Philosophy

Department of Chemistry and Biochemistry

June 2016

Title: Molecular Level Insights into Carbon Capture at Liquid Surfaces

Implementing effective and environmentally responsible carbon capture technologies is one of the principle challenges of this century. Successful implementation requires a host of engineering advancements, but also a fundamental understanding of the underlying physics, chemistry, and materials science at play in these highly complex systems. A large body of scholarship examines both current technologies as well as future strategies, but to date little exploration of the surface behavior of these systems has been examined. As these carbon capture systems involve uptake of gaseous CO<sub>2</sub> to either aqueous or solid substrates, understanding the chemistry and physics governing the boundary between the two reactant phases is critical. Yet probing the unique chemistry and physics of these interfacial systems is very difficult.

This dissertation addresses this knowledge gap by examining the surface chemistry of monoethanolamine and CO<sub>2</sub>. Monoethanolamine is a simple organic amine currently used in small scale CO<sub>2</sub> scrubbing, and acts as an industrial benchmark for CO<sub>2</sub> capture efficiency. The studies presented throughout this dissertation employ surface selective techniques, including vibrational sum frequency

spectroscopy, surface tensiometry, and computation methodologies, in order to determine the behavior governing aqueous amine interfaces.

The adsorption behavior and surface orientation of aqueous monoethanolamine is examined first. The results show monoethanolamine is present at the surface, highly ordered, and solvated. Perturbations to this amine surface from gaseous  $\text{CO}_2$  and  $\text{SO}_2$ , as well as from liquid  $\text{HCl}$ , are examined in the remainder of the dissertation. Reactions between the amine and acids are shown to cause immediate changes to the interface, but the interface then remains largely unaffected as further reaction evolves. The studies presented herein provide a needed exploration of the interfacial picture of these highly reactive systems, with implications for future carbon capture materials and design.

This dissertation includes both previously published and forthcoming co-authored material.

## CURRICULUM VITAE

NAME OF AUTHOR: Laura Ellen McWilliams

### GRADUATE AND UNDERGRADUATE SCHOOLS ATTENDED:

University of Oregon, Eugene, OR  
Banaras Hindu University, Varanasi, UP, India  
Lyon College, Batesville, AR

### DEGREES AWARDED:

Doctor of Philosophy, Chemistry, 2016, University of Oregon  
Master of Science, Chemistry, 2012, University of Oregon  
Bachelor of Science, Chemistry, 2007, Lyon College

### AREAS OF SPECIAL INTEREST:

Atmospheric Chemistry  
Carbon Capture  
Physical Chemistry  
Spectroscopy  
Surface Science

### PROFESSIONAL EXPERIENCE:

Research Assistant, Richmond Laboratory, University of Oregon, Eugene, OR,  
2011–present

Graduate Teaching Assistant, Physical Chemistry Laboratory, University of  
Oregon, Eugene, OR, 2010–2011

Forensic Toxicologist, Arkansas State Crime Laboratory, Little Rock, AR, 2009–  
2010

Environmental Chemistry REU, University of Notre Dame, Notre Dame, IN,  
2006

## GRANTS, AWARDS AND HONORS:

National Energy and Technology Laboratory Grant, “Using Vibrational Sum Frequency Spectroscopy to Unlock the Mechanisms of Carbon Capture,” URS subcontract/task release number RES1100425/005, 2013.

## PUBLICATIONS:

McWilliams, L. E., Valley, N. A., Wren, S. N., and Richmond, G. L. A Means to an Interface: Investigating Monoethanolamine Behavior at an Aqueous Surface. *Phys. Chem. Chem. Phys.* **2015**, *17*, 21458–21469.

Wren, S. N., Gordon, B. P., Valley, N. A., McWilliams, L. E. and Richmond, G. L. Hydration, Orientation, and Conformation of Methylglyoxal at the Air–Water Interface. *J. Phys. Chem. A* **2015**, *119*, 6391–6403.

Valley, N. A., Blower, P. G., Wood, S. R., Plath, K. L., McWilliams, L. E. and Richmond, G. L. Doubling Down: Delving into the Details of Diacid Adsorption at Aqueous Surfaces. *J. Phys. Chem. A* **2014**, *118*, 4778–4789.

## ACKNOWLEDGEMENTS

The immense gratitude I feel for everyone that supported me during this work, both in big and small ways, cannot be adequately expressed. I cherish the relationships formed during graduate school, and am so fortunate to have so many to acknowledge. Firstly, I am grateful to my advisor Dr. Geraldine Richmond. Geri, you were supportive, kind, and generous during one of the toughest times of my life. I can never thank you enough for your care and mentorship throughout. You were also a huge support throughout grad school, helping shape the way I think about science and guiding me to see the bigger picture. I especially thank you for creating a lab community I care for immensely and to whom I am so proud to belong.

To the lab—I am lucky to call myself a member alongside you all. Dr. Stephanie Ota, my mentor and friend, was and remains a huge inspiration both personally and professionally. I learned more in the two years I worked under her than any others; most importantly she taught me to cherish morning yoga, hot Toshi's in August, and exercise ball office chairs. I am forever in her debt. Katy and Cruise, Stephanie, ERo, Sumaloom, Nevada, JetStar, Branditoburrito, ACarp, Reginald, Bri, Cliven, The Generator, and Amelia—you have been and always will be family to me. I am lucky to have such a supportive, energetic, and caring group of coworkers. Priscilla and Shiloh—I honestly can't thank you enough. You keep the lab running, keep us accountable and sane. And, of course, my office mate of three years, Dr. Nick Valley—you were my guide through many of the challenging aspects of my research. Moreover, you somehow convinced me that computational approaches were the path forward. I both hate, and am so grateful, that you somehow manage to be right about everything.



To my committee members—thank you for your continued support and genuine interest in my future success. To Dr. Larry Scatena—thank you for being generous with your time, an excellent sounding board for my roadblocks, and for always advocating for my well-being. To Kris, John, and Jeffrey in the machine shop and Cliff in the electronics shop—thank you for your help with all of my experimental challenges, but especially for your incredible patience and skill. To Denise Stewart—for your transparency and calm, thank you for making the painful reality of working in a construction zone more bearable. To the Women in Graduate Science—thank you for being a support network, professional resource, and genuine great time. Kate, Kara, Fern, Matt, Brandon—thank you for striving with me to make this STEM workplace a little more equitable, and for being great friends throughout.

I want to especially thank my friends and family outside of the university. To Dr. Grafton and the Lyon College community—thank you for encouraging me to strive harder and not be satisfied with the status quo. I would never have considered the possibility of grad school had it not been for your encouragement and endless letters of recommendation. To the McWilliamses, Pyles, Curls and Lachmans both near and far—thank you for showing sincere interest in my happiness and my work, and for keeping life in perspective. Mom—you instilled in me a desire and excitement for learning, and provided the tools to be successful. You will always be my best teacher. And Jove—I cannot succinctly describe how grateful I am for all that you do and who you are. Know that my well of gratitude is bottomless, and that because of you, I will always cherish this time of my life.

This research was supported in part by the National Energy and Technology Laboratory, URS subcontract/task release number RES1100425/005, and by a grant from the National Science Foundation, CHE-1051215.

For Jove

## TABLE OF CONTENTS

Chapter	Page
I. INTRODUCTION . . . . .	1
II. BACKGROUND AND THEORY OF SURFACE TECHNIQUES . . . . .	6
Vibrational Sum Frequency Generation . . . . .	8
Computational Methodology . . . . .	15
Wilhelmy Plate . . . . .	17
Conclusions . . . . .	21
III. EXPERIMENTAL CONSIDERATIONS . . . . .	22
Vibrational Sum Frequency Spectroscopy . . . . .	23
Computational Methodology . . . . .	37
Wilhelmy Plate . . . . .	40
Sample Preparation . . . . .	41
Gas Flow Parameters . . . . .	42
Conclusions . . . . .	42
IV. THE VAPOR/WATER INTERFACE . . . . .	43
The Neat Air/Water Interface . . . . .	44
Changes to the Vapor/Water Interface . . . . .	49
Conclusions . . . . .	53

Chapter	Page
V. BEHAVIOR OF MEA AT THE VAPOR/WATER INTERFACE . . . . .	55
Introduction . . . . .	55
MEA Spectral Response . . . . .	56
Spectral Assignments: Comparison of VSF Spectra . . . . .	60
Surface Population Analysis . . . . .	68
Molecular Orientational Analysis . . . . .	72
Conclusions . . . . .	77
VI. BEHAVIOR OF MEA AT THE ACIDIFIED WATER INTERFACE . . .	79
Introduction . . . . .	79
Experimental MEH Surfaces . . . . .	81
Computed MEH Surfaces . . . . .	87
Conclusions . . . . .	91
VII. SURFACE BEHAVIOR OF MEA-CO <sub>2</sub> . . . . .	93
Introduction . . . . .	93
Surface Dynamics During CO <sub>2</sub> Uptake to MEA . . . . .	97
MEA-CO <sub>2</sub> Spectral Response . . . . .	100
Assignment of 1563 cm <sup>-1</sup> Feature . . . . .	105
Computed Carbamic Acid (CBA) . . . . .	108
Conclusions . . . . .	112
VIII. PRELIMINARY STUDIES: SURFACE BEHAVIOR OF MEA-SO <sub>2</sub> . . .	115
Introduction . . . . .	115
MEA-SO <sub>2</sub> Spectra . . . . .	118

Chapter	Page
Comparing Surface Impact of SO <sub>2</sub> and CO <sub>2</sub> . . . . .	121
Conclusions . . . . .	122
IX. CONCLUSIONS . . . . .	124
APPENDICES	
A. FITTING PARAMETERS FOR WATER . . . . .	127
B. FITTING PARAMETERS FOR MEA STUDIES . . . . .	129
C. FITTING PARAMETERS FOR CO <sub>2</sub> UPTAKE . . . . .	131
D. DIHEDRAL MATCHES FROM MD TO DFT . . . . .	132
REFERENCES CITED . . . . .	134

## LIST OF FIGURES

Figure	Page
1. Schematic of VSF propagation where interfacial plane is $xy$ , and the plane of propagation is $xz$ (highlighted in green). . . . .	10
2. Plot of susceptibility in $xxz$ of the SS-CH <sub>2</sub> (red, filled circles) and AS-CH <sub>2</sub> (blue, open circles) at varying degrees of molecular tilt ( $\theta$ ) . . . . .	14
3. Representative Wilhelmy plate used in surface tension studies. . . . .	18
4. Simplified schematic of the laser system used for sum frequency spectroscopy, with inset of vertical breadboard. Incident beam angles at interface are visible = 45° and IR = 60°. Red lines indicate visible beam, blue lines indicate infrared beam, while the dark green lines indicate the sum frequency beam. . . . .	24
5. Schematic of the acquisition optics used for sum frequency spectroscopy (10e – side in Figure 4). Incident angles are visible = 45° and IR = 60° (not shown). The dashed, solid and dotted green lines represent different SF beam paths depending on the frequency of the infrared input. The inset shows the output SF spot (IR=7.1 μm, Vis=800 nm) directed through a spectrometer, revealing two distinct frequencies. . . . .	29
6. Schematic of the experimental cell used during gas flow studies. . . . .	32
7. Non-resonant SF response off a gold substrate in dried air (black), in CO <sub>2</sub> (red triangles) and in SO <sub>2</sub> (gold dots). The intensity of the gold response in the bending region has been increased by 10. . . . .	34
8. Characteristic IR absorbances of water (black) and polystyrene (red) used to calibrate the VSF data. . . . .	35
9. Representative water box used in MD studies. . . . .	38
10. VSF spectra in the vibrational stretching region of the neat air/water interface (black) at incident angles visible=45° and IR=60° (top) and visible=63° and IR=55° (bottom). Resonant mode fits shown in green (free OH), purple (companion OH), and light and dark blue (tetrahedrally coordinated water); the non resonant contributions to the spectra are shown in orange. . . . .	45

Figure	Page
11. VSF spectra in the vibrational bending region of the neat air/water interface shown in black with resonant mode fits as the solid black line (total) with fit components in blue (coordinated OH), green (free OH), and red (librational water motions) in both the <i>ssp</i> (top) and <i>sps</i> (bottom) polarization schemes . . . . .	48
12. VSF spectra in the vibrational stretching (a, c) and bending (b, d) regions of the vapor/water interface, with the neat air/water spectra shown in grey and in an acidic gas environment in red (CO <sub>2</sub> ; a, b) and orange (SO <sub>2</sub> ; c, d)	51
13. VSF spectra of 1 M NaHCO <sub>3</sub> (pink) from 1300–1800 cm <sup>-1</sup> (top), and magnified around the yellow box to 1500–1800 cm <sup>-1</sup> (bottom). The neat water spectrum (grey) is shown for reference. . . . .	52
14. MEA . . . . .	56
15. VSF spectra of aqueous monoethanolamine solutions at the air-water interface acquired using the <i>ssp</i> -polarization scheme in the CH/OH stretching region. Experimental data (shapes) and corresponding fits (solid lines) are offset for clarity. . . . .	57
16. VSF spectra in <i>ssp</i> -polarization of 10 M MEA solution (green) and neat water (grey). Correctly acquired VSF data (top) and VSF data convoluted with an IR+IR+vis response (bottom) are offset for clarity. The dotted vertical lines act as visual guides for MEA resonant modes. . . . .	59
17. VSF spectra of 10 M MEA solutions in <i>ssp</i> - (purple, diamonds) and <i>sps</i> -polarization (teal, circles) in the CH stretching region. Experimental data (open shapes) and corresponding fits (solid lines) are shown. Incident beam angles for both polarizations were 63°(visible) and 55°(IR). . . . .	62
18. VSF spectra in the bending region in <i>ssp</i> -polarization of 10 M MEA (green, bottom), 10 M EDA (teal, middle), and 10 M ETG (orange, top) with their representative structures on the left. Experimental data (shapes) and corresponding fits (solid lines) are shown with individual component fits. The component fits arising from the water modes have been removed for clarity. . . . .	64
19. VSF spectra in <i>ssp</i> -polarization taken experimentally (blue) and calculated (orange) in (a) the bending region, (b) the CH stretching region, and (c) the NH stretching region. Note, the y-axes for (a), (b), and (c) are not comparable, but are scaled to allow calculated spectra to be observed. Dotted orange lines represent conformer contributions to the overall calculated VSF spectra. . . . .	66

Figure	Page
20. Computed (bottom) and experimental (top) VSF spectra of 10 M MEA solution in <i>ssp</i> -polarization in the bending region. Bottom: computed spectra show total in black with conformer contributions highlighted in color. Top: experimental spectra and total fit in grey, the total fit from only resonant modes in black, and components to the fits are colored. . . . .	67
21. Surface pressure versus bulk concentration of MEA, with concentrations of VSF spectra from Figure 15 colored. . . . .	69
22. Density profile of water (grey dashed line) and $\sim 10$ M MEA (green solid line) extracted after 52 ns of simulation time. . . . .	71
23. Correlated angular distributions in the bulk and surface region of $\sim 10$ M MEA probing (a) the backbone orientation ( $\theta$ vs $\phi$ ) and (b) the $\text{NH}_2$ orientation ( $\beta$ vs $\alpha$ ). The color guides on the left describe the $z$ -axis, where cooler colors equate to lower percent of total population while warmer colors equate to higher percent of total population. . . . .	73
24. Angular distribution of $\sim 10$ M MEA methylene bisector in both the bulk (red dashed) and at the surface (blue solid) averaged over all methylene twists. . . . .	75
25. Generalized picture of MEA's surface orientation and conformation. Angles for $\sim 10$ M MEA solution are shown. . . . .	76
26. Percent change in concentration of MEA (green triangles) and MEH (yellow circles) with changing pH based on Equation 6.1. . . . .	80
27. VSF spectra in <i>ssp</i> -polarization of 10 M MEA in water (green) and 10 M MEA in HCl (gold) in the bending (a) and stretching (b) regions. Experimental data (shapes) and corresponding fits (solid lines) are shown. . . . .	82
28. VSF spectra of 10 M MEA in water (green) and 10 M MEA in HCl (gold) in <i>ssp</i> -polarization in the CH stretching region. The red arrows indicate the spectral changes observed upon acidification. . . . .	85
29. Density profile of water (grey dashed line) and $\sim 1$ M MEH (gold solid line) extracted after 50 ns of simulation time. The $\sim 10$ M MEA (green solid line) from Figure 22 is shown for reference. . . . .	88
30. VSF spectra of MEH in <i>ssp</i> -polarization taken experimentally (gold) and calculated (purple) in (a) the bending region and (b) the CH stretching region. The green trace is experimental VSF of 10 M MEA. Note, the $y$ -axes for (a) and (b) are not comparable, but are arbitrarily scaled so that calculated spectra may be observed. . . . .	89



Figure	Page
31. Generalized picture of MEA and MEH surface orientation and conformation. Representative angles for $\sim 10$ M MEA and $\sim 1$ M MEH. Note: MEH's C–O and C–N angles may reverse at the depth shown. . . . .	90
32. Structures of molecules examined in this chapter. CBA = carbamic acid; MEA = monoethanolamine; CBM = carbamate; and MEH = protonated MEA . . . . .	96
33. Surface pressure of 10 M MEA vs. time under CO <sub>2</sub> exposure (red) alongside the change in solution pH during reaction (green). Vertical lines are error bars at $\pm 1\sigma$ from the average. . . . .	98
34. VSF spectra in <i>ssp</i> -polarization of 10 M MEA (bottom, green) during reaction with CO <sub>2</sub> (2nd, pink, $\sim 3$ hours; 3rd, red, $\sim 15$ hours), and after CO <sub>2</sub> (top, blue) has been purged and the reaction ceased. The neat water surface (grey) is shown in the bottom spectra for reference. Experimental data (shapes) and corresponding fits (solid lines) are shown. The spectra are offset for clarity. . . . .	101
35. VSF spectra in <i>ssp</i> -polarization of 10 M MEA (bottom, green) during reaction with CO <sub>2</sub> (2nd, pink, $\sim 3$ hours; 3rd, red, $\sim 15$ hours), and after CO <sub>2</sub> (top, blue) has been purged and the reaction ceased. The neat water surface (grey) is shown in the bottom spectra for reference. Experimental data (shapes) and corresponding fits (solid lines) are shown. The spectra are offset for clarity. . . . .	103
36. VSF spectra in the bending region in <i>ssp</i> -polarization of 10 M MEA (green, bottom) and 10 M MEA after reaction with CO <sub>2</sub> (blue, top). Experimental data (shapes) and corresponding fits (solid lines) are shown with individual component fits. The component fits arising from the water modes have been removed for clarity. . . . .	105
37. CBA (top) and BOC (bottom) . . . . .	105
38. VSF spectra in <i>ssp</i> -polarization of 5 M BOC (yellow). The 10 M MEA (green) and 10 M MEA post-CO <sub>2</sub> (blue) spectra are shown for reference. . . . .	106
39. VSF spectra in the bending region in <i>ssp</i> -polarization of 10 M MEA after reaction with CO <sub>2</sub> in H <sub>2</sub> O (dark blue) and D <sub>2</sub> O (teal). Experimental data (shapes) and corresponding fits (solid lines) are shown. . . . .	107
40. Density profile of water (grey dashed line) and $\sim 1$ M CBA (blue) extracted after 54 ns of simulation time. The $\sim 10$ M MEA (green) density from Figure 22 is shown for reference. . . . .	108

Figure	Page
41. Computed VSF spectra of CBA in <i>ssp</i> -polarization (middle traces, blue) in the (a) bending region and (b) CH stretching region. The dark blue trace at top is the experimental VSF spectra of post-CO <sub>2</sub> exposure MEA solution, with component fits shown in light blue. The green, bottom trace is the computed ~10 M MEA spectra for reference. The spectra have been off-set for clarity, and the y-axes for (a) and (b) are not comparable. . . . .	110
42. Generalized picture of ~1 M CBA surface orientation in the top surface (left) and in the more coordinated surface (right). . . . .	111
43. Depiction of the evolution of aqueous MEA surfaces in the presence of CO <sub>2</sub> . 1. MEA at the vapor/water interface. 2. Exposure to CO <sub>2</sub> results in CO <sub>2</sub> reacting with water and MEA to form CBM, MEH, and CBA. 3. The charged species (CBM and MEH) retreat from the surface while CBA remains. 4. After CO <sub>2</sub> flow ceases, the CBA remains at (or migrates to) the surface. . . . .	114
44. Possible SO <sub>2</sub> —MEA products <sup>1</sup> . . . . .	117
45. VSF spectra in the (a) bending region and (b) stretching region in <i>ssp</i> -polarization of 10 M MEA (bottom, green) during reaction with SO <sub>2</sub> (middle, yellow), and after SO <sub>2</sub> (top, blue) has been purged and the reaction ceased. The neat water surface (grey) is shown in the bottom spectra for reference. Experimental data (open shapes) and corresponding fits (solid lines) are shown. The spectra are offset for clarity. . . . .	119
46. VSF spectra in the (a) bending region and (b) stretching region in <i>ssp</i> -polarization of 10 M MEA after reaction with SO <sub>2</sub> (teal) and after reaction with CO <sub>2</sub> (dark blue). Experimental data (open shapes) and corresponding fits (solid lines) are shown. . . . .	122

## LIST OF TABLES

Table	Page
1. Elements of $\chi_{i,j,k}^{(2)}$ at a $C_\infty$ surface with xy interfacial plane, and their unique polarization counterparts in VSF spectroscopy. . . . .	11
2. Frequencies and assignments of peaks from experimental and calculated <i>ssp</i> VSF spectra. Experimental frequencies are from global fits of <i>ssp</i> spectra taken at incident angles 45° (visible) and 60° (IR). Calculated frequencies are anharmonic VPT2 frequencies calculated at the B2PLYP/6-311++G (2d,2p) level of theory. Fits to water resonances are not included for clarity.	61
3. Frequencies and assignments of peaks from experimental <i>ssp</i> VSF spectra for MEA and acidified MEA. . . . .	84
4. Frequencies and assignments of peaks from experimental <i>ssp</i> VSF spectra. Experimental frequencies are from global fits of spectra taken at incident angles 45° (visible) and 60° (IR). All frequencies are $\text{cm}^{-1} \pm 10 \text{ cm}^{-1}$ . . .	102
5. Frequencies, gaussian widths, and assignments of peaks from experimental <i>ssp</i> VSF spectra at incident angles 45° (visible) and 60° (IR). . . . .	127
6. Frequencies, gaussian widths, and assignments of peaks from experimental <i>ssp</i> VSF spectra at incident angles 63° (visible) and 55° (IR). . . . .	127
7. Frequencies, gaussian widths, and assignments of peaks from experimental <i>sps</i> VSF spectra at incident angles 63° (visible) and 55° (IR). . . . .	128
8. Frequencies, gaussian widths, and assignments of peaks from experimental <i>ssp</i> VSF spectra of <b>10 M MEA</b> at incident angles 45° (visible) and 60° (IR). . . . .	129
9. Frequencies, gaussian widths, and assignments of peaks from experimental <i>ssp</i> VSF spectra of <b>10 M EDA</b> at incident angles 45° (visible) and 60° (IR).	130
10. Frequencies, gaussian widths, and assignments of peaks from experimental <i>ssp</i> VSF spectra of <b>10 M ETG</b> at incident angles 45° (visible) and 60° (IR).	130
11. Frequencies, gaussian widths, and assignments of peaks from experimental <i>sps</i> VSF spectra of <b>10 M MEA</b> in CH region at incident angles 63° (visible) and 55° (IR). . . . .	130

Table	Page
12. Frequencies, gaussian widths, and assignments of peaks from experimental <i>ssp</i> VSF spectra of <b>10 M MEA with CO<sub>2</sub></b> at incident angles 45° (visible) and 60° (IR). . . . .	131
13. DFT structures and energies calculated at B3LYP/6-311++G(2d,2p) level of theory for <b>~10 M MEA</b> . Conformer ranges for MD simulations that matched the DFT structures. . . . .	132
14. DFT structures and energies calculated at B3LYP/6-311++G(2d,2p) level of theory for <b>~1 M MEH</b> . Conformer ranges for MD simulations that matched the DFT structures. . . . .	132
15. DFT structures and energies calculated at B3LYP/6-311++G(2d,2p) level of theory for <b>~1 M CBM</b> . Conformer ranges for MD simulations that matched the DFT structures. . . . .	133
16. DFT structures and energies calculated at B3LYP/6-311++G(2d,2p) level of theory for <b>~1 M CBA</b> . Conformer ranges for MD simulations that matched the DFT structures. . . . .	133

# CHAPTER I

## INTRODUCTION

Carbon dioxide has long been implicated in climate change. CO<sub>2</sub>, along with methane and nitrous oxide, accounts for ~80% of the total global warming effects from atmospheric gases.<sup>2</sup> CO<sub>2</sub> concentrations have risen steeply since the 1750s, reaching an average rate of 2 ppm per year for the last decade.<sup>3</sup> This level of atmospheric CO<sub>2</sub> exceeds any measured level for the last several hundreds of thousands of years, with this increase arising primarily from fossil fuel burning and land use changes.<sup>4-7</sup> Fossil fuels currently supply ~85% of U.S. energy consumption,<sup>8</sup> ensuring their use—and continued exhaust of CO<sub>2</sub>—in the near future. Thus technologies capable of removing CO<sub>2</sub> efficiently and economically from fossil fuel exhaust streams are critical.<sup>9</sup>

Current strategies for combating this CO<sub>2</sub> increase involve changes to our energy, transportation, building, and farming sectors, including reducing our reliance on fuel-powered cars, designing more energy efficient buildings, and shifting to “greener” fuels such as solar, wind, or nuclear. Most of these strategies, however, will require decades-long policies to shift cultural, economic, and societal norms. In the near future, carbon capture and storage (CCS) technologies have been proposed to reduce CO<sub>2</sub> emissions. CCS technologies involve capturing CO<sub>2</sub> before it is released into the atmosphere, then storing it for later use. While many CCS technologies exist, post-combustion CO<sub>2</sub> capture is considered more economically feasible and scalable.<sup>10,11</sup>

Post-combustion CCS involves capturing CO<sub>2</sub> from the exhaust of a fuel combustion process. These technologies are typically designed to retrofit existing infrastructure. The classic example of a post-combustion strategy is scrubbing CO<sub>2</sub> from power plant exhaust. The majority of global CO<sub>2</sub> emissions arise from stationary

sources,<sup>4</sup> with  $\sim 60\%$  of global  $\text{CO}_2$  emissions arising from fewer than 8,000 locations, over half of which are power plants.<sup>3</sup> Recent studies, in fact, have projected a reduction of over 350 Mt of  $\text{CO}_2$  emissions per year by 2030 if CCS were used by 2020 in the US alone.<sup>3</sup> This is a projected decrease of  $\sim 4\%$  of the global annual  $\text{CO}_2$  emissions achievable solely by the US sector in under a decade.

At present, aqueous amines are a leading candidate for CCS post-combustion scrubbing processes.<sup>11</sup> The scrubbers exploit an exothermic ( $\Delta H_f \sim -7.1$  kcal/mol)<sup>12</sup> reaction between gaseous  $\text{CO}_2$  and aqueous amines to generate carbamate or carbamic acid products. The amines are commonly introduced to the gaseous exhaust stream as an aqueous spray, reacting with  $\text{CO}_2$ . The  $\text{CO}_2$ -amine reaction product remains in the aqueous phase, which is then collected and sent to a heater. In the heater, the  $\text{CO}_2$  is separated from the amine, allowing the amine to then be recycled into the exhaust stream for continued use.<sup>10</sup>

Monoethanolamine (“MEA”;  $\text{HO}(\text{CH}_2)_2\text{NH}_2$ ), a small organic amine, is the current benchmark molecule for post-combustion CCS.<sup>13</sup> MEA is a well-established technology, having been used in the natural gas industry for decades.<sup>3,10</sup> Since CCS technologies are projected, on the outside, to quadruple the cost of electricity from existing US power plants,<sup>3</sup> cheaper, well-established, and reliable technologies are primary targets for larger scale use such as implementation in coal-fired power plants. Despite its prominence, MEA has a number of shortcomings, including corrosiveness and the energy required to remove  $\text{CO}_2$ , that make its current implementation in power plants prohibitive.<sup>6,8,11</sup>

Ultimately, a fundamental understanding of the physical and chemical components in an aqueous amine system is necessary for successful design, development, and scaling of future post-combustion CCS technologies. Yet

surprisingly few studies have examined the molecular level effects of even the most well established technologies. In fact, even fewer studies have considered the role of the solution surface in CO<sub>2</sub> capture. This is a major shortcoming in the literature due to the strong surface-activity of these amines, and the fact that the CCS reaction requires gas exchange across an interface. A few notable examples exist, such as the Lewis, et al. study of CO<sub>2</sub>-treated MEA surfaces that suggests different bulk vs. surface behavior of reactants and products,<sup>14</sup> or the Niedermaier, et al. study of ionic liquids that shows different chemistry with CO<sub>2</sub> at the surface compared to the bulk.<sup>15</sup> Yet these studies indicate that CO<sub>2</sub>-amine surface chemistry is not only necessary but also largely unexamined.

The experiments described in this dissertation seek to probe the fundamental chemistry involved in amine-CO<sub>2</sub> surface interactions. Specifically, the surface behavior of MEA will be examined in aqueous environments and under varying degrees of acidification. These studies will seek to understand the behavior and presence of MEA at aqueous interfaces, the conditions that favor or discourage CO<sub>2</sub> adsorption to aqueous MEA surfaces, the similarities between CO<sub>2</sub> and SO<sub>2</sub> surface chemistry with MEA, and the role and response of the surface before, during, and after reaction. Understanding the fundamentals of the MEA system establishes a molecular-level picture of a carbon-capture system, with implications for improving efficiency, scalability, and enhanced performance of future technologies.

Moreover, understanding the aqueous behavior, preference, and chemistry of these amines at environmental surfaces is critical as their increased usage warrants concern regarding their own environmental presence. It has been suggested that current CCS strategies will result in 40-160 tons of amines to be emitted each year for each power plant that currently emits ~1 million tons of CO<sub>2</sub>.<sup>16</sup> This increase in

atmospheric amines will have enormous implications for the chemistry, lifetimes, and dynamics of atmospheric species. This impact will be especially felt in the condensed phase, where these alkali amines are likely to reside. Therefore an understanding of the surface preference and behavior of MEA has implications not only in carbon-capture technologies, but also in the atmospheric systems CO<sub>2</sub> scrubbing seeks to manage.

This dissertation focuses on surface specific experiments capable of probing aqueous interfaces. Surface tensiometry, computational methodology, and vibrational sum frequency spectroscopy (VSFS) are used to directly probe MEA surfaces under gaseous CO<sub>2</sub> or SO<sub>2</sub> exposure. Chapters II and III detail these techniques, providing a framework for the remaining dissertation. Chapter IV details the neat water interface, its behavior, interpretation, and changes upon perturbation with CO<sub>2</sub> or SO<sub>2</sub>. Understanding this simpler system helps instruct the more complicated interpretation of the MEA system, and provides the foundation for all subsequent aqueous phase studies.

Chapter V details the neat MEA surface, its speciation, adsorption and orientation. VSFS, surface tension, and computational techniques are all employed to characterize MEA at an aqueous surface. The MEA system is also used to evaluate the data extracted from computational methods with those determined experimentally. The bending region of the vibrational spectrum is assessed, and much detail is provided to properly identify peaks in this poorly defined region. The details of this chapter have previously published.<sup>17</sup> Dr. Sumi Wren and Dr. Nicholas Valley aided in the initial stages of this work, but all experiments, computational work, and interpretation were conducted independently.



Chapter VI examines how the MEA surface changes with decreasing pH, as a comparison to the spectral changes examined during acidification with CO<sub>2</sub> in Chapter VII. These experiments help distinguish spectral changes in the CO<sub>2</sub> system from changes arising from the overall solution pH. The surface tension experiments and a portion of the computational experiments for this chapter were conducted by Nina Vincent. This work will be included with Chapter VII in a future publication.

Chapter VII details the reaction of the aqueous MEA surface with gaseous CO<sub>2</sub>. The role and behavior of MEA during reaction, the characterization of reaction products both during and after reaction, and the interpretation of the spectral changes observed throughout are examined by these studies. Ultimately, through a combination of the above-mentioned experimental techniques, a clear picture of MEA-CO<sub>2</sub> at the surface is generated. This work will be submitted for a future publication, with the computational studies of MEA-CO<sub>2</sub> product species begun by Dr. Nicholas Valley.

Chapter VIII examines the MEA surface upon exposure to SO<sub>2</sub> gas. SO<sub>2</sub> is known to have high affinities for water surfaces, and is a common contaminant in flue gas systems resulting in much faster quenching of CO<sub>2</sub> uptake by amines.<sup>18</sup> Moreover, SO<sub>2</sub> shows unique behavior at aqueous surfaces forming surface complexes with both water and organics.<sup>19,20</sup> Contrasting the CO<sub>2</sub> and SO<sub>2</sub> uptake studies allows for a deeper understanding of the surface chemistry at play within CCS systems. This work will be submitted in a future communication.

Chapter IX provides an overview of the MEA system with an outlook for future work. The picture of aqueous MEA under CO<sub>2</sub> and SO<sub>2</sub> will be used to evaluate current CCS strategies, with suggestions for future fundamental science.

## CHAPTER II

### BACKGROUND AND THEORY OF SURFACE TECHNIQUES

While most chemistry can be well described by bulk-phase properties and macroscopic phenomenon, the interface holds many unique traits that necessitate close examination apart from bulk-phase behavior. For example, simple surfactants are known to adsorb to interfaces and display high surface concentrations, despite being miscible in the bulk solute. Similarly, as will be discussed in Chapter IV, air/water interfaces display unique hydrogen bonding environments compared to the bulk solution; this aqueous interface can induce unique orientation and speciation of solutes, unique chemistry of both solvent and solute, and unique reaction dynamics compared to what dominates in the bulk. It is therefore necessary to study surface phenomenon in systems where such uniqueness may play a role.

The studies of this dissertation focus on aqueous monoethanolamine (MEA) and its reaction with gaseous acids at the air/liquid interface. MEA is a surface active organic, as will be shown in Chapter V, meaning it displays higher surface concentrations relative to the bulk. Yet MEA occupies a large interfacial footprint, allowing water molecules to also reside at the surface and participate in surface chemistry. MEA's orientation at the air/water interface is constrained, induced by preferred solvation of its hydrophilic functional groups. Thus aqueous MEA surfaces are quite unique from their bulk. Moreover, the systems herein involve uptake of acidic gases to this MEA surface. As surface MEA is the first line of interaction during the absorption of these gaseous species, it's reasonable to assume the chemistry that occurs at the surface could govern or influence the chemistry that dominates the bulk. Understanding the surface behavior of MEA and its reaction products before

and after reaction, the dynamics of surface speciation and behavior, and the broader implications for surface-dominated carbon capture systems (i.e. amine-functionalized MOFs, membrane contractors, etc.) is the focus of this dissertation. Thus, it is crucial to accurately probe these surfaces in real-time and under realistic conditions.

Few can sensitively probe molecular properties at an interface, although many techniques exist to study chemistry in the bulk. Surface tensiometry, which probes adsorbate surface concentration and packing, has been in analytical use for over a century, but is largely governed by macroscopic dynamics. Extraction of molecular detail from surface tension data is based on varying assumptions that often are unsuitable once reactions or multiple surface species are considered. Surface spectroscopies such as second harmonic generation and surface enhanced Raman have been used extensively since the introduction of reliable pulsed laser systems, and provide molecular-level detail of surface systems. Vibrational sum frequency spectroscopy (VSFS), a similar process to second harmonic generation, is also ideal for studying molecular interfacial properties, and enables direct probing of vibrational transitions that elucidate molecular identities, orientations and binding environments of surface species. However, as a coherent phenomenon, VSF spectral contributions can be very difficult to deconvolve, and often rely on elegant experimental techniques (i.e. polarization manipulation, precise deuteration) to fully elucidate changes in spectra. This is especially true for reacting systems where reactions and products have similar and overlapping vibrational signatures. In such cases, computational modeling of the surface system is employed to allow for comparison with and clarification of the surface spectroscopy.

The systems studied in this dissertation are examined using a combination of surface tensiometry, VSF spectroscopy, and computational methodology in order to

accurately describe the surface behavior and reactions at play. This chapter will detail the necessary theory that governs these surface techniques, while the subsequent chapter will detail the experimental considerations necessary for implementation. The fundamentals of vibrational sum frequency generation will be briefly detailed in this chapter; although the interested reader is directed to the exhaustive description of VSF at liquid surfaces present in the literature.<sup>21–26</sup> A description of calculating molecular orientation from VSF spectra is also provided. The current computational methodology employed herein and the current state of the field of calculating VSF spectra is discussed. The chapter ends with a discussion of fundamentals of surface tension via the Wilhelmy plate method.

### **Vibrational Sum Frequency Generation**

Spectroscopic techniques take advantage of light’s ability to interact with a material. When light encounters a material, the material’s outermost electrons can be influenced by the light’s electric field ( $\mathbf{E}$ ), creating an induced dipole in the material that oscillates at the same frequency as the light. These collective induced dipoles can have an additive effect in the condensed phase, such that a polarization ( $\mathbf{P}$ )—or dipole moment per unit volume—may be considered.

$$\mathbf{P} = \epsilon_0 \chi^{(1)} \mathbf{E} \tag{2.1}$$

$\chi^{(1)}$  is the condensed phase average of the material’s electrons’ polarizabilities, called the susceptibility, and  $\epsilon_0$  is the vacuum permittivity. In traditional, linear spectroscopies, like IR or Raman, Equation (2.1) accurately describes the system. However, in the presence of very large  $\mathbf{E}$ , such as found in pulsed laser systems,

nonlinear contributions to Equation (2.1) are no longer negligible, and an expansion to higher orders is necessary to accurately characterize the system polarization.

$$\mathbf{P} = \epsilon_0(\chi^{(1)}\mathbf{E} + \chi^{(2)}\mathbf{E}^2 + \chi^{(3)}\mathbf{E}^3 + \dots + \chi^{(n)}\mathbf{E}^n) = \mathbf{P}^{(1)} + \mathbf{P}^{(2)} + \mathbf{P}^{(3)} + \dots + \mathbf{P}^{(n)} \quad (2.2)$$

This linear expansion of  $\mathbf{P}$  shows that in high intensity laser fields, oscillation of molecular dipoles can occur at frequencies of higher-orders than the incident field. This phenomenon is the origin of VSF, which arises from the  $\mathbf{P}^{(2)}$  term in Equation 2.2 and is thusly called a “second-order” process.

In second-order processes where the system  $\mathbf{E}$  arises from the sum of two incident fields of different frequencies,  $\mathbf{E}(\omega_1)$  and  $\mathbf{E}(\omega_2)$ , the second-order polarization may be expressed as

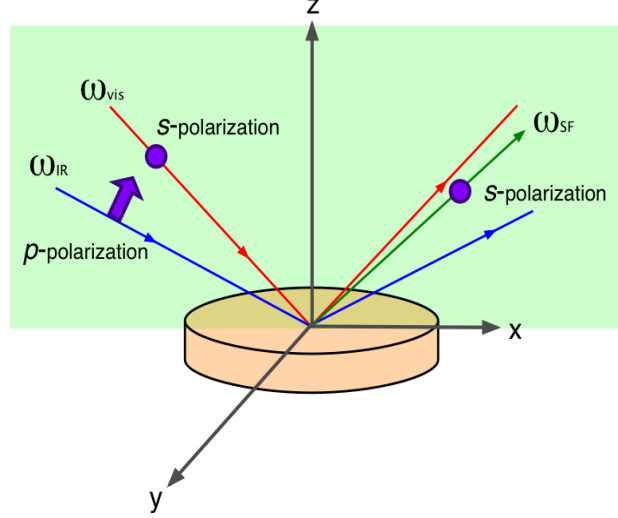
$$\mathbf{P}^{(2)} = \epsilon_0\chi^{(2)}(\mathbf{E}_1\cos \omega_1t + \mathbf{E}_2\cos \omega_2t)^2 \quad (2.3)$$

given a frequency dependence in  $\mathbf{E}$  equal to  $\mathbf{E}_1\cos \omega t$ . An expansion of the square in Equation (2.3) gives rise to terms describing constant DC fields, second harmonic generation, difference frequency generation, and sum frequency generation.<sup>21</sup> Although these second-order processes may occur concurrently, this dissertation focuses on sum frequency generation, and specifically *vibrational* sum frequency generation (VSF), where the incident  $\mathbf{E}$  field arises from the sum of a visible ( $\omega_{vis}$ ) and tunable infrared ( $\omega_{IR}$ ) beam.

In VSF, incident visible and infrared beams overlap at an interface generating an output beam (SF), as shown in Figure 1. At liquid surfaces where the interfacial plane is the xy plane, the z-axis can be described as having  $C_\infty$  symmetry, simplifying the coordinate space such that  $x = -x$ ,  $y = -y$ , but  $z \neq -z$ . We can broadly describe the susceptibility from Equation (2.3) in terms of this coordinate system as  $\chi_{i,j,k}^{(2)}$ .

Due to the symmetry of the surface the tensor  $\chi_{i,j,k}^{(2)}$  does not equal  $\chi_{-i,-j,-k}^{(2)}$  or  $-\chi_{i,j,k}^{(2)}$ . This detail is subtle but substantial in its significance to VSF spectroscopy.

In bulk media  $\chi_{i,j,k}^{(2)}$  and its inverse must be equivalent; the only condition where this equivalency holds is when  $\chi_{i,j,k}^{(2)} = 0$ . Thus in bulk media, the  $\chi_{i,j,k}^{(2)}$  term, and thereby the sum frequency process, generates no response. At the surface, however, where  $\chi_{i,j,k}^{(2)} \neq \chi_{-i,-j,-k}^{(2)}$ , a non-zero result can define  $\chi_{i,j,k}^{(2)}$  such that a non-negligible SF response arises. This



is the origin of the surface-selectivity of VSF spectroscopy, ensuring its usefulness in studying buried or complex interfaces whose responses would otherwise be lost to the bulk response.

Moreover, this symmetry consideration of the surface allows for constraint of the  $\chi_{i,j,k}^{(2)}$  term. As shown in Equation (2.3),  $\chi^{(2)} = \frac{1}{\epsilon_0} \mathbf{P}^{(2)}(\mathbf{E}(\omega_1) + \mathbf{E}(\omega_2))^{-2}$ . Since  $\mathbf{P}^{(2)}$ ,  $\mathbf{E}(\omega_1)$ , and  $\mathbf{E}(\omega_2)$  are vectors,  $\chi^{(2)}$  has  $3^3$  elements. This element count reduces considerably in light of the surface symmetry condition to four unique elements, as shown in Table 1. By changing the incident polarization of the visible and IR beams, and detecting a specific polarization of the SF response, the various elements of  $\chi_{i,j,k}^{(2)}$  may be probed. In Table 1 these elements are shown with their corresponding experimental VSF polarization counterpart. Experimental polarization designations are given to the incident and outgoing beams in energetic order: SF, visible, IR. For

TABLE 1. Elements of  $\chi_{i,j,k}^{(2)}$  at a  $C_\infty$  surface with xy interfacial plane, and their unique polarization counterparts in VSF spectroscopy.

Elements of $\chi_{i,j,k}^{(2)}$	VSF polarization (SF, vis, IR)
$\chi_{x,x,z}^{(2)} = \chi_{y,y,z}^{(2)}$	<i>ssp</i>
$\chi_{x,z,x}^{(2)} = \chi_{y,z,y}^{(2)}$	<i>sps</i>
$\chi_{z,x,x}^{(2)} = \chi_{z,y,y}^{(2)}$	<i>pss</i>
$\chi_{z,z,z}^{(2)}$	<i>ppp</i>

the interfacial geometry employed throughout this dissertation, and discussed in detail in the next chapter, *p*-polarized light oscillates parallel to the xz propagation plane while *s*-polarized light oscillates perpendicular, as shown in Figure 1. Polarizations such as *ssp* and *sps* are common in VSFS, and will be mentioned throughout this dissertation. Simplistically, these polarization schemes designate probing dipole moments in the plane of the interface (*sps*) and those components normal to the interface (*ssp*) such that information regarding surface orientation may be elucidated.

### *Molecular Orientation Analysis*

More quantitative methods for detailing the surface orientation of molecules may be employed by examining the molecular symmetry of the surface species. Several papers detail this analysis in greater detail and for several molecular symmetry groups.<sup>27-31</sup> Generally, symmetry arguments are employed to reduce the  $\chi_{i,j,k}^{(2)}$  expressions. By then examining ratios of the amplitudes of different contributing modes (or of the same mode in different experimental polarizations), a molecular orientation relative to surface normal may be extracted. But before this ratio comparison can be done, an accounting of the molecular symmetry contributions

$(\beta_{i,j,k}^{(2)})$  in relation to the macroscopic  $\chi_{i,j,k}^{(2)}$  is required. As an example of such analysis, the methylene ( $\text{CH}_2$ ) modes will be discussed.

The intensity of VSF light generated at the surface is proportional to the incident intensities and the square of the effective  $\chi^{(2)}$

$$I_{\text{SF}} \propto |\chi_{\text{eff}}^{(2)}|^2 I_{\text{vis}} I_{\text{IR}} \quad (2.4)$$

where  $\chi_{\text{eff}}^{(2)}$  is related to  $\chi_{i,j,k}^{(2)}$  via experimental geometry considerations and associated Fresnel coefficients.<sup>27,28</sup> The macroscopic susceptibility  $\chi_{i,j,k}^{(2)}$  depends on both the orientational average of the molecular hyperpolarizabilities,  $\langle\beta\rangle$ , and the number of contributing molecules,  $N$ , via Equation (2.5).

$$\chi_{i,j,k}^{(2)} = \frac{N}{\epsilon_0} \sum_{i',j',k'} \langle \mathbf{R}_{ii'} \mathbf{R}_{jj'} \mathbf{R}_{kk'} \rangle \beta_{i',j',k'}^{(2)} \quad (2.5)$$

where  $\mathbf{R}_{qq'}$  is the Euler rotation capable of transforming the molecular  $i'j'k'$  coordinates to the laboratory  $ijk$  coordinates.

The intensity of the SF light is enhanced when the IR frequency is resonant with molecular vibrational modes. Thus, by tuning the IR beam across a wavelength range, VSF spectroscopy generates a vibrational spectrum of interfacial molecules. The second-order molecular hyperpolarizability term,  $\beta^{(2)}$ , has both resonant and nonresonant ( $\beta_{NR}^{(2)}$ ) terms.

$$\beta^{(2)} = \beta_{NR}^{(2)} + \sum_q \frac{A_q}{\omega_{IR} - \omega_q + i\Gamma_q} \quad (2.6)$$

Where  $\omega_q$  is the resonant frequency,  $\Gamma_q$  is its broadening, and  $A_q$  is the SF strength factor related to IR ( $\frac{\partial\mu_{k'}}{\partial Q_q}$ ) and Raman ( $\frac{\partial\alpha_{i'j'}}{\partial Q_q}$ ) properties of a  $q$ th vibrational mode



according to Equation (2.7):

$$A_q^{i'j'k'} = -\frac{1}{2\epsilon_0\omega_q} \frac{\partial\alpha_{i'j'}}{\partial Q_q} \frac{\partial\mu_{k'}}{\partial Q_q} \quad (2.7)$$

The result of Equation (2.7) shows SF vibrational modes must be both IR and Raman active, as any nonexistent polarizability ( $\alpha_{i'j'}$ ) or dipole moment ( $\mu_{k'}$ ) transition will result in no response from  $\beta^{(2)}$ . Molecular symmetry arguments determine which elements of  $\beta^{(2)}$  (or analogously the  $A_q^{i'j'k'}$ ) contribute to the overall  $\chi_{ijk}^{(2)}$ . For the methylene group of  $C_{2v}$  symmetry, these nonvanishing elements of  $\beta^{(2)}$  have been meticulously determined by Hirose and coworkers.<sup>27</sup> For  $A_1$  symmetry (the symmetric stretch and bending vibrations), the elements are  $\beta_{aac}^{(2)}$ ,  $\beta_{bbc}^{(2)}$ , and  $\beta_{ccc}^{(2)}$ . For the  $B_1$  symmetry (the asymmetric stretch), the elements are  $\beta_{aca}^{(2)} = \beta_{caa}^{(2)}$ . Assuming a methylene bond angle of  $109.5^\circ$  and fixing the molecular coordinates such that the molecular plane is ac and the c-axis is the bisector of H–C–H, the tensor elements of  $\chi_{ijk}^{(2)}$  may be derived, as shown by Lü, et al.<sup>30</sup>

For the purposes of this discussion, only the *ssp*-polarization will be considered. Using known relationships between the  $\beta_{i'j'k'}^{(2)}$  terms, the expressions of Lü greatly simplify, as shown for the symmetric (SS) and asymmetric (AS) stretch of the methylene group.

$$\chi_{xxz}^{(2),SS} = \frac{1}{4}N(\beta_{aac}^{(2)} + \beta_{bbc}^{(2)} + 2\beta_{ccc}^{(2)})\langle\cos\theta\rangle + \frac{1}{4}N(\beta_{aac}^{(2)} + \beta_{bbc}^{(2)} - 2\beta_{ccc}^{(2)})\langle\cos^3\theta\rangle = 2\cos(\theta) \quad (2.8)$$

$$\chi_{xxz}^{(2),AS} = -\frac{1}{2}N(\beta_{aca}^{(2)})(\langle\cos\theta\rangle - \langle\cos^3\theta\rangle) = -2.106[\cos(\theta) - \cos^3(\theta)] \quad (2.9)$$

Plotting the  $\chi_{xxz}^{(2),SS}$  and  $\chi_{xxz}^{(2),AS}$  versus varying degrees of  $\theta$ , gives Figure 2. This plot clearly shows that for any angle of the methylene group, the symmetric stretch

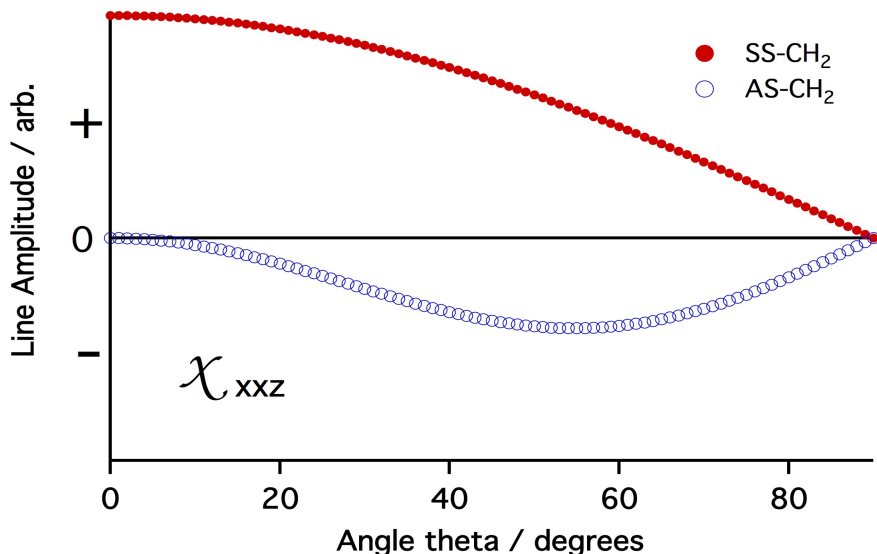


FIGURE 2. Plot of susceptibility in  $xxz$  of the SS-CH<sub>2</sub> (red, filled circles) and AS-CH<sub>2</sub> (blue, open circles) at varying degrees of molecular tilt ( $\theta$ )

and asymmetric stretch will be out of phase (of opposite sign) in  $ssp$  polarization. Other selection rules arise from this analysis, such as SS-CH<sub>2</sub> should not appear in  $sps$  and that any peak more intense in  $ssp$  than in  $ppp$  cannot be from AS-CH<sub>2</sub>.<sup>30</sup> However, the assertions of these selection rules break down as soon as the methylene oscillators behave non-ideally (i.e. couple). Nevertheless, taking the absolute value of the ratio of SS and AS from this plot and comparing it to the ratio of the assigned SS and AS from data, extraction of the molecular tilt of the methylene group from surface normal is possible. (The molecular twist is ignored in this analysis.) Ultimately, this detailed molecular symmetry analysis relies on arguments of isolated oscillators in constrained geometries; in systems where the molecular behavior departs from these assumptions the experimentalists rely on computationalists to determine relevant behaviors and frequencies for the specific system under study.

## Computational Methodology

Fundamentally, the desired outcome of the computational methodology is to generate a realistic picture of the interface in order to compare it with changes observed experimentally. This realistic picture holds information on surface density, surface orientation, and preferred molecular conformation. Strong confidence in simulated interfacial pictures is best obtained by comparison with measurable metrics. Vibrational sum frequency spectra are calculated to confirm that the interfacial picture accurately reflects the experimental reality, but additionally to assist in vibrational assignments. Typically, an interfacial picture is generated using molecular dynamics simulations (MD), while accurate calculations of frequencies and molecular response are determined using various quantum mechanical (QM) approaches.

Calculating VSF spectra can be achieved via a range of approaches,<sup>32-37</sup> and the details of each approach differ in the level of approximations, system size, and computational expense. Ideally, for each system under study one would perform highly rigorous quantum mechanical dynamics calculations. However, for systems larger than diatomic gases, achieving this level of rigor is near impossible. Choosing a computational approach always involves a trade off between the accuracy of results given, respectability of approximations, appropriateness of system size, and computational expense (both in time and processing power). Moreover, the multitude of approaches for calculating VSF exist because no single approach best balances these three trade offs in all situations.

The systems in this dissertation deal with small molecules ( $N < 15$ ) and thus can accommodate more rigorous QM approaches for calculating VSF frequencies. However, the systems also examine solution dynamics, seeking information on surface to bulk partitioning and behavior; the calculated VSF frequencies, moreover, are

wholly dependent on these dynamics. Thus a compromise is needed between QM calculations and capturing larger-scale phenomenon. Some VSF methodologies compromise by drastically shrinking the system size, and using *ab initio* molecular dynamics (AIMD) to calculate an entire, smaller system quantum mechanically. AIMD system sizes and trajectory time lengths are small,  $\sim 10$  Å and  $\sim 1$  ns respectively,<sup>38–40</sup> while time and length scales possible with classical dynamics may be orders of magnitude larger. However, employing AIMD allows for more accurate calculated frequencies and response properties as they are obtained directly from the system wavefunction.

The computational methodology employed throughout this dissertation, however, chooses an alternative track. Instead of sacrificing system size for accuracy of frequency calculations, we employ an amalgamation of classical molecular dynamics with quantum mechanical calculations. In essence, we generate accurate information from each method independently, then combine the requisite information afterward. This combination allows for larger system sizes to be probed, but additionally allows for reasonably accurate frequency calculations. (Typical box sizes include 900 water molecules and 16–160 solute molecules in a 30 Å x 30 Å x 30 Å box.) What this approach requires, however, that other approaches do not is a way of accurately mapping the information gained in the classical MD to the QM frequency calculations.

As explained in greater detail in the next chapter, classical molecular dynamics are used to extract interfacial orientation and molecular conformations. These simulations occur in a large water box with reasonable distinction between surface and bulk regions. Molecules are parameterized with atomic charges iteratively fit to reproduce the quantum mechanically determined electrostatic potential (RESP fitting). This allows the classical application of forces (i.e. “balls on springs”) to

include contributions that account for hydrogen bonding and Coulomb interactions. However, unlike AIMD methods, chemistry (i.e. bond breaking and forming) does not occur. Our systems must therefore initially contain all reactant and product species necessary for accurate analysis.

Vibrational frequencies are calculated with DFT, which has been shown capable of generating accurate VSF spectra.<sup>36,41</sup> The DFT is additionally employed to calculate polarizability and dipole moment changes with respect to each vibrational normal mode of gas phase structures. An in-house code then monitors the conformers from MD and matches the DFT structures to a representative conformer. In the event the code is unable to accurately account for the full MD conformational space, additional structures are included in the DFT calculations until >70% of structures are assigned to conformers.

Using this combination of MD and QM allows for accurate calculation of vibrational frequencies and response tensor elements without sacrificing system size and sampling. Ultimately, the robustness of the methodology is determined not only by how well it matches current data but how well it predicts future data. The use of VSF to examine complex, reacting systems necessitates utilizing computational tools to help unravel the myriad spectral signatures and dynamics.

### **Wilhelmy Plate**

The interfacial region often exhibits enhancement or loss of surface species as reactions progress or concentrations change. The dynamics governing these interfacial population changes often differ from the bulk, and are not solely correlated to bulk concentration. VSF spectra can provide evidence for changing interfacial population, but often this spectral evidence is convolved with other physical changes occurring

in the system. It is therefore necessary to have a measurable way of determining changes in surface population independent of the VSF spectra. Surface tension measurements provide such a way by enabling determination of the interfacial number density and surface area per molecule. These metrics allow for comparison with changes in VSF spectral intensity and help clarify the overall surface picture.

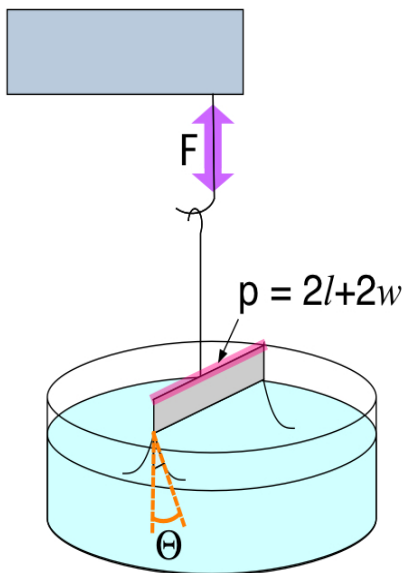


FIGURE 3. Representative Wilhelmy plate used in surface tension studies.

For this dissertation, the Wilhelmy plate method was primarily used to measure surface tension. The experimental details of using this method are presented in the following chapter, but a brief discussion of the theory governing this method is included here. The Wilhelmy plate method involves a thin plate attached to a force balance sensitive enough to detect micro-newton changes in force, as shown in Figure 3. When the plate encounters a solution, a meniscus is formed which exerts a measurable force on the plate. The surface tension ( $\gamma$ ) of the solution under study is

dependent on this measured force ( $F$ ), as well as the perimeter of the bottom of the plate ( $p$ ), and the contact angle ( $\theta$ ) between the edge of the plate and the meniscus, according to Equation (2.10):

$$\gamma = \frac{F}{p * \cos \theta} \quad (2.10)$$

The surface tension of pure water ( $\gamma_0$ ) is recorded daily to ensure instrument performance and to normalize changes in data sets by converting surface tension

values to surface pressures ( $\pi$ ).

$$\pi = \gamma_0 - \gamma \quad (2.11)$$

Surface pressure may then be plotted as a function of bulk solute concentration to generate a surface pressure isotherm. Typically, increases in the surface pressure isotherm indicate surface population increases alongside bulk concentration, and vice versa; but to better account for surface dynamics the Gibbs adsorption equations are employed. These equations enable calculating the maximum surface excess, the average area per molecule, the relative adsorption, and the surface mole fraction from surface pressures.<sup>42</sup>

The surface concentration at maximum solute surface coverage may be found by calculating the maximum surface excess ( $\Gamma_i$ ).

$$\Gamma_i = \frac{1}{RT} \left( \frac{\partial \pi}{\partial \ln a_i} \right)_{T,P} \quad (2.12)$$

( $\Gamma_i$ ) may be extracted from surface pressure by performing a linear fit to a plot of surface pressure versus the natural log of bulk activities ( $\ln a_i$ ), where  $R$  is the ideal gas constant and  $T$  is the temperature. The slope of the fit line to Equation (2.12) may be inverted to give the average area per molecule. The Frumkin isotherm may be used to calculate the surface excess ( $\Gamma_x$ ) at each bulk concentration value according to Equation (2.13):

$$\Gamma_x = \Gamma_i (1 - e^{\frac{-\pi}{RT\Gamma_i}}) \quad (2.13)$$

The surface excess describes the difference between an ideal system, i.e. one in which the surface has no effect on concentration,<sup>43</sup> and the real system where the surface does cause a sometimes large effect on surface concentration.

Alternative to surface excess the surface mole fraction, as described by Tyrode and coworkers,<sup>44</sup> provides a more direct comparison to surface population. The surface mole fraction may be extracted from the surface tension data by calculating the relative adsorption ( $\Gamma_{2,1}$ ), according to Equation (2.14):

$$\Gamma_{2,1} = -\frac{x \left(\frac{\partial \gamma}{\partial x}\right)_{T,P}}{RT \left(1 + x \frac{\partial \ln \alpha}{\partial x}\right)} = \Gamma_2 - \Gamma_1 \frac{x}{1-x} \quad (2.14)$$

where  $x$  is the bulk mole fractions of solute,  $\alpha$  is the activity coefficients of the solute,  $\gamma$  is the solution surface tensions, and  $\Gamma_1$  and  $\Gamma_2$  are the surface excess concentrations of solvent and solute in  $\mu\text{mol}/\text{m}^2$ . Generating linear fits to the plots of  $\gamma$  versus  $x$  and  $\ln \alpha$  versus  $x$  enables solving for  $\Gamma_{2,1}$  at each bulk mole fraction of solute. Then using the area per molecule ( $a_1$ ) value of solute calculated from Equation (2.12) and the known area per molecule value for the solvent (water is  $8 \text{ \AA}^2$ ),<sup>44</sup> the monolayer model may be evoked to solve for surface mole fraction ( $m.f.s$ ) for every bulk mole fraction of solute, where  $N_A$  is Avogadro's number.

$$N_A(\Gamma_1 a_1 + \Gamma_2 a_2) = 10^{26} \quad (2.15)$$

$$m.f.s = \frac{\Gamma_2}{\Gamma_2 + \Gamma_1} \quad (2.16)$$

Using these sets of equations enables direct comparison between changes in bulk and surface populations, which greatly informs interpretation of VSF spectral response as well as helps verify the molecular picture extracted from computational techniques. It should be noted, however, that the Gibbs equations best represent behavior of single component systems, with characteristic monolayer-like adsorption behavior. Understanding surface tension changes to complex, reactive mixtures



is a subject for much ongoing study, with some advances in modeling complex systems recently reported.<sup>45,46</sup> Nevertheless, the equations presented above will only be employed in the single-component monoethanolamine system of Chapter V, with surface tension changes in the reactive systems discussed only in comparative terms to the simpler system.

## Conclusions

Harnessing the combined strength of surface spectroscopy, computational methodology and surface tensiometry allows for a clear picture of surface behavior and speciation to be drawn. What follows in the next chapter is a detailed discussion of the experimental parameters and equipment necessary for conducting the above mentioned techniques. The remainder of this dissertation draws upon the discussion presented in this chapter in order to clearly describe the reacting systems under study.

## CHAPTER III

### EXPERIMENTAL CONSIDERATIONS

The previous chapter discussed the theory behind the surface techniques employed throughout this dissertation. What follows in this chapter is a discussion of experiments necessary to properly conduct the surface science. These experiments involve three main approaches. One, surface tensiometry, provides information on the surface population and adsorption dynamics of surface systems. Another, a combination of molecular simulations and computational calculations, allows for extraction of surface species' orientation, spectral mode assignments, and understanding cooperative effects of multiple surface species. The third approach, sum frequency spectroscopy, provides a vibrational spectrum of surface species. Wrapped in this vibrational spectrum is information on the characteristic species at the surface, the population of surface species, the orientation of surface species and the binding environment. Taken together, the spectral information obtained through vibrational sum frequency can describe in detail the molecular level picture of surface systems. Often, however, such spectral information is difficult to deconvolve and requires clever spectroscopy and the above-mentioned complementary techniques to gain an appropriate understanding of the system under study. Combining these approaches, as was discussed in the previous chapter, ensures clarity when deciphering the behavior of reacting surfaces.

What follows is a discussion of these surface techniques. The laser system necessary for sum frequency spectroscopy will first be discussed, including an aside on multiphoton processes. A description of the sum-frequency experiment including gas flow considerations, and a detailing of how equipment is cleaned will follow. A

discussion of relevant data analysis techniques for the sum frequency experiments will conclude the sum frequency discussion. An overview of the of the computational approach for calculating sum frequency spectra will be discussed. The chapter will conclude with a discussion of the Wilhelmy plate method, bulk Raman acquisition, and sample preparation.

### **Vibrational Sum Frequency Spectroscopy**

As detailed in the previous chapter, sum frequency generation is an energetically low process, with most of the energy of the incident beams going toward linear reflection or refraction. (The  $\mathbf{P}^{(1)}$  term in Equation (2.2)) Pulsed lasers, which are capable of generating high peak powers, ensure enough energy remains to generate the sum frequency process, while the pulse durations protect the sample surface from damage. Thus, the laser system used during this dissertation contains a  $\sim 2.6$  picosecond pulse with a 1 kHz repetition rate. This picosecond beam is centered around 800 nm, and is split into the visible (unchanged, 800 nm) line and infrared (downconverted,  $2.5 \mu\text{m}$ – $12 \mu\text{m}$ ) line for the sum frequency experiments. The principle components of the laser system used in these studies have been described in detail elsewhere,<sup>19,41,47</sup> although upgrades to the infrared generation and detection stages are unique to the projects described here.

#### *The Laser System*

As shown in Figure 4, the visible light used throughout these experiments begins with a continuous wave (CW) green laser centered at 532 nm. Both a Coherent Verdi and a Spectra-Physics Millennia were used throughout these studies. This CW light is routed into a Ti:Sapphire oscillator (Coherent Mira) that passively mode-locks

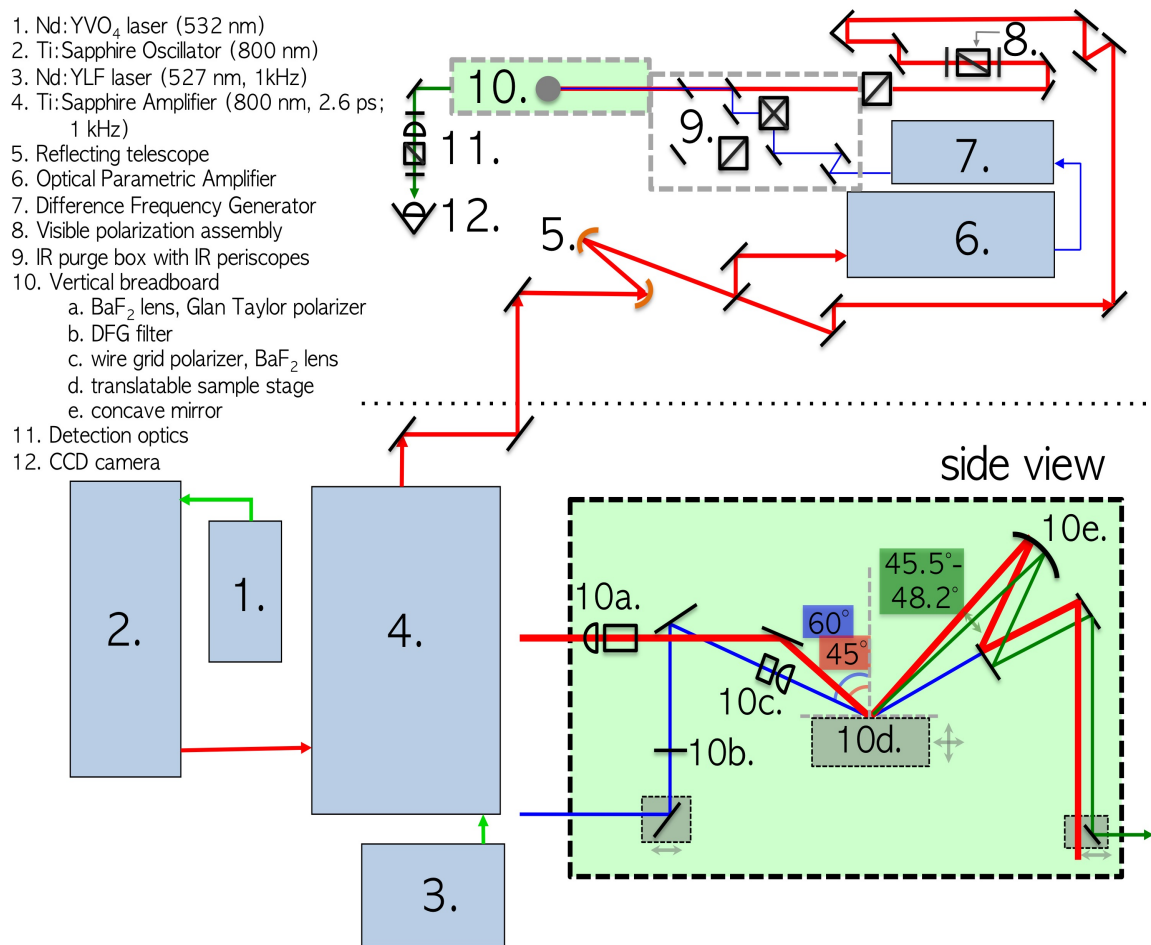


FIGURE 4. Simplified schematic of the laser system used for sum frequency spectroscopy, with inset of vertical breadboard. Incident beam angles at interface are visible = 45° and IR = 60°. Red lines indicate visible beam, blue lines indicate infrared beam, while the dark green lines indicate the sum frequency beam.

the CW to produce  $\sim 800$  nm,  $\sim 76$  MHz pulses. This resultant  $\sim 135$  fs red light seeds a regenerative Ti:Sapphire amplifier (Spectra-Physics Spitfire Pro XP) that is pumped with  $\sim 18$ -20 W of green light from a Nd:YLF laser (527 nm, Spectra-Physics Empower). The regenerative amplifier first stretches the seed pulse from the oscillator then significantly amplifies the pulse in the regenerative cavity before finally compressing the output beam. The resultant  $\sim 2.6$  ps,  $\sim 800$  nm, 1 kHz pulse is  $\sim 2$  W.

The amplifier output (red line in Figure 4) then travels along a series of optics, including a reflecting telescope to narrow and collimate the beam to  $\sim 5$  mm, before encountering a 75/25 beam splitter. Approximately 0.5 W of the incident 800 nm beam continues relatively unchanged as the visible line for the sum frequency experiments. The visible beam travels a series of optics to match a harmonic of the pathlength the infrared beam travels. The visible beam exits the amplifier horizontally polarized (*s*-polarized in the interfacial frame) and encounters an assembly (8 in Figure 4) of  $\lambda/2$  wave plate, cube polarizer,  $\lambda/2$  wave plate to set its intensity and polarization for the SF experiment. The first  $\lambda/2$  wave plate of the assembly is used to attenuate the incident visible by mixing its polarization; the cube polarizer ejects any vertical polarization and passes horizontal; and the second  $\lambda/2$  wave plate selects the visible polarization by either passing the output of the cube polarizer or fully converting the output to vertical. Once the intensity and polarization of the visible beam is set, it travels through a height changing periscope before being directed onto a vertical breadboard.

The remaining  $\sim 1.5$  W of the incident  $\sim 800$  nm light is routed into an optical parametric amplifier (OPA) and difference frequency generator (DFG) assembly (6,7 in Figure 4; Light Conversion Topas-800 and N-DFG). The OPA takes the input  $\sim 800$  nm beam and down converts the seed via a barium borate (BBO) type II crystal to produce signal from 1150–1620 nm at 250–350 mW after amplification. Wavelengths are selected by calibrating the BBO crystal angle with the angle of a 300 grooves/mm diffraction grating, creating a spectral resolution of  $\pm 5$  nm. The OPA signal and idler are mixed in the DFG’s silver gallium sulfide crystal to produce output IR wavelengths from 2.5  $\mu\text{m}$ –12  $\mu\text{m}$  at 35–5  $\mu\text{J}$  used as the infrared line in the sum frequency experiments. A calibration curve of the OPA and DFG crystal angles,

the OPA grating angle, and the OPA and DFG delay mirrors enables the scanning of infrared frequencies throughout data acquisition so that a broad spectrum is obtained from discrete frequencies.

The IR output (blue line in Figure 4) exits the DFG box horizontally polarized (*s*-polarized in the interfacial frame) and enters a series of dry air purged boxes (PneuDRi MIDAS, Parker) to minimize infrared intensity loss from ambient water and CO<sub>2</sub> absorption. The boxes are not airtight, but instead are kept at positive pressure to constantly replace the ambient volume with generated dry air. Typical experimental humidities inside the boxes are  $\sim 10\text{--}30\%$  RH. The horizontally polarized infrared beam can take one of two paths within the purge boxes depending on the polarization needed for the experiments. One path, as shown in Figure 4, routes the infrared through an off-axis periscope to change the infrared polarization to vertical; the opposite path routes the infrared through a periscope that performs a height change while maintaining horizontal polarization. This infrared beam is then directed onto a vertical breadboard.

The visible and infrared beams enter the vertical breadboard at different heights, as shown in the green side view of 10 in Figure 4. Both visible and infrared lines contain BaF<sub>2</sub> lenses to focus the beam at the interface. These lenses are set such that their focus is just beyond ( $\sim$ few mm) the sample surface. Additionally, as a final insurance of proper polarization, both the visible and infrared lines have polarizers just before being steered to the interface. The incident beam angles of both the visible and infrared beams are variable, since interchanging the incident angles can greatly impact the detected sum frequency intensity and spectral interpretation.<sup>48</sup> For the studies presented in this dissertation, the beam angles are either visible = 45° and infrared = 60°, as shown in Figure 4, or visible = 63° and infrared = 55°. These

angles were calculated from refractive indices and nonlinear Fresnel coefficients to maximize the sum frequency response.<sup>48,49</sup>

The visible and infrared beams are then both spectrally and temporally overlapped at the sample surface to generate a sum frequency response (green line in Figure 4). The spectral overlap is achieved by adjustment of the final IR mirror to maximize visual proximity of the two beams on heat paper set at the designated interfacial height; the temporal overlap is achieved by adjustment of the visible retroreflector to maximize SF intensity. The generated sum frequency beam is emitted in the phase-matched direction, with its angle relative to the surface determined by the incident angles ( $\theta_{vis}, \theta_{IR}$ ) and frequencies ( $\tilde{\nu}_{vis}, \tilde{\nu}_{IR}$ ) of the visible and infrared beams, according to Equation (3.1).<sup>49</sup>

$$\theta_{SF} = \arcsin \left( \frac{\tilde{\nu}_{vis}}{\tilde{\nu}_{SF}} \sin \theta_{vis} + \frac{\tilde{\nu}_{IR}}{\tilde{\nu}_{SF}} \sin \theta_{IR} \right) \quad (3.1)$$

Since the frequency of the infrared beam changes throughout data acquisition, as a result of scanning the crystal and grating angles within the OPA/DFG assembly, the outgoing SF response varies in output angle. To reduce aberrations and better separate the visible beam from the SF, a concave mirror, placed at its focal length, collects the beams outgoing from the sample surface. This mirror, designated 10e in Figure 4, takes the angular separation of the visible and SF beams and locks it into a spatial separation. The visible and sum frequency beams travel along a series of optics at this set width, before a final mirror on a micrometer stage picks off the sum frequency, sending it to the detection line. The detection line contains a 600 nm longpass filter, a lens to focus the SF on the camera, a cube polarizer to select the detected SF polarization, a 785 nm ultrasteep shortpass filter (RazorEdge, SEMROCK) to block any remaining visible light, and a thermoelectrically cooled

CCD camera (PIXUS, Princeton Instruments). Updating the acquisition optics in this manner has reduced the overall background from previous setups by an order of magnitude, greatly enhancing signal to noise.

*An Aside: Multi-photon Processes*

An unpleasant consequence to arise from this experimental set-up is the detection of multi-photon surface phenomena. Though energetically unfavorable, multi-photon phenomena can occur, and unless accounted for can lead to false data interpretation. In this experimental system, no spectrometer is used prior to the CCD camera, thus extreme caution must be undertaken to ensure no errant processes are interacting with the SF response. In fact, an errant response was detected and found to arise from the surface generation of a multi-photon (IR+IR+visible) process. It is unclear from where the second IR photon arises for this process, but such a response has been observed, and could be ignored, in other sum frequency experiments. Due to the unique constraints of this experimental set-up, however—no detection spectrometer, scanning frequencies, etc.—the presence of this multi-photon response requires additional measures.

In this system the infrared generation in the OPA/DFG assembly is discrete, with each wavelength generated independently at  $\pm 5$  nm resolution. As mentioned earlier, a scan of an entire vibrational range is achieved by synchronizing via a LabView program the calibration curves of the OPA and DFG at these discrete frequencies and incrementally stepping through each frequency, usually in  $3 \text{ cm}^{-1}$  increments. Throughout this step-wise progression of IR frequencies, the angle of the sum frequency beam relative to the interface changes, as shown in Equation (3.1),



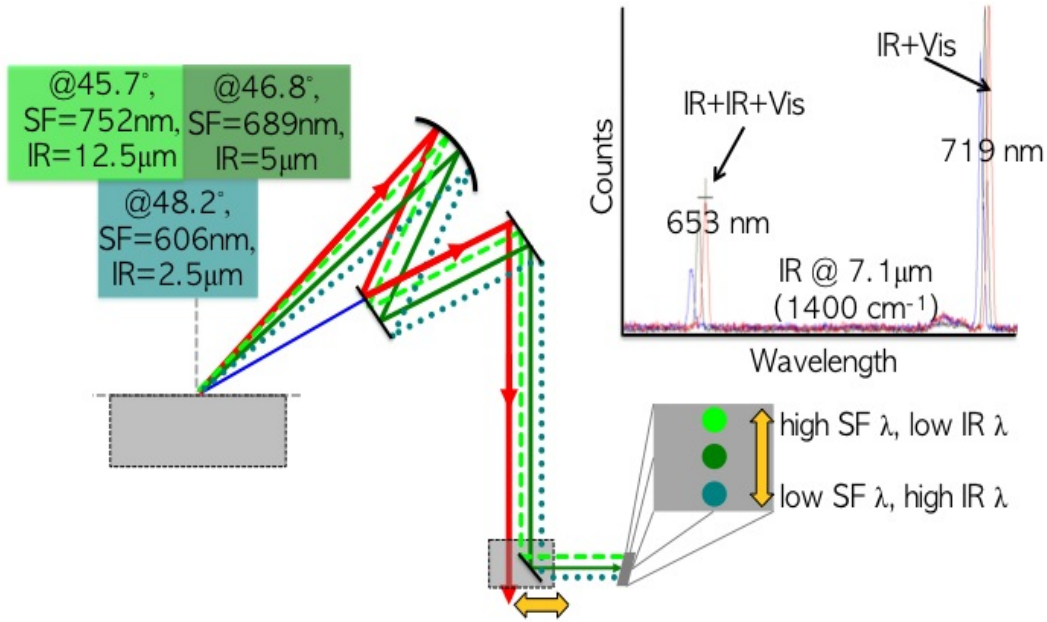


FIGURE 5. Schematic of the acquisition optics used for sum frequency spectroscopy (10e – side in Figure 4). Incident angles are visible = 45° and IR = 60° (not shown). The dashed, solid and dotted green lines represent different SF beam paths depending on the frequency of the infrared input. The inset shows the output SF spot (IR=7.1  $\mu\text{m}$ , Vis=800 nm) directed through a spectrometer, revealing two distinct frequencies.

moving from broader angles at low IR frequencies to shallower angles (closer to the 800 nm beam) at high IR frequencies, as shown in Figure 5.

This change in SF output angle results, as a consequence of the current set-up, in a change in spatial position of the final output beam such that the SF beam vertically translates along the detection optics as the experimental scan progresses. This is shown in Figure 5 as a change in position observed on a mirror (grey box), with higher SF frequencies at top and lower SF frequencies at bottom. This experimental detail would be unremarkable if not for the detection lens, which is set at its focal length, and thus focuses all beams regardless of position to the same point on the CCD camera. As the scan steps through the infrared frequencies and the SF spots move along the detection optics vertically, the camera records only one, unchanging spot. Since the frequencies, and thus positions, of the SF spots are determined by

the frequencies of the infrared, this movement should be inconsequential if only one frequency is generated per input frequency of infrared.

The final, key assumption, that only one frequency is generated per scan step is false. Despite the energetic cost of generating sum frequency with two input beams, higher order processes can also arise when high enough energy densities are used. For this system, an additional spot was observed along the detection line. The additional spot, as shown in the inset of Figure 5, was at a lower frequency than the SF spot, and tracked concomitantly with the sum frequency spot as the infrared frequency was changed. It was originally thought that this errant spot was a result of additional IR generation in either the OPA or DFG. However, the DFG output was tested on a monochromator and only one output frequency was observed at each point throughout the calibration curve.

Input frequencies of  $7.1 \mu\text{m}$  ( $1400 \text{ cm}^{-1}$ ) for the infrared and  $\sim 800 \text{ nm}$  ( $12500 \text{ cm}^{-1}$ ) for the visible, the SF should be at  $719 \text{ nm}$  ( $13900 \text{ cm}^{-1}$ ). As shown in the inset of Figure 5, this was observed on the spectrometer along with a second, lower frequency. The second, errant frequency was observed at  $653 \text{ nm}$  ( $15313 \text{ cm}^{-1}$ ). The difference between the  $653 \text{ nm}$  spot and the SF spot at  $719 \text{ nm}$  is  $\sim 1400 \text{ cm}^{-1}$ , the frequency of the incident IR. When the frequency of the infrared was changed, the frequencies of both the SF and the errant spot changed, with the SF changing linearly with IR frequency while the errant spot changed by a factor of two. This second spot, therefore, arose from an IR+IR+visible process generated at the surface.

Due to the detection setup, this errant spot was collected by the camera at all calibration positions where the pickoff mirror could spatially collect both the SF spot and the IR+IR+visible. The pickoff mirror is the final mirror on the vertical breadboard, sending the sum frequency beam toward the detection line. This mirror

is on a micrometer stage so that its position may be adjusted depending on which spectral region is being measured. Its position is optimized for the maximum SF intensity at the middle frequency within a scan’s spectral range. In the stretching region ( $2.5\ \mu\text{m}$ – $4\ \mu\text{m}$  infrared input) at the input angles of visible =  $45^\circ$  and IR =  $60^\circ$ , the pickoff mirror is set to the far right, closest to the detection line. At this position, the IR+IR+visible process generates frequencies from 490–540 nm, propagating even further to the right than the pickoff mirror can travel. Thus, the multiphoton process was never of consequence in the stretching region data acquisition. In the bending region ( $5.5\ \mu\text{m}$ – $11\ \mu\text{m}$  infrared input) at the input angles of visible =  $45^\circ$  and IR =  $60^\circ$ , the pickoff mirror is set to the middle of its travel, further left from its setting in the stretching region. At this position, the IR+IR+visible process generates frequencies from 620–700 nm, appearing on the bottom edge of the pickoff mirror as shown by the teal dot in Figure 5. Thus, the multiphoton process greatly affects data acquisition in the bending region. As a consequence, a set of two 700 nm longpass filters are used in the detection line to block all IR+IR+visible response during data acquisition in the bending region. Additionally, the detection lens is positioned slightly before its focal length such that any errant frequencies will be separated in space on the camera.

### *The Interface*

Despite the complexity of the laser system necessary for sum frequency generation, the majority of experimental time (and design) is spent within the area of the interface, denoted as 10d in Figure 4. The interface is set at an arbitrary height on the vertical breadboard, but once determined contains a number of elements that must work in concert to achieve the desired SF signal generation. A stage with tilt, yaw and vertical adjust is housed a few centimeters below

the interface, to enable fine adjustment of the system between samples. A gas-tight polychlorotrifluoroethylene (kel-F) chamber sits on the stage and holds the experimental samples. The kel-F chamber, shown in Figure 6, has three windows: a  $\text{BaF}_2$  input window set orthogonal to the input IR angle, a fused silica output window set orthogonal to the middle of the SF output angle, and a silica window along the front, allowing visual inspection of the surface during experiments. A blue glass filter resides at the bottom of the chamber to minimize visible light scatter.

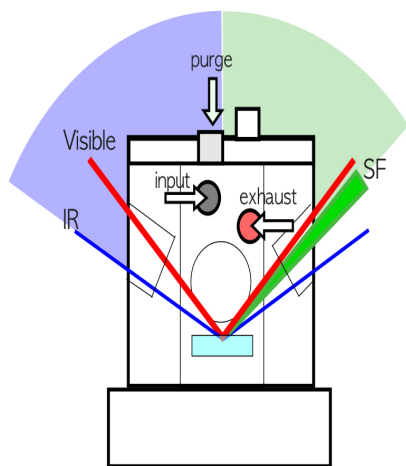


FIGURE 6. Schematic of the experimental cell used during gas flow studies.

The kel-F chamber also has three gas ports: an input that contains  $\text{CO}_2$ ,  $\text{SO}_2$ ,  $\text{HCl}$  or mixtures of the three, an exhaust leading to a fume hood, and a purge that contains the carrier gas,  $\text{N}_2$ . The tubing for the gas lines are either kel-F (input) or teflon (purge and exhaust), with kel-F or teflon adaptors fitted to the chamber ports with Kalrez o-rings. The acidic gases used in these

studies are individually monitored with flow meters on each line, but are mixed in a stainless steel manifold prior to introduction in the sample chamber. The chamber is kept at atmospheric pressure throughout these studies, with flow rate of the input matched to the exhaust.

The sample surface is generated by pouring samples into scrupulously clean, handmade glass dishes that are then lowered into the chamber. Sum frequency measurements are especially sensitive to contaminants, with detection limits on

the ppm scale.<sup>50</sup> All equipment encountering the samples during these studies thus undergoes a rigorous cleaning routine of a minimum 24 hour soak in a concentrated sulfuric acid/NoChromix solution, an overnight soak in ultrapure water (Barnstead Epure at  $> 18 \text{ M}\Omega\text{-cm}$ ), copious rinsing of each dish under ultrapure water, followed by drying in a  $\geq 200^\circ\text{C}$  oven. This cleaning regiment has been found to be best at removing most trace contaminants, however aqua regia and base baths are occasionally employed if the acid baths are unsuccessful. Due to the vigorous cleaning employed, all experimental equipment is limited to either glass or a highly chemical resistant plastic such as kel-F.

Once the solution under study is poured into the dishes and lowered into the chamber, the solutions are left to equilibrate for 10-15 min in dried air. During gas uptake studies, the acidic gas is turned on and allowed to equilibrate with the solution for a minimum of 30 min prior to data acquisition. Each day the interface is set based on the nonlinear response off an uncoated gold surface. This gold response closely matches the IR intensity, with characteristic dips due to ambient water and  $\text{CO}_2$ , but with a Gaussian profile due to walk off in the overlap of the infrared and visible beams at the surface. Once the gold is set, only the interfacial stage is raised and lowered throughout the day. The gold scans are used not only to calibrate the IR spectrum but to normalize the data. This is done by dividing the experimental spectra with the gold response, in order to account for day-to-day variations in IR absorption, spectral overlap, and laser efficiency. When gas uptake experiments are conducted, gold scans within the atmosphere of the gas under study are used for normalization, as shown in Figure 7. This ensures spectral dips due to IR absorption—such as those at  $\sim 3610$  and  $\sim 3710 \text{ cm}^{-1}$  in  $\text{CO}_2$ , and  $1360 \text{ cm}^{-1}$  in  $\text{SO}_2$ —are properly normalized.<sup>51</sup>

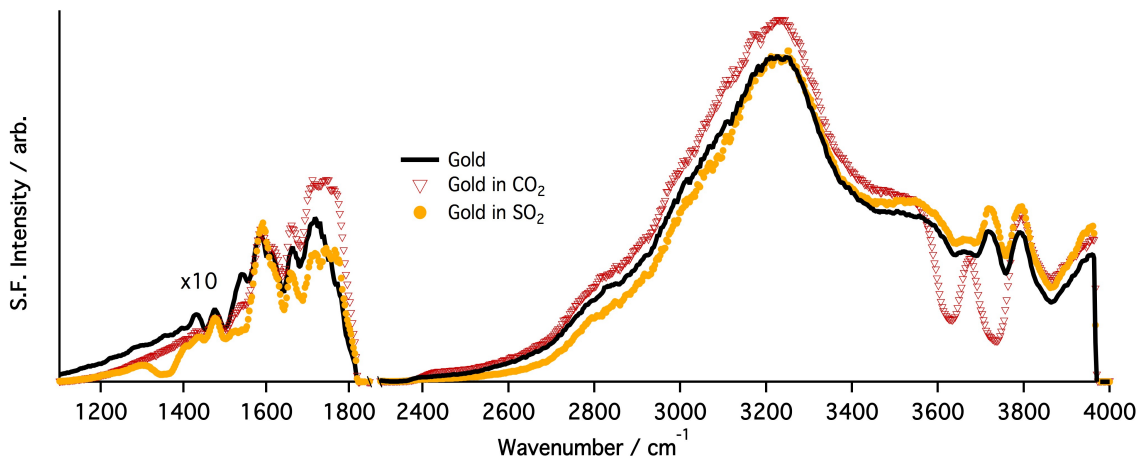


FIGURE 7. Non-resonant SF response off a gold substrate in dried air (black), in  $\text{CO}_2$  (red triangles) and in  $\text{SO}_2$  (gold dots). The intensity of the gold response in the bending region has been increased by 10.

### *Spectral Calibration and Fitting*

In addition to the SF response of gold, daily measurements are taken of the incident IR intensity spectrum as well as the IR intensity spectrum of polystyrene. As shown in Figure 8, the dips observed in the polystyrene spectrum (red) along with the dips due to ambient water absorbances off gold (black) provide a full range of calibration points encompassing the infrared range examined. The dips are assigned based off reported NIST values<sup>51,52</sup>, and are matched with the daily polystyrene scan. A plot of the known polystyrene values versus the daily polystyrene values is fit with a linear regression; the regression's slope and intercept are used to adjust the daily sum frequency wavelengths.

Once all data have been averaged (usually 9–20 scans), normalized and calibrated, the final experimental necessity is spectral fitting. Because the intensity and shape of the SF spectra occurs as a consequence of a number of overlapping resonant and nonresonant modes, spectral fitting is necessary to deconvolve the

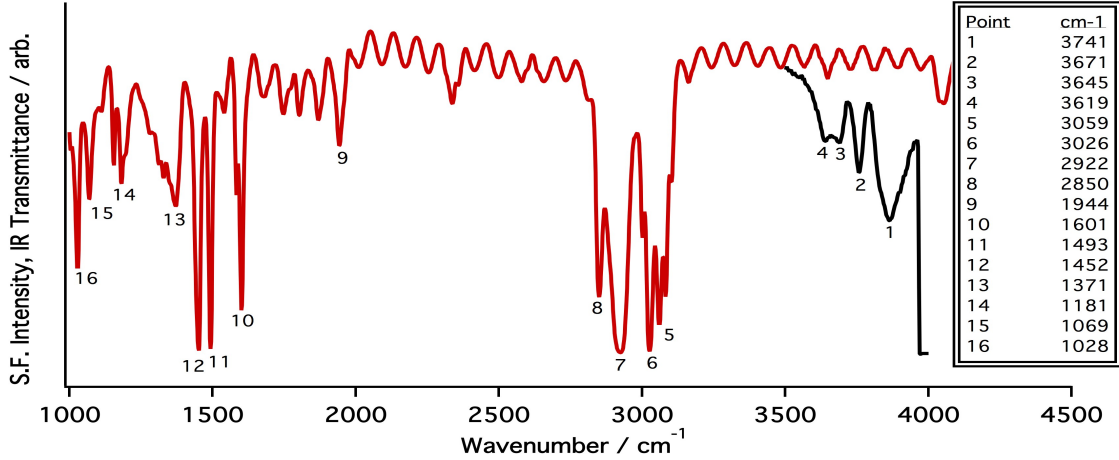


FIGURE 8. Characteristic IR absorbances of water (black) and polystyrene (red) used to calibrate the VSF data.

various contributions to the spectra. While a number of sum frequency groups employ only Lorentzian lineshapes<sup>31,53–55</sup> to describe the resonant response of oscillators, we employ a complicated fitting routine to account for broadening due to individual molecular transitions (homogeneous) as well as broadening due to the oscillators residing in condensed media with varying intermolecular constraints (inhomogeneous).

A fitting routine introduced by Bain<sup>56</sup> and established here by Moore<sup>57</sup> takes into account these various broadening terms, as shown by Equation (3.2).

$$\chi^{(2)} = \chi_{\text{NR}}^{(2)} e^{i\psi} + \sum_{\nu} \frac{A_{\nu} e^{i\phi_{\nu}} e^{-[(\omega_L - \omega_{\nu})/\Gamma_{\nu}]^2}}{\omega_L - \omega_{\text{IR}} + i\Gamma_L} \quad (3.2)$$

The first term in Equation (3.2) accounts for the non-resonant contributions to the SF spectra, including the non-resonant amplitude and phase ( $\psi$ ). The second term in Equation (3.2) is a sum over all the resonant modes  $\chi_{R_{\nu}}^{(2)}$ , and contains contributions from the vibrational transition strengths ( $A_{\nu}$ ), phases ( $\phi_{\nu}$ ), peak frequencies ( $\omega_{\nu}$ ), and broadening terms ( $\Gamma_{\nu}$  and  $\Gamma_L$ ) of all resonant modes.

Measurements of the neat air/water interface are taken daily to allow for comparison of spectral intensity over multiple days, but also to guide the fitting of systems in aqueous media. Spectral fits for the neat air/water interface have been well established,<sup>58-61</sup> and will be discussed in depth in the next chapter. Five unique variables are assigned for each fit of a resonant mode: an amplitude, phase, Lorentzian width, frequency and Gaussian width. As a result, fits to the spectra—especially in spectrally congested regions such as the OH/CH stretching region—may be non-unique. Thus care is taken in fits to limit the number of variables considered. All spectra are fit globally, with the daily water acting as the foundation of the fits. Any additional peaks are added to the global fit only when it is physically reasonable and absolutely necessary to achieve appropriate fit residuals. The nonresonant response of the vapor/liquid interface is also accounted for in the fitting routine, and contains contributions from amplitude and phase.

All phases are fixed to either  $\pi$  or 0, indicating either an up or down orientation relative to the surface normal at zero. Lorentzian widths are fixed, with their values determined by vibrational relaxation lifetimes of the specific vibrational transition.<sup>62-65</sup> For the oscillators in this dissertation, the  $\Gamma_L$  values are  $2\text{ cm}^{-1}$  for CHs,  $5\text{ cm}^{-1}$  for coordinated OHs and C=O,  $7\text{ cm}^{-1}$  for NHs, and  $12\text{ cm}^{-1}$  for the free OH. The global routine iteratively fits the data to achieve reasonable matches across all samples. The initial global fit varies only the amplitude of each contributing peak, constraining the remaining four. Loosening of the other parameter constraints like peak position or Gaussian width occurs only when necessary. The remainder of this dissertation will discuss in detail the various spectral fits and their interpretations for the systems under study.



## Computational Methodology

The computational approach used throughout this dissertation has been outlined in previous publications.<sup>41,66–69</sup> As mentioned in the previous chapter, this approach involves a combination of molecular dynamics simulations and quantum mechanical calculations. This combination avoids the high computational expense of *ab initio* dynamics, enabling examination of larger systems while maintaining high accuracy of molecular spectroscopic properties. The computational methodology discussed here was implemented in our lab by Dr. Nicholas Valley; some calculations included in this dissertation were performed by him and will be noted where appropriate.

The computational approach first involves classical molecular dynamics simulations of sample molecules in a water box with vacuum at both top and bottom. The dynamics evolve for a minimum of 45 ns. Information on molecular orientation relative to the surface, surface and bulk densities, and favored conformations of sample molecules within the water box is extracted. The favored MD conformers are then matched to gas-phase static structures from DFT calculations. A sum frequency response for each structure is then calculated using DFT methods. All molecular dynamics and density functional theory calculations were performed on the ACISS supercomputer<sup>70</sup> at the University of Oregon. Matching of the molecular dynamics conformers with the quantum mechanical structures and generating sum frequency spectra was performed on a local computer using in-house code.

### *Classical Molecular Dynamics*

Classical molecular dynamics (MD) simulations were performed using the Amber 12 suite of programs.<sup>71</sup> A 30 Å cube was created and randomly packed with 900 water molecules and 16–160 sample molecules, representing 1–10 M, using PACKMOL.<sup>72</sup>

The box's  $z$ -dimension was expanded to 120 Å and periodic boundary conditions were applied to create a box with two vacuum/liquid surfaces, as shown in Figure 9. Initial systems' energies were minimized at 0 K using a combination of steepest descent and conjugate gradient methods. The systems were then equilibrated while increasing the temperature from 0 K to 298 K over 2 ns. After equilibration, Langevin dynamics were used to evolve the system via a leapfrog integrator for >45 ns of simulation time, with a timestep of 1 fs. Data were recorded every 100 fs.

Simulation data were extracted after a minimum of 45 ns of evolution. Fully polarizable models were used for all simulation systems: POL3<sup>73</sup> for water and fully atomistic models for all sample molecules using the Amber FF02pol force field.<sup>71</sup> Electrostatic interactions were calculated using the particle mesh Ewald technique with a force cutoff of 10 Å. The SHAKE algorithm was used to hold the O-H bonds in the waters rigid, enabling faster data acquisition.

The interface was defined by the Gibbs dividing surface, with data collected for both vacuum/water interfaces of the box. Simulation distances are discussed relative to the ascribed interface and bond angles are reported relative to the interfacial normal pointing into the vacuum phase.

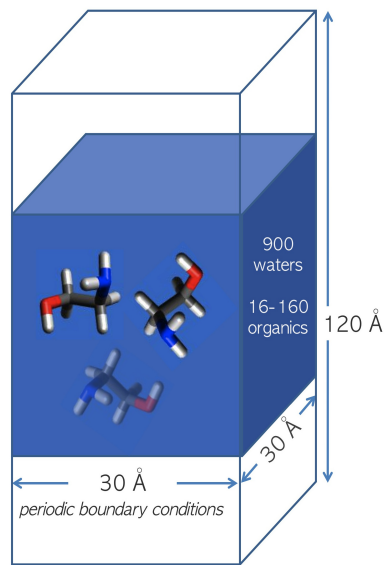


FIGURE 9. Representative water box used in MD studies.

## *Quantum Mechanical Calculations*

Density functional theory (DFT) calculations were performed using the NWChem<sup>74</sup> and Gaussian 09<sup>75</sup> program packages. Geometry optimizations and harmonic frequency calculations for isolated gas phase sample molecules were conducted using the B3LYP hybrid functional and the 6-311++G(2d,2p) basis set. Second-order vibrational perturbation theory (VPT2) was used to calculate anharmonic corrections to vibrational frequencies. Initially, a range of combinations for the VPT2 corrections was explored in order to garner the best agreement between experimental VSF and calculated spectra, with selection of basis sets and functionals guided by literature precedent.<sup>76-79</sup> B3LYP, B2PLYP, and MP2 functionals were matched with either 6-311++G(2d,2p) or aug-pVTZ basis sets. During the amine studies of Chapter V, B2PLYP/6-311++G(2d,2p) was found to provide the best agreement between calculated and experimental spectra with respect to both peak positions and relative intensities. The reader is directed to the discussion in the supplementary information of McWilliams, et al<sup>17</sup> for a detailed account of the chosen functional/basis set. B2PLYP/6-311++G(2d,2p) was therefore used in the calculation of all other spectra to maintain consistency during comparison.

The matching of static gas phase structures from the density functional calculations with the conformers extracted from the molecular dynamics simulations is afforded by in-house code.<sup>67</sup> The group of static DFT structures is initially created based on the maxima from the correlated dihedral distributions extracted from the molecular dynamics simulations. The conformer matching for each data set is checked to insure the representative gas structures account for more than >70% of the conformers present in the simulations. Occasionally, unfavorable gas phase structures are favorable in the condensed phase simulations; in such circumstances, key bonds

are locked to ensure accurate conformer matching. Three-point finite differentiation is used to calculate polarizability ( $\alpha$ ) and dipole moment ( $\mu$ ) derivatives for each normal mode (Q), according to Equation (3.3),

$$\chi_{ijk}^{(2)} \propto \sum_{a,b,c} C_{abc} \frac{\partial \alpha_{ab}}{\partial Q_q} \frac{\partial \mu_c}{\partial Q_q} \quad (3.3)$$

where the laboratory and molecular frames are related via  $C_{abc}$ . (This proportionality originates from the SF strength factor discussed in Equation (2.7) in the previous chapter.) This methodology allows for calculation of VSF spectra while accurately describing condensed phase molecular structures.

### Wilhelmy Plate

As indicated in the previous chapter, surface tensiometry measurements provide information on the number density of surface species along with information on surface adsorption dynamics. For this dissertation, surface tension data were collected primarily using a force balance via a Wilhelmy plate apparatus<sup>80</sup> (KSV Instruments). The Wilhelmy plate consists of a platinum plate suspended from a platinum wire; the force applied to the plate is measured versus starting time and the surface tension is calculated based on the plate perimeter via Equation (2.10). As was the case in the VSF experiments, surface tension samples are prepared and held in glass dishes scrupulously cleaned according to the procedure described above. The platinum plate (Biolin Scientific) was cleaned before each measurement by copiously rinsing under ultrapure water and heating over flame until glowing orange. Once clean, the plate was carefully lowered into the solution.

Surface tension of the neat air/water interface was taken at the beginning of each day to ensure surface tension values for each data set were comparable. During gas uptake studies, the kel-F chamber used in VSF measurements was employed for surface tension to mimic the conditions during the VSF experiments. The main exception to the VSF conditions, however, was that the air-tight lid to the chamber was by necessity removed. Rather, the kel-F chamber and force balance were additionally contained in an acrylic box fitted with an exhaust port to ensure complete containment of the experimental gases. Surface tension values were converted to surface pressure in order to correct for instrumental fluctuations by subtracting the surface tension of the neat air/water surface. All measurements were recorded at room temperature ( $\sim 20^\circ\text{C}$ ) and atmospheric pressure.

### Sample Preparation

All solutions were diluted volumetrically with either  $\text{H}_2\text{O}$  ( $> 18 \text{ M}\Omega\text{-cm}$ , Barnstead E-pure) or  $\text{D}_2\text{O}$  (99.9%, Cambridge Isotopes), and sonicated for a minimum of 10 minutes before use. Monoethanolamine ( $\geq 99\%$ ), ethylenediamine ( $> 99\%$ ), and N-boc-ethanolamine ( $> 98\%$ ) were purchased from Sigma-Aldrich and used as received. Ethylene glycol (0.04% water contamination) was purchased from Fisher.  $\text{Na}_2\text{CO}_3$  ( $> 99.95\%$ ) and  $\text{NaHCO}_3$  ( $> 99.5\%$ ) were purchased from Sigma-Aldrich. The carbonate salt was baked for a minimum of 72 hours at  $> 200^\circ\text{C}$  to eliminate organic contamination; the bicarbonate salt was not heated due to its rapid decomposition to carbonate at  $> 50^\circ\text{C}$ . Liquid hydrochloric acid (EMD) used for pH adjustment ranged from 36.5–38 wt.% in water. pH was measured with either pH paper (BDH or MColorpHast) or a pH meter (Sartorius PB-11).  $\text{CO}_2$  (cylinder, 99.99%) and  $\text{N}_2$  (cylinder) were purchased from Industrial Source.  $\text{SO}_2$  (lecture bottle, 99.98%) was

purchased from Scott Specialty Gases. HCl (lecture bottle, 99.995%) was purchased from Matheson Trigas. All gases were used as received.

### **Gas Flow Parameters**

All gas flow studies were conducted in the kel-F chamber mentioned above. Solutions were poured and data of the neat surface acquired before the reactant gas atmosphere was introduced. In the VSF studies, solutions were equilibrated for a minimum of  $\sim 30$  minutes before spectra were taken; in the surface tension studies, the force was measured immediately. No stirring of the solution occurred during gas flow, out of necessity of not perturbing the surface. The  $\text{CO}_2$  was introduced into the chamber at a rate of 0.6 liters per minute. The  $\text{SO}_2$  was introduced at a rate of 15 standard cubic centimeters per minute. An  $\text{N}_2$  carrier gas was used in the  $\text{SO}_2$  studies at a flow rate  $\sim 1$  liter per minute. All flow experiments occurred at room temperature ( $\sim 21^\circ\text{C}$ ) and atmospheric pressure.

### **Conclusions**

What follows in the remaining chapters is the implementation of these experimental techniques to examine the complex chemistry of a model carbon-capture surface. A brief discussion of the aqueous system in Chapter IV is followed by monoethanolamine and its reaction with different acidic gases and liquids. In order to accurately characterize the complex systems under study, all experiments discussed here will be utilized. This combination of surface spectroscopy, surface tensiometry, bulk studies and computational methods has enabled complex surface phenomenon to be examined.

## CHAPTER IV

### THE VAPOR/WATER INTERFACE

From the vast ocean surface to the tiniest cloud-forming aerosol to the exhaust from a smokestack, the interface between vapor and water contains enormous chemical diversity. The potential for unique chemistry and dynamics at the vapor/water interface holds import to understanding larger physical phenomenon. These vapor/water interfaces can play surprising and prominent roles in influencing larger systems. For example, the makeup of aerosol surfaces is known to play a role in mitigating chemistry and either inhibiting or enhancing gaseous uptake. These behaviors at the “small scale” of the aerosol surface have enormous impact on the behavior and chemistry governing “large scale” questions like contaminant species’ longevity in the atmosphere, greenhouse gas effects, and overall climate.

Understanding the behavior of the ubiquitous vapor/water interface is therefore fundamental to understanding more complex systems. For the purposes of this dissertation, we begin with a discussion of the vapor/water interface in order to lay the foundation for the more chemically diverse carbon capture systems in subsequent chapters. All systems herein involve aqueous solutions interacting with gaseous reactants. Therefore, to ignore the underlying water structure in these systems is to ignore many of the dominant changes, especially in the coherent VSF spectra where large water resonances convolve with resonances from the molecules under study. Thus, understanding the underlying water structure is essential to understanding changes in the more complex systems.

This chapter begins with an overview of the current interpretation of the vapor/water interface, primarily in light of the vibrational sum frequency spectra.

Current spectral analysis of both the stretching and bending region will be addressed, to lay the foundation for future parameters once organics are present at the surface. The chapter will finish with a discussion of the water surface under various acidic atmospheres, and how perturbations to the water surface manifest differently in the bending and stretching region.

### **The Neat Air/Water Interface**

The neat air/water interface has been explored in detail in numerous VSF studies<sup>19,55,59–61,81,82</sup> and computational simulations.<sup>34,58,83–88</sup> This interface exhibits high surface tension ( $\sim 72.7$  mN/M at 20°C)<sup>89</sup> indicative of strong hydrogen bonding between surface water molecules. In addition, the VSF spectra of the air/water interface shows prominent spectral features arising from 3800–2900  $\text{cm}^{-1}$  and 1800–1400  $\text{cm}^{-1}$  due to highly ordered surface waters, confirming the observation from surface tension of strong hydrogen bonding at the air/water interface. Much discussion surrounds the VSF spectra of so simple a system, in large part due to the broad, overlapping peaks arising from the extensive hydrogen-bonding network of liquid water.

The neat air/water interface can be described generally as a narrow region,  $\sim 6$ –10 Å deep, with decreasing hydrogen bonding nearer to the surface.<sup>90,91</sup> This picture of an ordered surface with decreased hydrogen bonding relative to the bulk creates the possibility of loosely mapping coordination and solvation preference of adsorbed species in regard to their affect on the hydrogen bonding structure of water. In order to interpret such changes to the water structure at the vapor/water interface, a fundamental understanding of the various contributions to the spectra is first necessary.



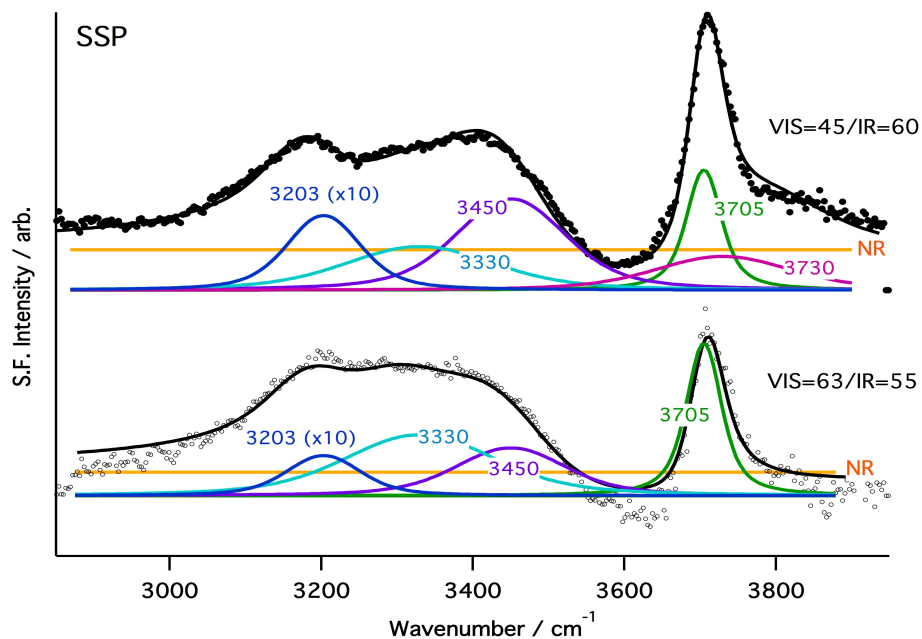


FIGURE 10. VSF spectra in the vibrational stretching region of the neat air/water interface (black) at incident angles visible=45° and IR=60° (top) and visible=63° and IR=55° (bottom). Resonant mode fits shown in green (free OH), purple (companion OH), and light and dark blue (tetrahedrally coordinated water); the non resonant contributions to the spectra are shown in orange.

### *The Stretching Region*

The neat air/water interface in the vibrational stretching region is dominated by a sharp feature around  $\sim 3700 \text{ cm}^{-1}$ , as shown in Figure 10 in green. This feature is assigned to oscillators that have one dangling OH bond pointing into the vapor phase, known as the “free-OH.” VSF analysis indicates approximately one in four surface waters have a free OH component.<sup>92</sup> The presence or absence of the free OH feature can indicate surface coverage of adsorbed species, as well as suggest interactions between top-most waters with gas phase species. The broad feature below  $3500 \text{ cm}^{-1}$  in Figure 10 is assigned to the coordinated water structure, comprised of water molecules residing along a continuum of hydrogen bonding environments. As shown in purple and blue in Figure 10, we fit to three peaks

in the coordinated region: one at  $\sim 3450\text{ cm}^{-1}$  arising from hydrogen bonding with the other OH oscillator on free OH water (the companion mode), and two at  $\sim 3330$  and  $\sim 3203\text{ cm}^{-1}$  due to more tetrahedrally bound water. These fitting parameters for the neat air/water interface were determined by computational studies<sup>58,86,93</sup> and isotopic dilution experiments<sup>58,59</sup> that incrementally increased the concentration of  $\text{D}_2\text{O}$  in water, allowing for decoupling of the various hydrogen bonding interactions. Moreover, these fitting parameters capture the behavior of the water stretching region even when incident visible and IR beam angles change, resulting in differences in the relative intensities between the modes. While the community still discusses the specific assignments of the water structure in the stretching region, a strong consensus has been found in the overall shape and interpretation of the VSF spectra of the neat air/water interface.<sup>94</sup>

Of the component fits to the neat air/water interface, the phase terms for the free OH feature and the remaining three resonant peaks differ. The free OH peak is assigned a phase of 0, or pointing out of the surface, while the more hydrogen-bonded modes are assigned a phase of  $\pi$ , or pointing down into the bulk. Extensive literature in the phase sensitive VSF community, which is able to experimentally determine the phases of component modes, showed these phase assignments to be accurate but lacking an additional positive (0) mode detected below  $3250\text{ cm}^{-1}$ .<sup>26,95,96</sup> However, recent reassessment of this positive-phase mode reveals it arose solely from an experimental artifact rather than being characteristic of the water surface,<sup>97</sup> validating the original fitting parameters presented here.

### *The Bending Region*

The intensity and shape of the stretching region at the neat air/water interface largely arises from symmetric and asymmetric stretches of water, greatly broadened by the vast hydrogen bonding network at the surface.<sup>25</sup> In the bending region, from 1800–1000  $\text{cm}^{-1}$ , the water bending oscillator is largely isolated from the intermolecular influences that congest the stretching spectrum. As a result, the bending mode has been posited as a potential local probe of hydrogen bonding, while also facilitating energy loss from the stretching modes.<sup>61,83</sup> This suggests the bending mode is rather insensitive compared to the stretching mode to changes in hydrogen bonding, but a convenient metric for librational (rotational, translational) changes to the water structure.

Literature reports VSF spectra of the neat air/water bending mode in both *ssp* and *ppp* polarization.<sup>61,83</sup> Figure 11 shows experimental spectra of the water bend in both the *ssp* and *sps* polarization schemes, with the components to the fits labeled underneath the total fit in black. Literature assigns three peaks in the bending region from 1800–1400  $\text{cm}^{-1}$ : one arising at 1656–1640  $\text{cm}^{-1}$  from the bend of waters with a free OH oscillator (green); the second arising at 1750–1730  $\text{cm}^{-1}$  from the bends of the more coordinated waters (blue); and the third arising  $<1500 \text{ cm}^{-1}$  from the long tail of a librational mode at  $\sim 700 \text{ cm}^{-1}$  (red). The bending mode in *ssp* of Figure 11 largely matches that reported by Bonn, et al.,<sup>83</sup> with the three fitted spectral features within error to those reported by Benderskii,<sup>61</sup> but with a greater separation between the dominant mode at 1642  $\text{cm}^{-1}$  and the less intense mode at 1765  $\text{cm}^{-1}$ . The peak positions in Figure 11 arise from a global fit of the *ssp* and *sps* polarization spectra, holding everything fixed except the amplitudes of all modes and the peak position of the dominant  $\sim 1620$ –

1650  $\text{cm}^{-1}$  mode. An unreasonable fit was achieved if the mode at  $\sim 1620\text{--}1650 \text{ cm}^{-1}$  was not allowed to vary in position between the spectra. The differences in peak position between the free OH bend in *ssp* versus *sps* is not entirely surprising given the same feature shifts over 14  $\text{cm}^{-1}$  between reported *ssp* and *ppp* spectra.<sup>61</sup>

The phases of the features in the bending region mirror those of the stretching region as well, with the feature assigned to the bend of the free OH having a phase of 0 and the feature assigned to the bend of coordinated waters having a phase of  $\pi$ . This phase similarity between the bending and stretching modes of water is unsurprising, given the same oscillators contribute to both

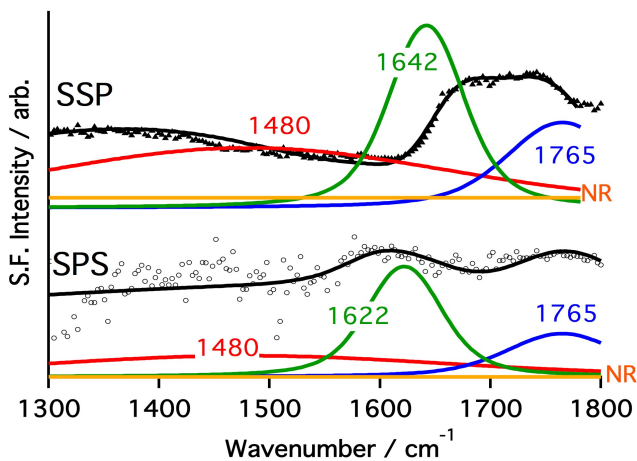


FIGURE 11. VSF spectra in the vibrational bending region of the neat air/water interface shown in black with resonant mode fits as the solid black line (total) with fit components in blue (coordinated OH), green (free OH), and red (librational water motions) in both the *ssp* (top) and *sps* (bottom) polarization schemes

modes and are thus not in unique orientations relative to the surface. Additionally the molecular symmetry of the fundamental symmetric stretch of the water ( $A_1$ ) is the same as the bending vibration ( $A_1$ ) further indicating the modes for the bend and stretch should be in phase.

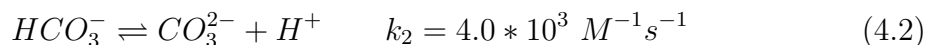
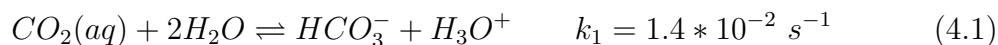
## Changes to the Vapor/Water Interface

Changes to the neat air/water interface manifest in unique ways in the bending and stretching regions. The stretching region can inform on the hydrogen bonding environment and coordination strength of various solutes, with blue shifting of modes indicating the oscillator resides in a more gas-like environment (in the vapor phase) while red shifting of modes indicates increased solvation (in the condensed phase). In the bending region, this trend is reversed, with blue shifting an indication of increased solvation. Additionally, in the bending region these spectral shifts are much subtler, a factor of roughly 4 times smaller than the same shift in the stretching region.<sup>98</sup> Likewise, changes in intensity between the free OH and more coordinated OH oscillators can indicate changes in solvation or hydrogen-bonding structure. For example, when the neat air/water interface is cooled from room temperature to 0°C, an increase in intensity is observed in the tetrahedrally coordinated water modes of the stretching region around  $\sim 3200\text{ cm}^{-1}$ , indicating the surface water increases in ice-like structure.<sup>19</sup> In the bending region this temperature change causes the coordinated water bend around  $\sim 1750\text{ cm}^{-1}$  to instead decrease in intensity, again due to increased ice-like structure that suppresses the bending vibration.<sup>61</sup> These seemingly converse effects manifest in a clearer overall picture of the behavior and structure of interfacial species, largely due to the different energetics associated with these two normal modes. Examining these two spectral regions in light of perturbations to the interface will be the subject of the remainder of this dissertation.

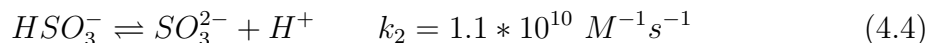
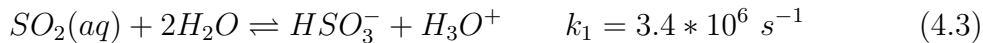
### *Acidic Vapor/Water Interfaces*

When solutes or reacting gases are introduced to the neat vapor/water interface, interesting spectral changes result. For the purposes of this dissertation, we're focused

on the surface reactions of gaseous CO<sub>2</sub> and SO<sub>2</sub>, typically in the presence of reactive amines. However, as we'll demonstrate in the next chapter, these amine surfaces are to a large extent water, to such a degree that the aqueous phase chemistry of these acidic gases beg consideration. In water, CO<sub>2</sub> and SO<sub>2</sub> readily dissolve, and undergo similar reaction mechanisms, although their reaction rates and Henry's law solubilities are quite different. The addition of CO<sub>2</sub> and SO<sub>2</sub> in water follows the following reaction mechanisms:<sup>99,100</sup>



and



with the associated Henry's law solubilities of 0.034 mol L<sup>-1</sup> atm<sup>-1</sup> for CO<sub>2</sub> and 1.22 mol L<sup>-1</sup> atm<sup>-1</sup> for SO<sub>2</sub>.<sup>99</sup> Despite their similar chemistry with water, CO<sub>2</sub> and SO<sub>2</sub> exhibit different overall rates of reaction that manifest in faster and greater acidification of water in an SO<sub>2</sub> atmosphere than a CO<sub>2</sub> atmosphere. Moreover, as shown in Figure 12, SO<sub>2</sub>(g) forms a surface-complex at the vapor/water interface, while CO<sub>2</sub> does not.<sup>101</sup> This surface-complex is evidenced by the broadening of the free OH feature around 3650 cm<sup>-1</sup> in Figure 12c, and shown computationally to arise from reorientation of surface waters to better accommodate interactions with SO<sub>2</sub>.<sup>102</sup>

Unlike SO<sub>2</sub>, little spectroscopic evidence exists to show CO<sub>2</sub> adsorbs at the vapor/water interface in the stretching region. Instead, as shown in Figure 12a,

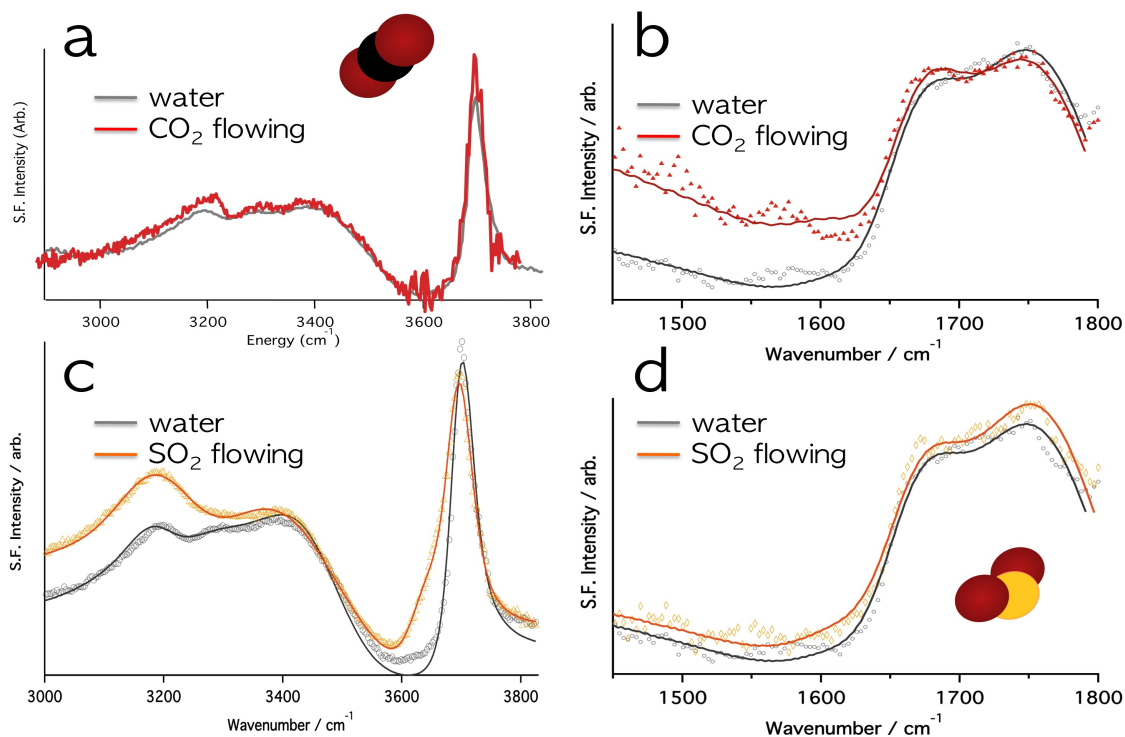


FIGURE 12. VSF spectra in the vibrational stretching (a, c) and bending (b, d) regions of the vapor/water interface, with the neat air/water spectra shown in grey and in an acidic gas environment in red ( $\text{CO}_2$ ; a, b) and orange ( $\text{SO}_2$ ; c, d)

$\text{CO}_2$ 's interaction with water only results in a slight increase in the tetrahedrally coordinated water modes around  $\sim 3200 \text{ cm}^{-1}$  due to increased ordering of water molecules around charged carbonate and bicarbonate ions. This same increase in intensity is equally observed during  $\text{SO}_2$  uptake, but to a greater extent, indicating ion formation of sulfites during  $\text{SO}_2$  flow in accordance with the reaction mechanisms of Equations (4.3) and (4.4) mentioned above.

In the bending region in Figure 12b and 12d, the uptake of  $\text{CO}_2$  and  $\text{SO}_2$  to the water surface shows different behavior than observed in the stretching region: no change (within error) is observed in the  $\text{SO}_2$  spectra while an increase in intensity of the libration mode is observed in the  $\text{CO}_2$  spectra. This noticeable difference in the libration of water under a  $\text{CO}_2$  atmosphere relative to an  $\text{SO}_2$  atmosphere could speak to the differing geometries the  $\text{CO}_2$  and  $\text{SO}_2$  reaction

products take in the water structure. Carbonate forms loose hydrated structures and strong hydrogen bonds with solvating water, causing slower relaxation rates of the water structure.<sup>103</sup> Sulfite, however, forms clathrate structures within the existing water network, and minimizes water exchange rates relative to neat solutions.<sup>104</sup> These differing ion effects to the water structure could manifest in the carbonate inducing slower librational motion in the water network, broadening the VSF libration signal; whereas the sulfite could largely orient the water network, but occupy “empty” space within the water structure manifesting as an unchanged VSF libration signal.

It is reasonable to assume the increase in the CO<sub>2</sub> spectra in Figure 12b could solely arise from increased librational changes to the water network due to differences in ion adsorption. However, as shown in Figure 13, the bending region has strong influences from overlapping resonant signals that also bear consideration. CO<sub>2</sub> reacts with water to produce bicarbonate and carbonate ions. Bicarbonate has a very strong carboxylate COO<sup>-</sup> resonance at  $\sim 1400\text{ cm}^{-1}$ , which has a long spectral tail that influences the underlying water structure in the bending

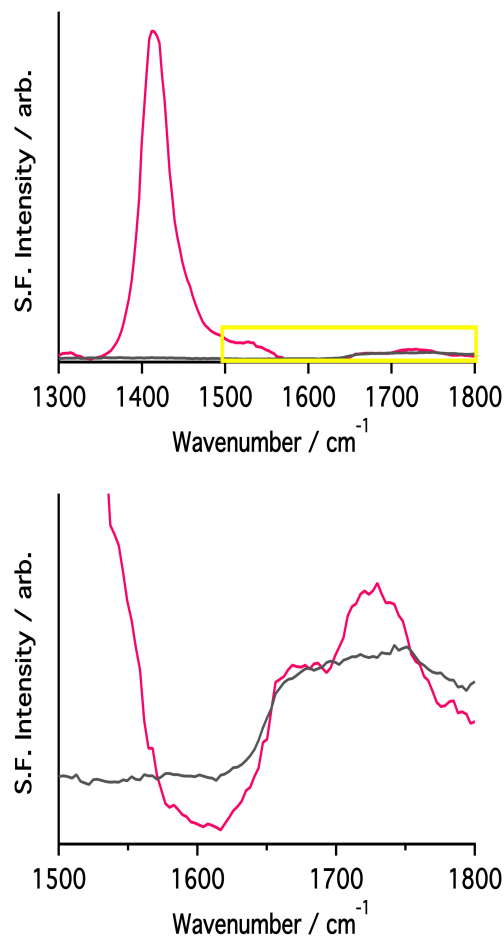


FIGURE 13. VSF spectra of 1 M NaHCO<sub>3</sub> (pink) from 1300–1800 cm<sup>-1</sup> (top), and magnified around the yellow box to 1500–1800 cm<sup>-1</sup> (bottom). The neat water spectrum (grey) is shown for reference.



region. As shown in the top trace of Figure 13, the large carboxylate peak at  $\sim 1400\text{ cm}^{-1}$  manifests in large increases in the water structure out to  $\sim 1600\text{ cm}^{-1}$ . And while this carboxylate peak wasn't observed in the  $\text{CO}_2$  data of Figure 12b, the presence of the carboxylate resonance due to adsorbed bicarbonate ions could manifest in spectral changes in the bending region that might otherwise be ascribed to the water network alone.

Thus, in examining the stretching region during acidic gas flow we find large intensity increases with  $\text{SO}_2$  in both the free OH and coordinated water region, but find minimal change in intensity with  $\text{CO}_2$ . In the bending region, the opposite trend is observed, with a large intensity change observed in the lower energy mode of water during  $\text{CO}_2$  flow. This change in intensity of the water bending mode with  $\text{CO}_2$  may arise from changes in the water structure due to the presence of ions or may arise from a convolution with long spectral tails from ion resonances. Taken together, these data indicate both  $\text{SO}_2$  and  $\text{CO}_2$  are absorbed to the water surface.  $\text{SO}_2$ , which forms surface complexes with the free-OH and increases hydrogen-bonding structure, has a greater impact on the surface water.  $\text{CO}_2$ , which forms looser hydrated structures with water, impacts the sub-surface water network. Comparing the stretching and bending regions allows for greater insight into the overall interfacial picture, especially when care is needed to deconvolve and interpret spectral changes.

## Conclusions

Examining the interfacial chemistry at complex surfaces requires a fundamental understanding of all the species involved. In the systems of this dissertation, aqueous phase chemistry and behavior dominates. Therefore, a fundamental understanding of the underlying water structure is essential to understanding the complexity of

these reacting systems. As shown in the uptake studies of  $\text{CO}_2$  and  $\text{SO}_2$  to neat water, examining both the stretching and bending regions of the vibrational spectrum elucidates a fuller picture than either region alone. The fitting parameters and structural interpretations in this chapter will lay the foundation for the experiments in the remainder of this dissertation. Throughout, the impact of adsorbed species to the underlying water structure will be considered and discussed.

## CHAPTER V

### BEHAVIOR OF MEA AT THE VAPOR/WATER INTERFACE

Monoethanolamine, or MEA, is the benchmark chemical in carbon capture technologies. Understanding the surface behavior of aqueous MEA will not only provide insight for the design of future carbon capturing amines, but will provide the foundation for the acidic uptake studies of subsequent chapters. This chapter begins with the spectra of MEA, and discusses the necessary mode assignments for identifying and understanding MEA surface behavior. A discussion of bending mode assignments based on structurally analogous molecules follows, as well as a brief discussion of previous bending mode spectra acquired alongside the multi-photon process mentioned in Chapter III. Computationally derived spectra will be compared to experimental spectra, with frequencies of MEA resonant modes and their assignments listed. The chapter will conclude with a discussion of the surface dynamics of MEA involving its surface preference and preferred surface orientation. This work has been published previously.<sup>17</sup> Dr. Sumi Wren and Dr. Nicholas Valley aided in the initial stages. I designed and conducted all experiments, and wrote all aspects of the manuscript.

#### **Introduction**

Aqueous amine solutions are prominent in carbon capture technologies, largely due to their classic donor-acceptor interactions with CO<sub>2</sub>,<sup>105</sup> and their energetically favorable heats of CO<sub>2</sub> sorption.<sup>106</sup> Aqueous solutions reduce the viscosity of the amine which increases CO<sub>2</sub> diffusion, and act to catalyze proton transfer throughout the reaction.<sup>40,105-108</sup> Monoethanolamine, a small organic amine shown in Figure

14, has been used in CO<sub>2</sub> capture technologies for decades.<sup>3</sup> MEA's lone pair electrons are accepted by CO<sub>2</sub>'s empty orbital to form carbamate or carbamic acid.<sup>105</sup>



FIGURE 14. MEA

While a handful of studies have examined the surface behavior of neat and aqueous MEA solutions,<sup>109–111</sup> the underlying physical chemistry of this reactive system has yet to be explored. In fact, some uncertainty still persists regarding the dominant reaction mechanism of CO<sub>2</sub> uptake to this seemingly simple system,<sup>112</sup> as will be discussed in Chapter VII.

This chapter seeks to examine the fundamental surface behavior of monoethanolamine. MEA is reactive and water soluble, making understanding the solution dynamics between the bulk and the surface necessary to understanding the behavior of the solution prior to absorption of gases. Moreover, as the first line of interaction between gas-phase CO<sub>2</sub> and the bulk, the surface behavior and structure of MEA could provide insight into fundamental uptake behavior. Recent engineering strategies and modeling have indicated the importance of interfacial chemistry in uptake and scrubbing.<sup>11,14,113,114</sup> The experiments of this chapter show MEA to be surface active and strongly oriented at an aqueous surface, such that MEA's nitrogen lone pair is pointing out toward the gas phase, available for reaction. This chapter also showcases the robustness of the combined experimental approach, with the sum frequency data convincingly captured with computationally derived results.

### MEA Spectral Response

Figure 15 shows vibrational sum frequency spectra of a concentration series of MEA solutions (1 M, 5 M, and 10 M MEA in H<sub>2</sub>O) at the air/water interface in *ssp*-polarization in the stretching region of the vibrational spectrum.

The VSF spectrum of the neat air/water interface is shown for reference in grey. Characteristic modes of neat water are present in the bottom, grey trace and agree well with the extensive literature of this interface.<sup>26,58,59,94</sup> Intensity due to free OH oscillators ( $\sim 3700\text{ cm}^{-1}$ ) as well as a broad feature ( $< 3500\text{ cm}^{-1}$ ) due to a continuum of more coordinated water oscillators is present.

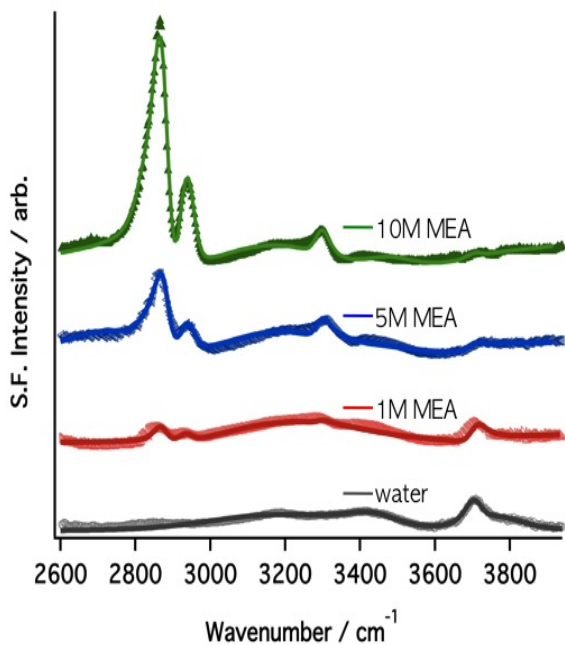


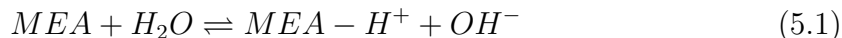
FIGURE 15. VSF spectra of aqueous monoethanolamine solutions at the air-water interface acquired using the *ssp*-polarization scheme in the CH/OH stretching region. Experimental data (shapes) and corresponding fits (solid lines) are offset for clarity.

Upon introducing MEA to solution, vibrational signatures characteristic to the  $\text{NH}_2$  and  $\text{CH}_2$  stretches ( $\sim 3287\text{ cm}^{-1}$ , and  $\sim 2936\text{ cm}^{-1}$  &  $\sim 2875\text{ cm}^{-1}$ , respectively) appear above the water structure. These new modes are present at all measured concentrations of MEA, showing MEA to be not only present at the surface but also ordered, as the relationship in Equation (2.5) details. All MEA spectra were globally fit, and achieved a reasonable match for all concentrations without allowing peak position, phase, or broadening to vary.

The only fitting parameter that needed varying between the concentration sets was the peak amplitude. This lack of change in fitted modes with changing bulk concentration suggest MEA does not reorient within the concentration regime under study, even if the bulk concentration changes by an order of magnitude. Instead, the changes in spectral intensity in Figure 15

could be due to changes in bulk concentration alone. This would suggest MEA is either isolated at the surface, orientationally constrained, or both. Yet, because VSF intensity arises from a convolution of both surface population and molecular orientation, a more thorough analysis of both the surface population and molecular orientation is required before a full interpretation of the changes in the spectra of Figure 15 can be understood.

In analyzing the aqueous MEA spectra of Figure 15, contributions from reaction products between water and MEA deserve consideration. An equilibrium between MEA and its protonated form, MEA-H<sup>+</sup>, exists in water according to Equation 5.1, with a pK<sub>b</sub> of 4.45.<sup>14</sup>



However, at the experimental pH ( $\sim 12.5$ ) the concentration of MEA-H<sup>+</sup> ( $\sim 10^{-2}$  M) is considered negligible. Additionally, protonation of amines is known to have dramatic effects on the VSF spectral shape in the CH stretching region;<sup>31</sup> yet no such effect was observed in these data. Therefore effects of MEA-H<sup>+</sup> species on the VSF spectral shape were neglected in these studies, but will be discussed in depth in the subsequent chapter.

In the bending region, as shown by the top two traces in Figure 16, characteristic resonances of the neat water and 10 M MEA solutions also give rise to VSF spectral intensity. The modes due to the free OH ( $\sim 1642$  cm<sup>-1</sup>) and more coordinated water oscillators ( $\sim 1765$  cm<sup>-1</sup>) are present in the top grey trace of Figure 16, and match the characteristic shape found in literature.<sup>61,83</sup> Additionally, vibrational signatures characteristic to the NH<sub>2</sub> ( $\sim 1601$  cm<sup>-1</sup>) and

CH<sub>2</sub> bends ( $\sim 1478\text{ cm}^{-1}$ ,  $\sim 1412\text{ cm}^{-1}$ , and  $\sim 1340\text{ cm}^{-1}$ ) of MEA appear above the water structure, shown by the topmost green trace of Figure 16.

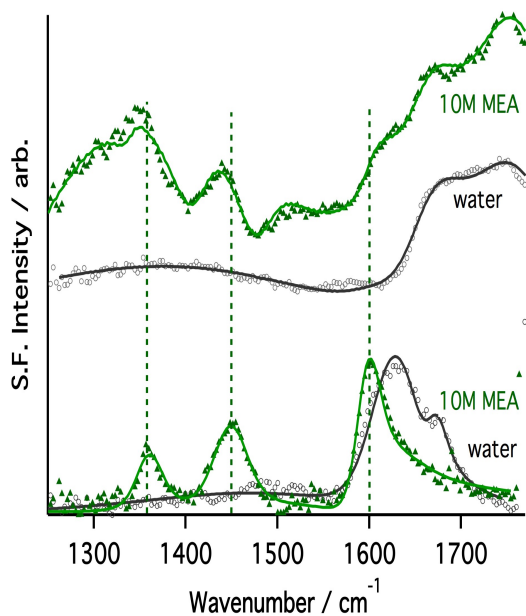


FIGURE 16. VSF spectra in *ssp*-polarization of 10 M MEA solution (green) and neat water (grey). Correctly acquired VSF data (top) and VSF data convoluted with an IR+IR+vis response (bottom) are offset for clarity. The dotted vertical lines act as visual guides for MEA resonant modes.

The bottom trace in Figure 16 shows the same solutions (neat water, grey; and 10 M MEA, green) acquired in the same spectral region with the same laser system and same incident angles, but lacking appropriate experimental safeguards to ensure a multi-photon process was not acquired along with the desired VSF spectra, as was described in Chapter III. For the amine spectra in green, the addition of the multi-photon process causes all resonant features to appear sharper and the background

water contribution—which dominates in the bending region due to water’s nearby libration—to be substantially minimized. The much improved signal-to-noise in the bottom traces of Figure 16 seems to suggest the multi-photon process could be utilized to improve spectral resolution and peak assignments in this spectrally congested region. But this is false reasoning. While the peak frequencies and general trends observed for the data acquired with the added multi-photon process (bottom) match those observed without the process (top), the convolution of modes in VSF makes this coincidence a unique case. Rather, the added influence of other

resonant modes from multi-photon processes would make spectral interpretation near impossible. Therefore, all further data are acquired with appropriate removal of the IR+IR+vis process, ensuring the resonant responses observed result solely from the VSF process.

## **Spectral Assignments: Comparison of VSF Spectra**

### *Experimental VSF Spectra*

In the stretching region of the vibrational spectrum of Figure 15, six peaks arise above the background water spectrum and are due to MEA's methylene and amine groups. The experimental VSF spectra were fit to peaks at  $2846\text{ cm}^{-1}$ ,  $2875\text{ cm}^{-1}$ ,  $2910\text{ cm}^{-1}$ ,  $2936\text{ cm}^{-1}$ ,  $3287\text{ cm}^{-1}$  and  $3345\text{ cm}^{-1}$ , as listed in Table 2. A peak at  $3200\text{ cm}^{-1}$  was also found to be necessary in the global fit, and is assigned to the hydroxyl group of the MEA but is strongly buried within the coordinated water structure. As VSF intensities depend upon vibrational transitions being both IR and Raman active, bulk IR and Raman studies are often used to guide identification of peaks in VSF spectroscopy. As such, bulk IR and Raman studies of MEA were examined to help identify the peaks in these VSF stretching region spectra. Knop, et al. and Jackson, et al. both report FTIR for neat MEA, attributing peaks at  $\sim 3290\text{ cm}^{-1}$  and  $\sim 3354\text{ cm}^{-1}$  to MEA's amine SS-NH<sub>2</sub> and AS-NH<sub>2</sub>, respectively.<sup>115,116</sup> Additionally, peaks at  $2864\text{ cm}^{-1}$  and  $\sim 2930\text{ cm}^{-1}$  are attributed to the CH-stretching bands; the peak at  $3180\text{ cm}^{-1}$  is attributed to MEA's alcohol OH stretch. Raman frequencies were reported by Samarakoon, et al. for  $\sim 3\text{ M}$  MEA solutions.<sup>117</sup> They report peaks at  $3313\text{ cm}^{-1}$ ,  $2952\text{ cm}^{-1}$ ,  $2940\text{ cm}^{-1}$  and  $2884\text{ cm}^{-1}$ , but do not assign the spectra. The stretching vibrational modes of MEA, especially those associated with the amine and alcohol groups, are expected to



TABLE 2. Frequencies and assignments of peaks from experimental and calculated *ssp* VSF spectra. Experimental frequencies are from global fits of *ssp* spectra taken at incident angles 45° (visible) and 60° (IR). Calculated frequencies are anharmonic VPT2 frequencies calculated at the B2PLYP/6-311++G (2d,2p) level of theory. Fits to water resonances are not included for clarity.

Experimental Frequencies ( $\text{cm}^{-1} \pm 10 \text{ cm}^{-1}$ )	Calculated Frequencies ( $\text{cm}^{-1}$ )	Assignment (mode)
1340	1355	CH <sub>2</sub> wag (+ NH <sub>2</sub> , CH <sub>2</sub> rock)
1412	1427, 1403	CH <sub>2</sub> wag (+ OH def.)
1478	1495	CH <sub>2</sub> scissor/bend
1601	1610	NH <sub>2</sub> scissor/bend
2846	2814	SS-CH <sub>2</sub>
2875	2827	SS-CH <sub>2</sub>
2910	2916	AS-CH <sub>2</sub>
2936	2968	AS-CH <sub>2</sub> (or FR-CH <sub>2</sub> )
3200	3556	OH stretch
3287	3340, 3391	SS-NH <sub>2</sub>
3345	3425	AS-NH <sub>2</sub>

red shift upon dilution with water due to solvation of MEA and subsequent loss of MEA dimers present in neat solutions.<sup>118</sup>

Based off these literature peak positions and assignments, it thus follows that the peaks observed at 3345  $\text{cm}^{-1}$  and 3287  $\text{cm}^{-1}$  are the AS-NH<sub>2</sub> and SS-NH<sub>2</sub> modes, respectively. The broad peak at 3200  $\text{cm}^{-1}$  is the solvated OH mode of MEA; however, due to hydrogen bonding as well as spectral coherence with the solvent OH modes, its spectral intensity is diminished. The modes at 2936  $\text{cm}^{-1}$ , 2910  $\text{cm}^{-1}$ , 2875  $\text{cm}^{-1}$ , and 2846  $\text{cm}^{-1}$  are the CH stretching modes of the methylene backbone. The literature alone does not enable complete assignment for all four modes. Fortunately, due to different polarization selection rules for the methylene SS and AS modes, polarization analysis can be exploited to aide in assigning experimental peaks.<sup>28,30</sup>

As outlined by Lu, et al. and described in Chapter II, comparison of *ssp* and *sps* relative peak intensities allow for mode assignments of methylene peaks to

be made.<sup>30</sup> Figure 17 shows *ssp* and *sps* spectra for 10 M MEA solution in the CH stretching region. Vertical lines act as guides to identify CH intensity due to peaks fit at 2936  $\text{cm}^{-1}$ , 2910  $\text{cm}^{-1}$ , and 2875  $\text{cm}^{-1}$ . One methylene selection rule states that the SS-CH<sub>2</sub> and AS-CH<sub>2</sub> modes should be out of phase in *ssp* spectra.

Indeed, as confirmed by the spectral fits

of Figure 15, the peaks at 2875  $\text{cm}^{-1}$  and 2910  $\text{cm}^{-1}$  are opposite phases.

Additionally, the peak at 2910  $\text{cm}^{-1}$  in *sps* has a higher fitted amplitude than the same peak in *ssp*. The methylene group selection rules dictate the peak at 2910  $\text{cm}^{-1}$  should therefore

be the AS-CH<sub>2</sub> mode; thus making the peak at 2875  $\text{cm}^{-1}$  the SS-CH<sub>2</sub> mode.

Unfortunately, these selection rules alone are unable to accurately assign the two remaining methylene modes. The selection rules are based on molecular

symmetry arguments and assume the methylene backbone of MEA is uncoupled from

the motion of the rest of the molecule. This last assumption is not well-satisfied for MEA, as its functional groups alter the coupling between the methylene stretches.

Similar analysis—taking into account calculated frequencies and literature precedent—was conducted for MEA in the bending region of the vibrational spectrum. As listed in Table 2, four peaks are uniquely fit to MEA in the bending region: at 1601  $\text{cm}^{-1}$ , 1478  $\text{cm}^{-1}$ , 1412  $\text{cm}^{-1}$ , and 1340  $\text{cm}^{-1}$ . A broad contribution also arises

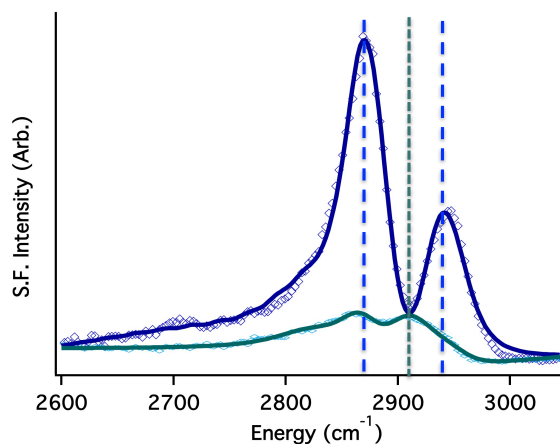


FIGURE 17. VSF spectra of 10 M MEA solutions in *ssp*- (purple, diamonds) and *sps*-polarization (teal, circles) in the CH stretching region. Experimental data (open shapes) and corresponding fits (solid lines) are shown. Incident beam angles for both polarizations were 63° (visible) and 55° (IR).

from the MEA hydroxyl at  $1250\text{ cm}^{-1}$ , but is largely convoluted with the background water. FTIR studies report peaks at  $1645\text{ cm}^{-1}$  and  $\sim 1600\text{ cm}^{-1}$  assigned to NH rocking.<sup>116,119</sup> Peaks at  $\sim 1450\text{ cm}^{-1}$  and  $\sim 1360\text{ cm}^{-1}$  appear in the reported spectra, but are either unassigned or assigned to the methylene bend or C–O–H bend.<sup>116</sup> Unfortunately, as the bending region of the vibrational spectrum is examined much less than the stretching region, few other sources exist to help identify peaks in this region.

To aide in the determination of the spectral assignments in the bending region, spectra were taken of 10 M MEA alongside 10 M EDA (ethylenediamine) and 10 M ETG (ethylene glycol), as shown in Figure 18. EDA and ETG are structurally analogous to MEA, with the important difference arising from their functional groups, with EDA having two amines and ETG, two hydroxyls. Globally fitting these three spectra enables identification and assignment of MEA spectral features. Figure 18 shows the individual components to the fits of MEA, EDA and ETG after the contributions from the water have been removed. Four unique peaks arise above the water structure in MEA, as was mentioned before, while five exist for EDA and only three for ETG. The three modes that arise in all three cases,  $1478\text{ cm}^{-1}$ ,  $1412\text{ cm}^{-1}$ , and  $1340\text{ cm}^{-1}$ , are assigned to the deformation and wags of the methylene backbone. The  $\text{CH}_2$  is the common structural group between these three molecules, and these peak positions are consistent with literature values for the  $\text{CH}_2$ .<sup>120</sup>

The broad OH deformation at  $1250\text{ cm}^{-1}$ , which is largely convoluted with the background water, shows increased intensity in the ETG spectrum relative to MEA. This is unsurprising, as the number of hydroxyl groups doubles from MEA to ETG. However, this mode is strongly coupled with other molecular modes, the water background modes, and molecular librations, making interpretation of its spectral

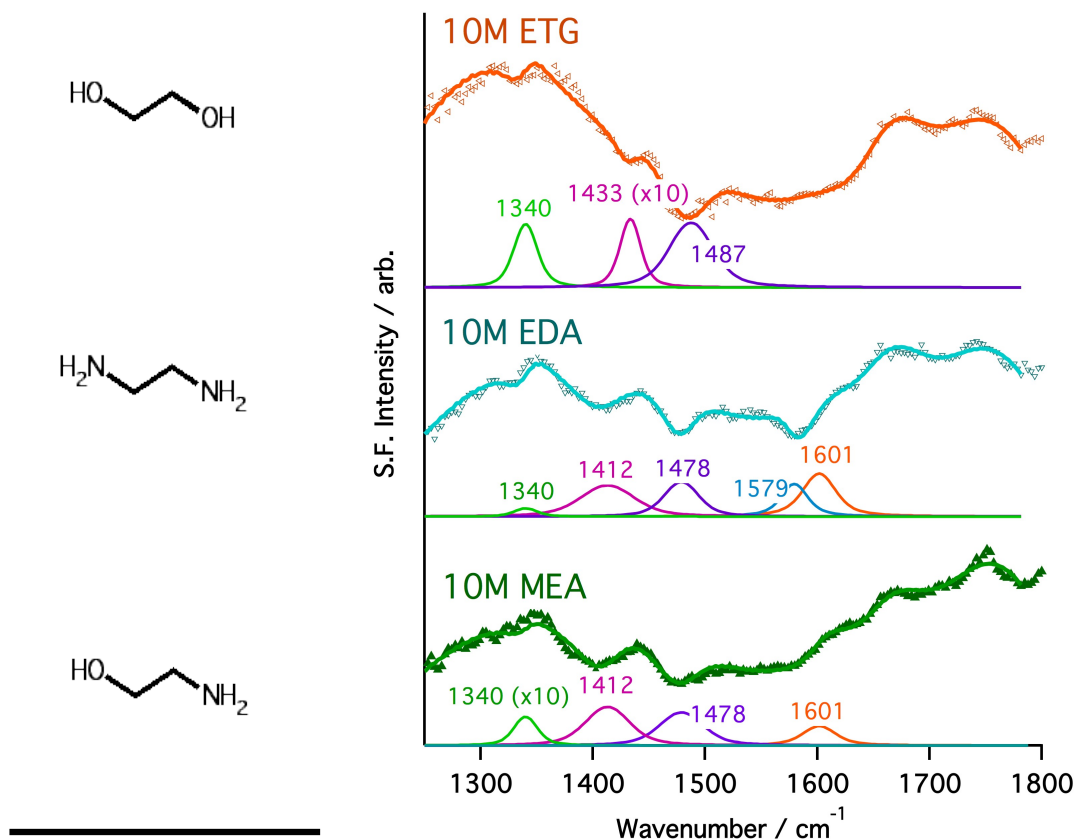


FIGURE 18. VSF spectra in the bending region in *ssp*-polarization of 10 M MEA (green, bottom), 10 M EDA (teal, middle), and 10 M ETG (orange, top) with their representative structures on the left. Experimental data (shapes) and corresponding fits (solid lines) are shown with individual component fits. The component fits arising from the water modes have been removed for clarity.

changes difficult. The shifts in frequency observed for some of the methylene modes in the ETG spectrum, in fact, largely arise from coherence effects with this OH deformation which couples with the methylene modes. The two modes which do not appear in ETG are present in EDA at  $1579\text{ cm}^{-1}$  and  $1601\text{ cm}^{-1}$ , while in MEA, only one peak at  $1601\text{ cm}^{-1}$  is present. These modes are assigned to the  $\text{NH}_2$  bend, consistent with the structure of the amines, and in agreement with literature values for the  $\text{NH}_2$ .<sup>116,119</sup> Two peaks are present in EDA due to different surface orientations of EDA's two amines.

Thus almost all resonant modes of MEA are assigned by employing spectroscopic techniques that enable discrete characterization of modes. However, in spectral regions where clarification isn't possible with such techniques, such as the coupled methylene stretches mentioned above, computational methodology is employed to assist with spectral interpretation and provide confirmation to already assigned modes.

### *Calculated VSF Spectra*

To resolve the uncertainty in the experimental spectral assignments, DFT at the B2PLYP/6-311G++(2d,2p) level of theory is used to calculate VSF spectra. Static gas-phase DFT structures are matched to surface conformers in the MD simulations. Assignments of the MD conformers to DFT structural "groups" are based on assigned ranges of specific dihedral angles; these ranges are listed in Appendix D. Calculated VSF spectra (orange) are shown in Figure 19 along with the fits to the experimental spectra (blue) for comparison. Peak positions are listed in Table 2. Note the calculated VSF spectra do not include solvent contributions; red shifting of the calculated peak frequencies for the amine and alcohol stretching modes is expected if solvation effects were included.

Figure 19b shows good agreement in both relative peak intensity and peak position for the CH stretching region. However, Figure 19a and 19c, look quite different, and indicate that solvent contributions play a large role in shaping the VSF spectra in the bending and NH stretching regions. Not only do the water OH modes greatly contribute intensity to the overall experimental line shape in Figure 19a and 19c, the solvation of MEA's functional groups lead to frequency shifts and spectral broadening of the NH and OH modes in the experimental spectra relative

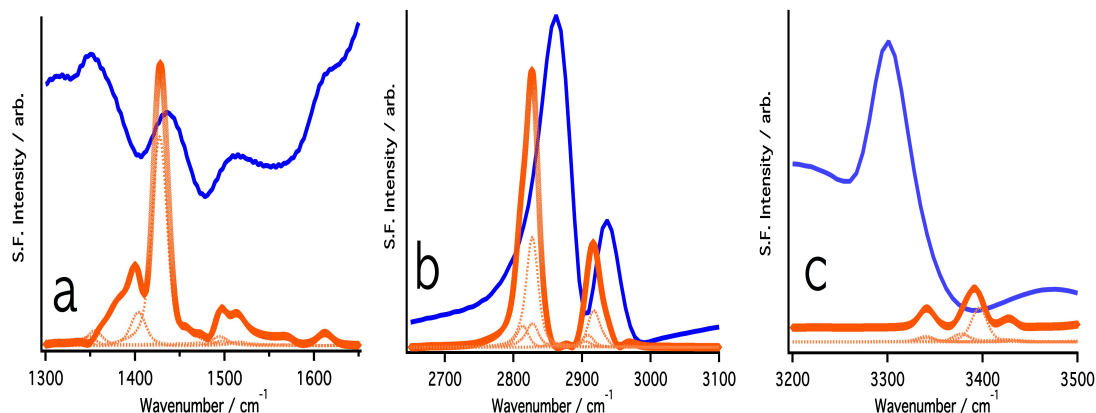


FIGURE 19. VSF spectra in *ssp*-polarization taken experimentally (blue) and calculated (orange) in (a) the bending region, (b) the CH stretching region, and (c) the NH stretching region. Note, the y-axes for (a), (b), and (c) are not comparable, but are scaled to allow calculated spectra to be observed. Dotted orange lines represent conformer contributions to the overall calculated VSF spectra.

to the calculated spectra. For example, the deviation in peak position ( $\pm\sigma$ ) between the calculated and experimental fit value of the NH stretching region is  $\sim 55\text{ cm}^{-1}$ . Relative intensities are also clearly affected by the solvent in the NH stretching region in Figure 19c. The background water structure can greatly impact the shape of the VSF spectra in the stretching region, resulting in greater mismatch between experiments and calculation. Moreover, NH stretches in amines and amides are notoriously difficult to accurately calculate with DFT, and are greatly influenced by solvent effects,<sup>121–123</sup> indicating the  $\sim 55\text{ cm}^{-1}$  deviation in peak position is not unreasonable. Nevertheless, in the CH stretching region of Figure 19b the solvent effects are lessened and result in an average deviation in peak position of  $\sim 21\text{ cm}^{-1}$ . This deviation in peak position not only indicates the CH region is favorable for examining spectra where solvent effects may be neglected, but also indicates strong agreement in peak frequencies exists between the experimental and DFT-derived spectra within this region.

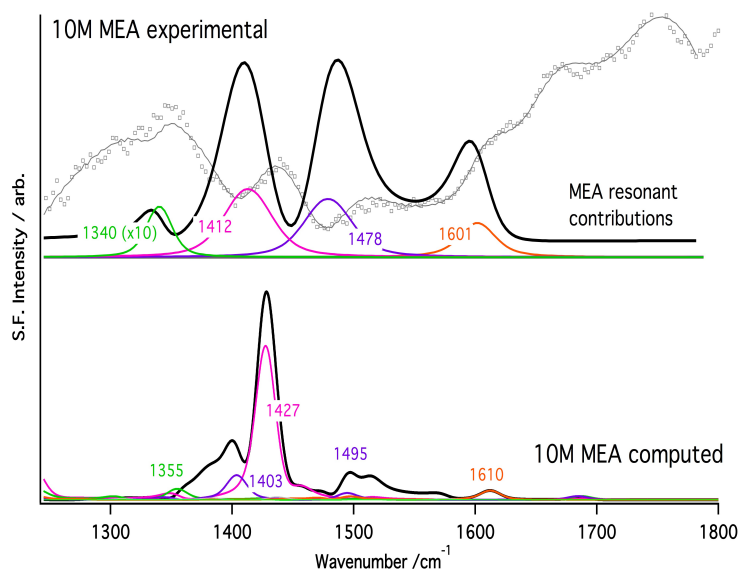


FIGURE 20. Computed (bottom) and experimental (top) VSF spectra of 10 M MEA solution in *ssp*-polarization in the bending region. Bottom: computed spectra show total in black with conformer contributions highlighted in color. Top: experimental spectra and total fit in grey, the total fit from only resonant modes in black, and components to the fits are colored.

Additionally, the DFT calculations show coupling between the methylene backbone modes, contrary to previous experimental assumptions. For example, the assignment of the peak at  $2875\text{ cm}^{-1}$  in the VSF spectra is  $\text{SS-CH}_2$  based off of literature precedent and polarization rules. In the calculated spectra, this peak appears at  $2827\text{ cm}^{-1}$  and arises instead from coupling between the two methylene units: a strong  $\text{SS-CH}_2$  contribution from one and a weaker  $\text{AS-CH}_2$  contribution from the other. This coupling behavior has been found to be characteristic for all the methylene stretches and bends calculated, and questions the assumption that each vibrational mode is discretely symmetric or asymmetric. Therefore, mode assignments in Table 2 are made taking into consideration the various strengths of these coupled vibrations, along with the literature assignments and polarization analysis presented above.

The calculated VSF spectra in the bending region in Figure 19a show good agreement in peak position with the experimental spectra, with an average deviation in peak position of  $\sim 9\text{ cm}^{-1}$ . However, the relative intensities of the calculated spectra when compared to the experimental spectra are markedly different. In the experimental spectra, intensity due to the water bend at  $1765\text{ cm}^{-1}$ ,  $1642\text{ cm}^{-1}$  and  $1480\text{ cm}^{-1}$  largely dwarfs the resonant contributions from MEA. However, if only the methylene groups' bending intensities are considered, the calculated spectra agree well with the experiment, as is shown in Figure 20. The top graph of Figure 20 shows the experimentally measured MEA spectrum (grey) with the fit to the data (grey, solid line). The contributions to the fit arising only from MEA resonant modes is shown in black, and provides a much better match to the computed MEA spectra. Thus, modes in the bending region are assigned as follows, based off of literature, analogous molecule studies, and calculated spectra: the peak at  $1601\text{ cm}^{-1}$  is the  $\text{NH}_2$  bend, and the peaks at  $1478\text{ cm}^{-1}$ ,  $1412\text{ cm}^{-1}$  and  $1340\text{ cm}^{-1}$  are  $\text{CH}_2$  bends and wags, as listed in Table 2.

### Surface Population Analysis

As mentioned previously, VSF intensity is due to both surface population and molecular orientation of surface species. Thus in order to fully interpret changes to VSF signal, changes to the surface population and molecular orientation of MEA also requires investigation. The surface activity of MEA has been the subject of previous study,<sup>109–111,124</sup> since its surface presence affects macroscopic parameters such as gas phase transfer rates and solution dynamics. MEA's surface population is investigated here in order to accurately interpret VSF spectra and to gain a complete picture of MEA's surface adsorption.



### Surface Pressure and Adsorption Calculations

Equilibrium surface tension values were obtained for aqueous MEA solutions (ranging from 0.5 M to pure MEA). Surface tensions were converted to surface pressures,  $\pi$  (the difference between the solution surface tension and the surface tension of neat water), and are plotted as a function of bulk MEA concentration in Figure 21. The use of surface pressure values facilitates comparison across data sets but, like surface tension, also reflects surface population. The surface pressure isotherm of MEA shows increases in surface pressure track increases in bulk concentration, indicating MEA is present at the surface and mirrors bulk concentration. The surface pressure values compare well with the trend reported by Vazquez, et al.,<sup>109</sup> considering differences in solution temperature between the two studies.

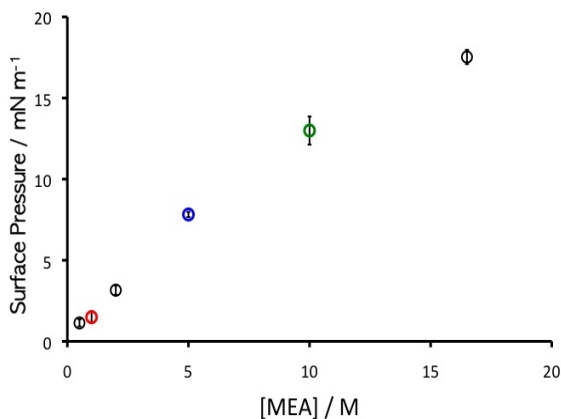


FIGURE 21. Surface pressure versus bulk concentration of MEA, with concentrations of VSF spectra from Figure 15 colored.

Both the minimum average surface area per molecule and the overall surface mole fraction are calculated from the surface pressure values using the Gibbs adsorption equations, as outlined in Chapter II. For these calculations, bulk concentrations of MEA were corrected with activity coefficients reported by Hilliard.<sup>125</sup> The minimum average surface area per

molecule was calculated to be  $\sim 126 \text{ \AA}^2$  per molecule. This large interfacial footprint is characteristic of other doubly functionalized molecules<sup>67</sup> and indicates MEA is

highly solvated at the surface, even at high concentrations. Additionally, the overall surface mole fraction of a 10 M MEA solution was calculated to be  $\sim 0.3$ , roughly equivalent to  $\sim 9.8$  M. For a 5 M solution, the surface mole fraction was calculated to be  $\sim 0.1$ , roughly equivalent to  $\sim 4.9$  M. These surface mole fractions indicate a fairly large surface density of MEA that roughly mirrors the bulk solution concentration. Taken together, the minimum average surface area per molecule and surface mole fraction suggest a largely solvated MEA surface structure with surface population closely tracking bulk solution concentration.

### *Density Profiles*

Surface population is also examined through density profile calculations. The density profile extracted from the molecular dynamics simulation of a  $\sim 10$  M MEA solution (160 molecules) is shown in Figure 22, and may be used to compare the interfacial picture developed from the surface pressure analysis with those from the simulated interfaces.

The density profiles show the density in the “bulk” (depths  $> 15$  Å) for the  $\sim 10$  M MEA solution to be  $\sim 1.01$  g/mL, corresponding well with densities measured experimentally.<sup>126,127</sup> At the surface, as shown in Figure 22, the total density of the solution decreases, but displays enhancement of MEA density relative to the bulk solution. This MEA surface enhancement appears contrary to the surface mole fraction calculated earlier, which suggested surface population of MEA roughly mirrors the bulk population. To investigate this discrepancy the surface mole fraction may be calculated from the density profiles, but only if rigorous accounting of the surface depth has been considered.

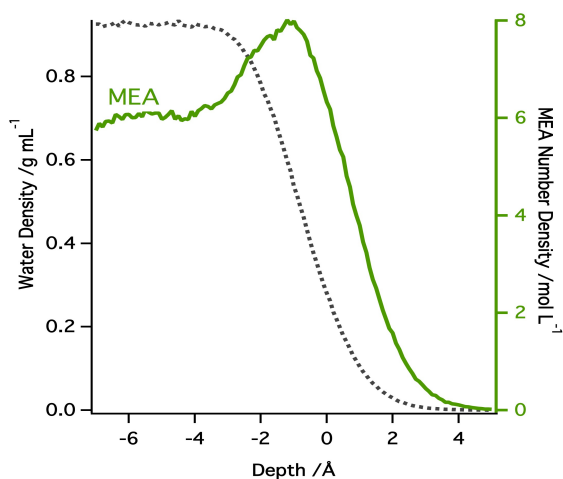


FIGURE 22. Density profile of water (grey dashed line) and  $\sim 10$  M MEA (green solid line) extracted after 52 ns of simulation time.

The computational surface analysis here, based on the Gibbs dividing surface, however, can be misleading and fail to accurately capture interfacial components. Recent computational work has sought to address these shortcomings of the Gibbs surface definition,<sup>128–132</sup> but issues regarding how to define the thickness of the surface layer, how surface behavior manifests on bulk behavior, and how changing composition reflects changes in interfacial thickness persist.<sup>133,134</sup> Within the community, the definition of the “surface” can range from 2 angstroms<sup>132,135</sup> to a nanometer,<sup>136,137</sup> with results between surface techniques (i.e. computed surfaces vs. surface tensiometry) varying due to different probe depths. Nevertheless, for VSF analysis a surface *region* is generally considered. From a regional approximation of Figure 22 ( $\pm 3$  Å from the Gibbs dividing surface), the average surface mole fraction is found to be  $\sim 0.267$  (or  $\sim 9$  M), roughly similar to that found in the surface pressure analysis, acknowledging the shortcomings of the interfacial definitions used.

Thus density profiles extracted from MD simulations together with experimental surface pressure measurements show MEA is concentrated at the solution interface, displaying surface activity and a population similar to the overall bulk. Therefore, intensity changes to the VSF spectra in Figure 15 likely result from increasing surface concentration that tracks with increasing bulk concentration. This interpretation of

The computational surface analysis here, based on the Gibbs dividing surface, however, can be misleading and fail to accurately capture interfacial components. Recent computational work has sought to address these shortcomings of the Gibbs surface definition,<sup>128–132</sup> but issues regarding how to define the thickness of the surface layer, how surface behavior manifests on bulk behavior, and how changing

the spectral changes in Figure 15 are confirmed by the surface pressure and density profile results along with the global fitting of the concentration series discussed previously. As a final check on the developing picture of MEA's surface behavior, the surface orientation of MEA at different concentrations is examined.

## Molecular Orientational Analysis

### *Orientalional Analysis via Molecular Dynamics Simulations*

Angular distributions extracted from the molecular dynamics trajectories report the average molecular tilt of bonds relative to the surface normal, giving information on MEA's surface orientation. Correlating the angular distributions of one bond relative to the other gives a sense for not only the orientation of the molecule relative to the surface but also the internal conformation the molecule adopts at the surface. Thus, an analysis of the correlated angular distributions of  $\sim 10$  M MEA was undertaken in order to understand MEA's surface orientation; representative distributions are shown in Figure 23.

In Figure 23a, the angular distribution of the C–O bond relative to the surface normal ( $\theta$ ) is plotted as a function of the angular distribution of the C–N bond relative to the surface normal ( $\phi$ ). The z-axis denotes population, with cooler colors (blue–green) denoting lower percentages of the population and warmer colors (yellow–red) denoting higher percentages of the population. In the bulk (depths  $>15$  Å), the correlated angular distribution of the backbone is isotropic. At the surface ( $0$  Å), however, a single, strong maxima appears. The correlated angular distribution at the surface shows a favored orientation of MEA, where the majority of MEA molecules adopt angles of  $\theta$  and  $\phi$  near  $\sim 140^\circ$ . These angles for  $\theta$  and  $\phi$  indicate both C–O and C–N bonds are pointing into the bulk. Additionally, this combination of angles

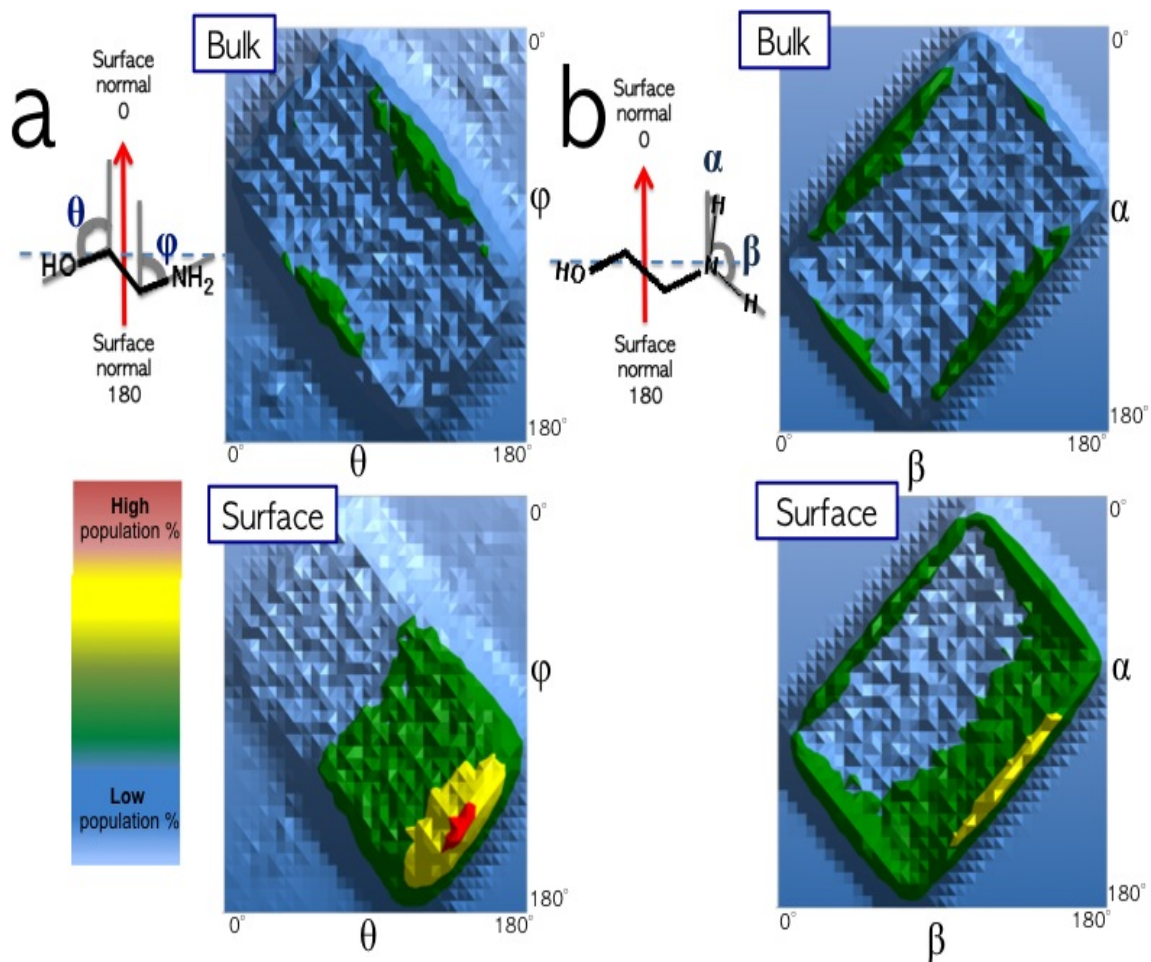


FIGURE 23. Correlated angular distributions in the bulk and surface region of  $\sim 10$  M MEA probing (a) the backbone orientation ( $\theta$  vs  $\phi$ ) and (b) the NH<sub>2</sub> orientation ( $\beta$  vs  $\alpha$ ). The color guides on the left describe the  $z$ -axis, where cooler colors equate to lower percent of total population while warmer colors equate to higher percent of total population.

corresponds to a gauche conformation of MEA's backbone at the surface. The gauche conformation of MEA is not wholly unexpected at the surface, as MEA has been shown to exist in the gauche conformation in neat solutions.<sup>118</sup> Integrating over the 2-D surface in Figure 23a confirms this picture, and shows  $\sim 98\%$  of the population exists in the gauche conformation.

Similarly, in Figure 23b the angular distribution of one N-H bond relative to surface normal ( $\beta$ ) is plotted as a function of the angular distribution of the other NH bond relative to the surface normal ( $\alpha$ ). Again, the z-axis denotes population, ranging from low percentages (cool colors) to high percentages (warm colors). For both bulk and surface regions, the NH<sub>2</sub> headgroup is fairly isotropic across the orientational space. However, at the surface there is a small maxima corresponding to angles of  $\alpha$  and  $\beta$  roughly around  $\sim 110^\circ$ – $140^\circ$ . This indicates that at the surface the NH<sub>2</sub> group tends to favor both N-H bonds pointing into the bulk water. Such an orientation would allow the NH<sub>2</sub> lone pair to be more open at the surface for reaction with gas phase CO<sub>2</sub>, indicating a possible route for surface chemistry.

The orientational MD analysis shows that surface-adsorbed MEA at  $\sim 10$  M adopts a constrained gauche conformation with its CH<sub>2</sub> groups pointing into the vapor phase and its amine and alcohol headgroups pointing into the bulk. Analysis of the MD simulations with  $\sim 5$  M MEA solution (not shown) show similar orientational behavior. Therefore, the behavior of MEA in the MD simulations indicates MEA surface orientation is not sensitive to concentration, supporting the interpretation that observed changes to the VSF spectra are largely a result of changing surface population.

### *Orientational Analysis via VSF Polarization Studies*

Polarization analysis of the experimental VSF spectra provides an additional means of extracting surface orientation information, complementing the MD analysis above. VSF intensity ratios are used to extract average orientational angles by following an analysis of the functional groups' polarization selection rules and rigorous normalization of spectra. The polarization selection rules of the methylene group have been extensively outlined<sup>27,28,30</sup> and were detailed in Chapter II. Following similar methodology, analysis of the methylene stretches was undertaken here, and compared to the orientational information from the molecular dynamics simulations.

Based on the SS-CH<sub>2</sub> and AS-CH<sub>2</sub> ratios in *ssp*-polarization detailed above, the average tilt angle of the methylene group in a 10 M MEA solution was found to be  $46 \pm 6^\circ$  from the surface normal. Tilt angles were also calculated for both 5 M and 1 M MEA solutions, and show the same value (within error)

for the average methylene tilt as the 10 M solution, indicating surface orientation is independent of concentration. These tilt angles for the methylene group are

consistent with the overall surface orientation inferred from the MD simulations.

In Figure 24, the angle of the bisector of the methylene group (extracted from MD) is averaged over all methylene twist angles in both the bulk of a  $\sim 10$  M MEA solution and at the surface. In the bulk, the methylene bisector is isotropic,

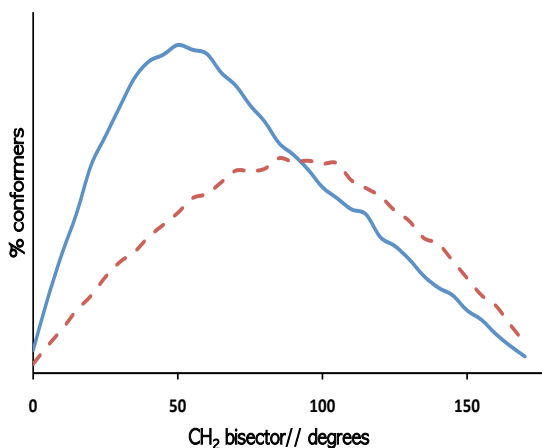


FIGURE 24. Angular distribution of  $\sim 10$  M MEA methylene bisector in both the bulk (red dashed) and at the surface (blue solid) averaged over all methylene twists.

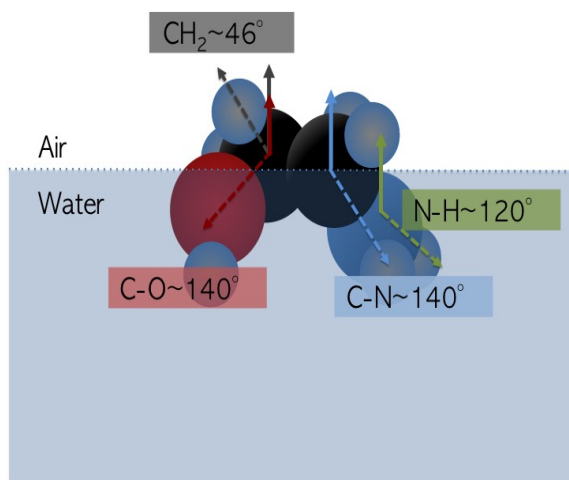


FIGURE 25. Generalized picture of MEA's surface orientation and conformation. Angles for  $\sim 10$  M MEA solution are shown.

consistent with the earlier orientational picture developed from the correlated angular distributions in Figure 23. At the surface the methylene groups are preferentially oriented  $\sim 45\text{--}50^\circ$  from surface normal. MD simulations therefore corroborate the polarization analysis of the experimental spectra, indicating the average tilt angle of the methylene groups at the surface to be  $\sim 46^\circ$  from surface normal.

The orientational analysis of MEA indicates an overall orientation as summarized in Figure 25. MEA favors a gauche conformation independent of concentration, at least in the high concentration regime. In light of the surface population analysis above, it is clear that the intensity changes present in the VSF concentration series in Figure 15 are the result of increasing population at the surface and not changes in surface orientation. This conclusion is also consistent with the large calculated interfacial footprint of MEA ( $\sim 126 \text{ \AA}^2/\text{molecule}$ ), indicating that even at large surface densities MEA still has sufficient space to adopt a favored orientation.



## Conclusions

As interest in aqueous alkanolamine solutions as sorbents in CO<sub>2</sub> capture has increased, so has the need to understand the molecular characteristics of the chemical constituents. The results of these studies provide important new insights into the molecular characteristics of MEA at an aqueous surface and how its adsorption at a surface might facilitate CO<sub>2</sub> capture. The results demonstrate that MEA exhibits similar concentration at the surface as in the bulk, and maintains a large interfacial area ( $\sim 126 \text{ \AA}^2/\text{molecule}$ ) even at high concentrations due to favorable solvation of MEA.

Additionally, this work demonstrates the validity of the combined experimental and computational approaches to detail liquid surfaces. Surface population was examined both experimentally, with surface pressure data, and computationally, with density profiles from the MD and showed remarkable agreement. The surface orientation of MEA was supported by analysis of the computational MD trajectories, as well as evaluation of the experimental *ssp* VSF spectra. Lastly, comparison of experimental and computational VSF spectra revealed strong agreement with regard to peak positions and relative intensities. Agreement was especially strong for the methylene backbone vibrations allowing for confident assignments of spectral modes.

This chapter provides a needed picture of MEA surface adsorption and orientation which is required for future investigation into its surface reactivity. Results from this work indicate the presence of an interface induces an ordering of MEA as well as a preferred conformation. The subsequent chapters will detail what happens to this MEA surface when perturbed by acidic species. The next chapter will explore how direct acidification with HCl, which causes a shift in the equilibrium between MEA and protonated MEA (Equation 5.1), influences the MEA surface. These pH

studies will provide insight into whether spectral changes due to acidification can be linked to spectral changes when CO<sub>2</sub> or SO<sub>2</sub> are introduced.

## CHAPTER VI

### BEHAVIOR OF MEA AT THE ACIDIFIED WATER INTERFACE

The previous chapter detailed the surface behavior of concentrated MEA solutions, showing MEA adsorbs to the air/water interface, orients such that its methylene groups and nitrogen lone pair electrons are pointing out toward the vapor, and is largely isolated with an interfacial area per molecule of  $\sim 126 \text{ \AA}^2$ . What is unknown is how this surface responds to changes due to ions, reaction with gas phase molecules, or acidification. These perturbations result when  $\text{CO}_2$  adsorbs to MEA surfaces, causing a drop in pH of over four orders of magnitude and formation of multiple ionic species. In order to decouple the spectral response of the  $\text{CO}_2$ -MEA reaction from spectral responses due to other perturbative effects, acidification of the MEA surface was examined through addition of HCl. This chapter reveals that pH changes to the aqueous MEA system dramatically shift the bulk equilibrium, but have minimal impact on the surface. Surface tension and some computational studies performed by Nina Vincent are discussed here in order to better describe the behavior of the acidified spectra. I designed all aspects of the experiments, acquired all VSF spectra, performed all molecular dynamics simulations, and wrote all aspects of the manuscript. This work will be published in a forthcoming paper.

#### Introduction

Acidification has been shown to have a dramatic effect on the vapor/water interface,<sup>88,138,139</sup> as well as impact adsorbed organic species residing there.<sup>20,31,140,141</sup> HCl, for instance, is known to rapidly dissociate ( $K_a = \sim 10^{3.8}$ )<sup>142</sup> in aqueous solution into  $\text{H}^+$  and  $\text{Cl}^-$  ions. The  $\text{H}^+$ , additionally, influences water's self ionization and

reacts with water to form  $H_3O^+$ . The  $H_3O^+$  ion is thought to exist at the vapor/water interface, causing changes in the orientation of surface water and increasing the intensity of the VSF spectral response.<sup>88,139,143</sup>

Surface adsorbed organics species, can equally respond to changes in pH. Organics acids, such as carboxylic acid containing diacids or polymers, exist in their protonated form under acidic conditions. As a result of their lack of charge, these carboxylic acids adsorb to the interface at low pH,<sup>140,144</sup> but if the pH is increased they desorb. For organic bases, the corollary might be expected. At high pH, many bases are neutral and expected to be present at the surface. Upon increased acidification, bases become positively charged, and will likely retreat from the surface. For MEA, a classic Brønsted base, increased acidification of the solution results in increased protonation of MEA, from  $NH_2$  to  $NH_3^+$ , according to Equation 6.1, with a  $pK_b$  of 4.45.<sup>14</sup>

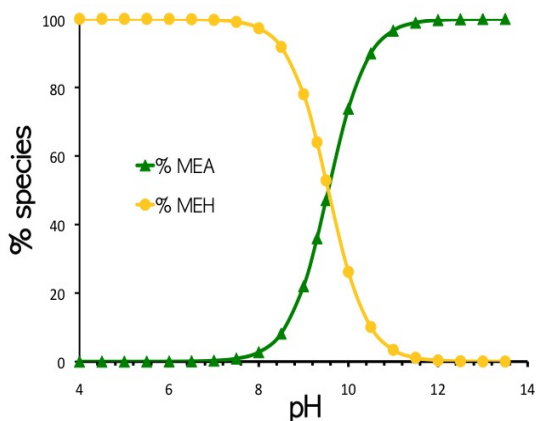
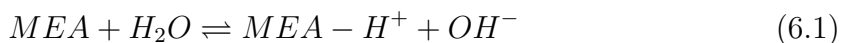


FIGURE 26. Percent change in concentration of MEA (green triangles) and MEH (yellow circles) with changing pH based on Equation 6.1.

The experiments of the previous chapter dealt with MEA solutions at their native pH,  $\sim 12.5$ , where  $\sim 97\%$  of the MEA is in its neutral form. For the acidified MEA solutions, a 10 M MEA sample is prepared in 36.5–38 wt.% HCl resulting in a solution pH  $\sim 9.3 \pm 0.8$ . This decrease in pH results in over 50% of MEA converting to protonated MEA, or “MEH”, as shown in Figure 26. At pH  $\sim 9.3$  roughly 65% of MEA species are in

the protonated form. This percent of MEH would increase dramatically with small adjustments in pH, such that at pH  $\sim 8.5$ , the MEH% is  $\sim 92\%$ . The studies in this chapter seek to characterize the spectral differences between MEA solutions in either neutral or protonated forms. Changes in the MEA modes as well as changes to the underlying water structure will be examined. MEA and HCl are mixed and allowed to react for  $\sim 5$  hours before data are acquired. No change in the surface tension is observed (within error) after 5 hours, such that it is assumed the solutions are at equilibrium with the surface after that time.

### Experimental MEH Surfaces

As shown in Figure 27, changing the pH of the MEA solution from 12.5 (green) to 9.3 (gold) results in subtle changes in the stretching region (b) and more obvious changes in the bending region (a). The stretching region shows demonstrably the same relative intensities between the CH stretches and the coordinated OH region as was observed in the native pH MEA spectra in green. The bending region, however, shows the same general spectral shape with an overall increase in spectral intensity. Table 3 details the peak frequencies extracted from the spectral fits shown in Figure 27.

If the lowered pH causes protonation of MEA resulting in  $\text{NH}_3^+$  to be present at the surface, spectral changes due to loss of the  $\text{NH}_2$  modes as well as reorientation of the MEA molecule to better solvate the charged  $\text{NH}_3^+$  are expected. In the stretching region, the SS- $\text{NH}_2$  and AS- $\text{NH}_2$  modes at  $3287\text{ cm}^{-1}$  and  $3345\text{ cm}^{-1}$  in the MEA spectra, respectively, are no longer present upon acidification. Instead, a large coordinated water region from  $\sim 3800\text{--}3000\text{ cm}^{-1}$  is observed and can be fit solely with the water and the MEA hydroxyl OH modes. This loss of the amine

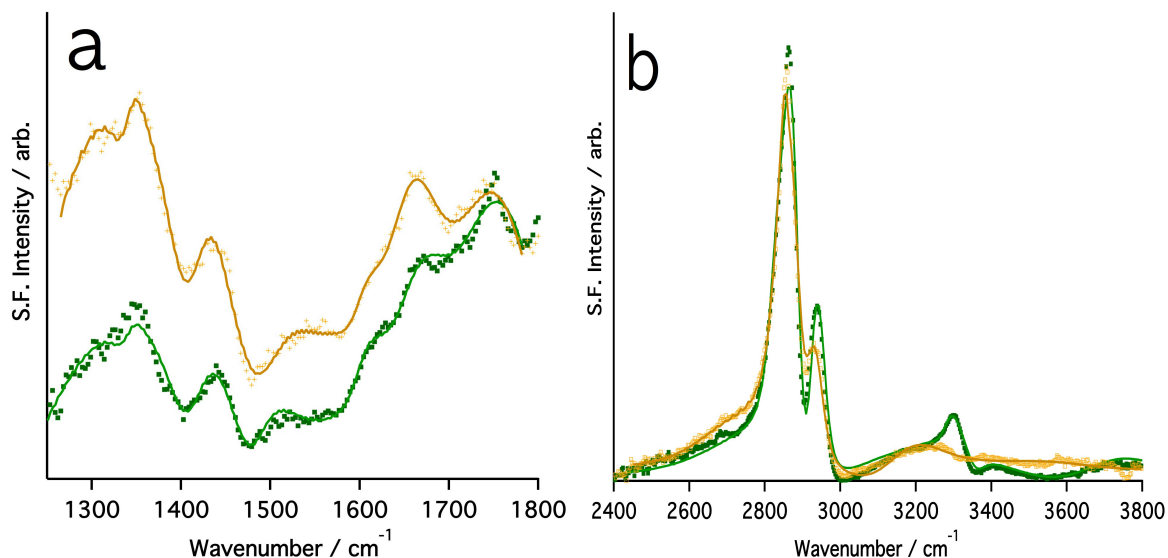


FIGURE 27. VSF spectra in *ssp*-polarization of 10 M MEA in water (green) and 10 M MEA in HCl (gold) in the bending (a) and stretching (b) regions. Experimental data (shapes) and corresponding fits (solid lines) are shown.

NH<sub>2</sub> stretching modes in the acidified MEA spectra could arise from three plausible scenarios.

One, given that at the examined pH of  $\sim 9.3$  the majority of species ( $\sim 65\%$ ) are MEH, MEH could be the only species present at the interface. Two, MEA and MEH are both present at the surface and the loss of NH<sub>2</sub> signal arises from reorientation of the MEA due to the presence of neighboring, charged NH<sub>3</sub><sup>+</sup>. Three, MEH could be absent from the surface, favoring bulk solvation of its charged group. The spectral changes in this scenario arise from surface MEA and water reorienting due to the presence of charged H<sub>3</sub>O<sup>+</sup>, sub-surface NH<sub>3</sub><sup>+</sup>, or electric field effects. In scenarios one and two, the presence of characteristic NH<sub>3</sub><sup>+</sup> modes are expected; in scenario three, changes in the coordinated water region are expected. The first scenario would result in dramatic changes to all spectral regions, unless the MEH adopts a remarkably similar surface orientation as neutral MEA, which is unlikely; the second and third

scenarios could result in only subtle changes to the MEA spectra as a result of slight reorientation.

In the stretching region, literature reports characteristic  $\text{NH}_3^+$  modes at  $\sim 3380$  and  $\sim 3280$ .<sup>120</sup> Unfortunately these frequencies reside in the coordinated water structure making direct observation difficult. As a result, these modes are not required to achieve a reasonable fit for Figure 27b. Thus, the presence of the MEH species cannot be ascribed to spectral differences between the  $\text{NH}_2$  and  $\text{NH}_3^+$  stretching modes alone. In the bending region FTIR studies report characteristic  $\text{NH}_3^+$  modes at  $1518\text{ cm}^{-1}$  and  $1634\text{ cm}^{-1}$  due to the sym. and asym. scissor of  $\text{NH}_3^+$ , respectively.<sup>119</sup> In the VSF spectra of Figure 27a, red shifting of the mode assigned to the free-OH bend of water is observed, changing from  $1641\text{ cm}^{-1}$  in MEA to  $1633\text{ cm}^{-1}$  in the acidified MEA solution. This red shift could arise from the presence of the asym. scissor of  $\text{NH}_3^+$ . Nevertheless this mode, like in the OH stretching region, is buried in the water structure making direct observation difficult. The mode at  $1601\text{ cm}^{-1}$  due to the  $\text{NH}_2$  bend, however, is present in the bending region spectra of acidified MEA. This indicates neutral MEA is still present at the surface even at pH 9.3. Taken together, the spectra of the N-H stretching and bending regions indicate unreacted MEA is present at the surface (due to the retention of the  $\text{NH}_2$  bending mode), eliminating scenario one. However these data cannot clearly determine whether other spectral changes arise from reorientation of the unreacted MEA or the presence of MEH (scenarios two and three).

The methylene stretching region could provide further insight. While C-H stretches are largely considered isolated from background water coherence, changes in molecular orientation arising from protonation or increased solvation of neighboring groups could manifest in changes in the methylene modes. In

TABLE 3. Frequencies and assignments of peaks from experimental *ssp* VSF spectra for MEA and acidified MEA.

MEA Frequencies ( $\text{cm}^{-1} \pm 10 \text{ cm}^{-1}$ )	MEH Frequencies ( $\text{cm}^{-1} \pm 10 \text{ cm}^{-1}$ )	Assignment (mode)
1340	1340	CH <sub>2</sub> wag (+ NH <sub>2</sub> , CH <sub>2</sub> rock)
1412	1412	CH <sub>2</sub> wag (+ OH def.)
1480	1480	br. water libration
1478	1485	CH <sub>2</sub> scissor/bend
1601	1601	NH <sub>2</sub> scissor/bend
1641	1633	water free-OH bend
1760	1760	coord. water bend
2846	2860	SS-CH <sub>2</sub>
2875	2890	SS-CH <sub>2</sub>
2910	2920	AS-CH <sub>2</sub>
2936	2930	AS-CH <sub>2</sub>
3200	3153	OH stretch
3287	—	SS-NH <sub>2</sub>
3345	—	AS-NH <sub>2</sub>
3340	—	coord. water stretch
3460	—	coord. water stretch
—	3650	br. coord. water stretch
3699	—	free OH



fact, the SS-CH<sub>2</sub> modes of small organic amines are known to blue shift and change in intensity upon acidification.<sup>31,145</sup> This blue shift was observed in VSF spectra of ethylenediamine, with a  $\sim 11$  cm<sup>-1</sup> shift,<sup>31</sup> and was ascribed to reorientation of the organic due to increased solvation of NH<sub>3</sub><sup>+</sup>, leading the methylene backbone to reside more parallel to the interfacial plane.

Figure 28 shows the C-H stretching region of MEA (green) and acidified MEA (gold) expanded from Figure 27b. As indicated by the red arrow in Figure 28, blue shifts are observed for the SS-CH<sub>2</sub>. But, as outlined in Table 3, these peak frequencies are within error of each other and are barely noticeable visually, appearing as a slight increase around 2900 cm<sup>-1</sup> in the spectrum of Figure 28. Moreover, in the ethylenediamine study, the blue shifts in the C-H region due to

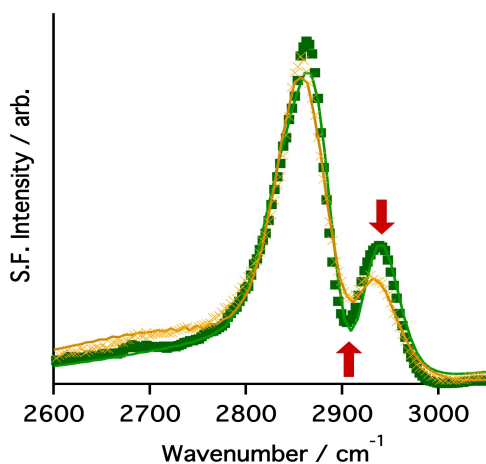


FIGURE 28. VSF spectra of 10 M MEA in water (green) and 10 M MEA in HCl (gold) in *ssp*-polarization in the CH stretching region. The red arrows indicate the spectral changes observed upon acidification.

NH<sub>3</sub><sup>+</sup> resulted in spectral C-H peaks becoming markedly more distinct; this is not observed for the acidified MEA spectra in Figure 28. Rather, a slight decrease in intensity and broadening in the AS-CH<sub>2</sub> modes is observed, but otherwise the methylene stretches are unaffected by acidification of the bulk. This lack of evidence of characteristic NH<sub>3</sub><sup>+</sup> spectral signatures, either from the N-H or C-H stretches and bends, suggests the spectra of MEA at pH  $\sim 9.3$  is largely dominated by neutral MEA. The changes in spectra with decreased pH are likely due to changes in orientation or

solvation of neutral MEA, but it is unclear if these changes manifest from MEH at the surface, other species, or field effects.

In order to ascertain the dynamics associated with the spectral changes observed, surface pressure of acidified MEA solutions was measured. The surface pressure of acidified 10 M MEA was found to be higher ( $18.9 \pm 1.6$  mN/m) than the 10 M aqueous MEA ( $13.4 \pm 0.7$  mN/m). This change in surface pressure indicates increased disorder of the water structure or increased organic species adsorption occurs upon acidification. However, the VSF spectra of Figure 27 show that the water structure isn't more disordered. Rather, in both the OH stretching and bending regions the VSF intensity increases. Increases in organic species adsorption are unlikely, but not impossible. Energetically, charged species are stabilized by increased solvation and are more likely to retreat from the surface than adsorb. Two possibilities arise from these surface pressure results if organic species adsorption is considered.

One, MEH retreats to the bulk freeing space at the surface for neutral MEA. Two, MEH is present at a depth in the surface region probed by surface tension, but not close enough to or oriented enough in the top surface to contribute to the VSF signal. The first scenario is unlikely. If MEH were migrating to the bulk and causing unreacted MEA to adsorb to the surface, the loss of the  $\text{NH}_2$  mode in the VSF spectra of Figure 27 cannot be readily explained. This is especially true when considering, as was detailed in the last chapter, that aqueous MEA does not reorient at the surface upon increased bulk concentration within these concentrations. The second scenario is possible. As was discussed in the surface population analysis of Chapter V, definitions of the surface region vary depending on technique, with VSF being more sensitive and discrete in its surface designation than surface pressure. Take, for instance, the addition of HCl to an aqueous system.

HCl is known to increase the surface pressure of water,<sup>146</sup> and was long considered a “structure-breaker” of surface water’s H-bonding network. Yet, VSF spectra of HCl show large intensity increases in the water OH stretching region, arising from more, not less, oriented water oscillators. In fact, HCl’s surface pressure raising was found to largely arise from the influence of sub-surface  $\text{Cl}^-$  while the surface-residing  $\text{H}_3\text{O}^+$  were found to increase the surface water H-bonding network, causing the increase in VSF intensity.<sup>139</sup> Thus, seemingly opposite trends may arise in reactive systems due to the interplay and ordering of charged species, and due to differences in technique. In these systems, interactions between the surface, sub-surface, and bulk can greatly influence the data extracted from different techniques, especially when different experimental probe depths are considered. Reliably matching changes in surface pressure to changes in VSF spectral intensity therefore becomes problematic. In order to ascertain a clearer picture of the surface dynamics and the changes in VSF spectra, molecular dynamics simulations of MEH are performed alongside VSF spectra calculations of MEH.

### Computed MEH Surfaces

The density profile of  $\sim 1$  M MEH (gold) is shown alongside the density profiles of  $\sim 10$  M MEA (green) and water (dotted black) in Figure 29. The  $\sim 1$  M concentration of MEH was used for ease of simulation, even though a higher molarity of MEH is expected at the experimental pH of 9.3. The MEH simulations, nevertheless, are pure systems, where 100% of amine species are MEH. The  $\sim 1$  M MEH simulations thus accurately capture the behavior of MEH at low pH. While the relative number densities of the MEH and MEA simulations cannot be directly compared to the experimental system, their generalized behavior may. Additionally, computational

studies of 10 M and 5 M MEA show no large difference in surface behavior or orientation between these two concentrations. This lack of change indicates that in this high concentration regime a generalized surface behavior may be evoked regardless of bulk concentration.

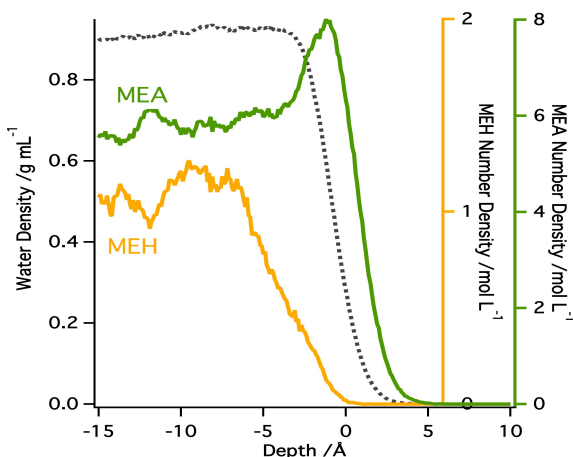


FIGURE 29. Density profile of water (grey dashed line) and  $\sim 1$  M MEH (gold solid line) extracted after 50 ns of simulation time. The  $\sim 10$  M MEA (green solid line) from Figure 22 is shown for reference.

In the density profile of Figure 29, the MEH is shown to prefer the bulk over the surface, with the majority of density residing  $>8$  Å away from the topmost surface. While MEA shows an enhancement of population at the surface, MEH is mostly absent. These density profiles would suggest that MEH would likely reside in the bulk but could also be present in the more coordinated surface region where it could influence surface MEA. This picture would explain

why the major features of the VSF spectra in Figure 27 are assigned to MEA, as well as why the surface pressure of MEA increases upon acidification.

The final component to understanding how acidification influences the MEA surface is to compare the spectra arising from experimental acidified MEA surfaces versus the spectra from computed MEH. As shown in Figure 30, the computed 1 M MEH spectrum (purple) in the bending (a) and stretching (b) regions is a poor match to the experimental *ssp* spectra of the acidified MEA surface (gold). In the calculated *ssp* MEH spectrum, the dominant spectral features at  $1485\text{ cm}^{-1}$  and  $3129\text{ cm}^{-1}$  arise from the methylene bend and the  $\text{SS-NH}_3^+$ , respectively. In the bending region, the

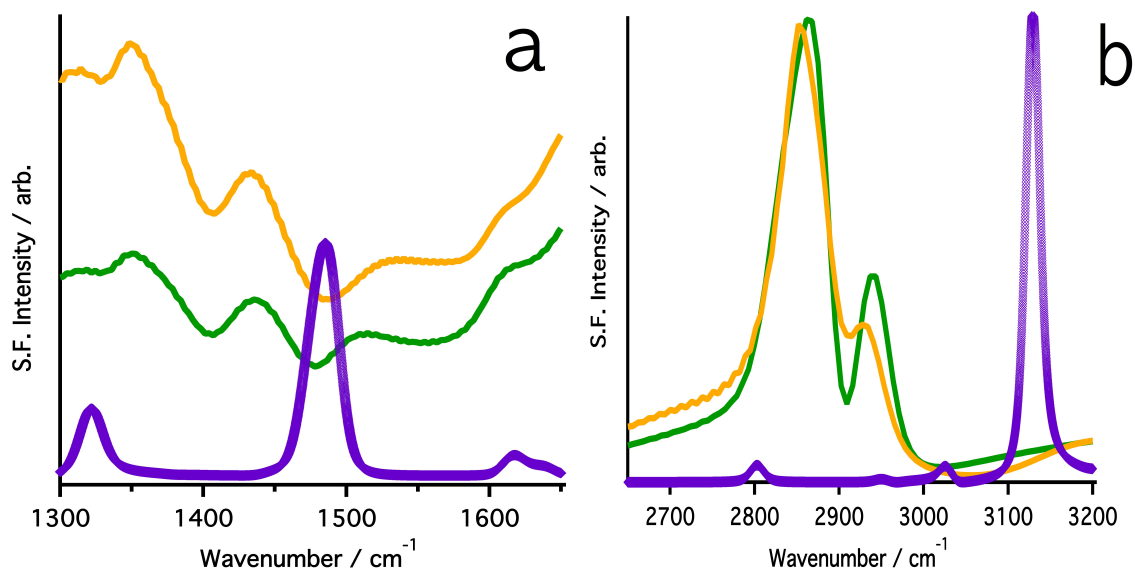


FIGURE 30. VSF spectra of MEH in *ssp*-polarization taken experimentally (gold) and calculated (purple) in (a) the bending region and (b) the CH stretching region. The green trace is experimental VSF of 10 M MEA. Note, the y-axes for (a) and (b) are not comparable, but are arbitrarily scaled so that calculated spectra may be observed.

methylene mode in the computed MEH spectra appears at  $1485\text{ cm}^{-1}$ , matching the experimental position of this mode in the acidified MEA spectrum. However, the other coordinated motions of the methylene backbone observed experimentally are not present in the computed MEH spectra. Rather, almost no intensity arises from the methylene stretches ( $3000\text{--}2800\text{ cm}^{-1}$ ) in the computed MEH spectrum, in contrast to the experiment. This lack of C–H intensity arises from a difference in orientation between MEA and MEH, as shown in Figure 31.

Orientational analysis, similar to that described in Chapter V for MEA, was conducted for MEH at the surface and in the bulk. MEH’s methylene backbone is shown to tilt to  $\sim 80^\circ$  relative to the surface normal, resulting in MEH lying more parallel to the surface. This parallel orientation would greatly reduce the C–H intensity in *ssp*-polarization, which is evidenced in the computed MEH spectra

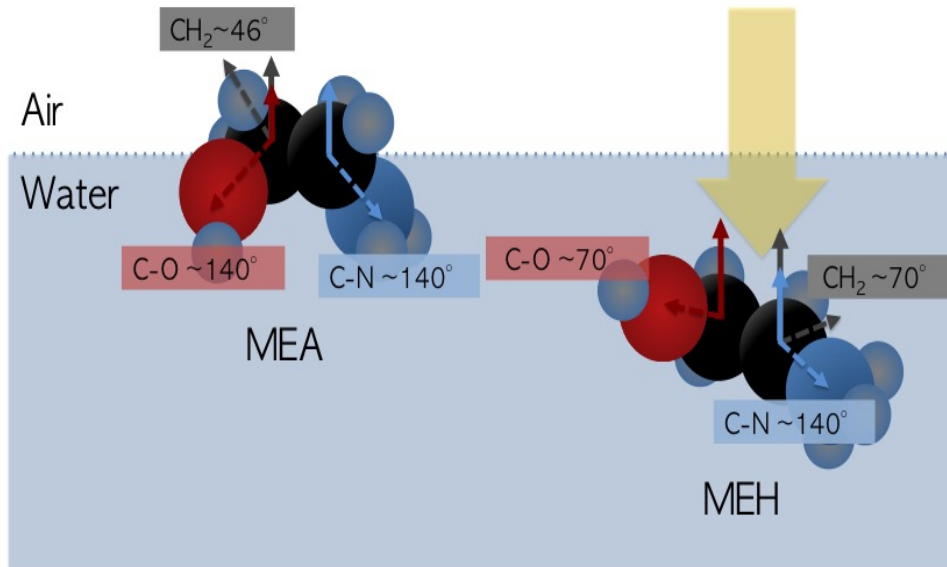


FIGURE 31. Generalized picture of MEA and MEH surface orientation and conformation. Representative angles for  $\sim 10$  M MEA and  $\sim 1$  M MEH. Note: MEH's C–O and C–N angles may reverse at the depth shown.

of Figure 30. At the top surface, the angle of MEH's C–O bond relative to surface normal greatly decreases. This decrease in C–O angle accommodates further solvation of MEH's  $\text{NH}_3^+$ , and leads to the OH pointing toward the vapor phase. This conformation of MEH would give rise to strong OH intensity that is not observed experimentally. However, at depths just a few Å into the surface, the C–O and C–N bond angles of MEH have an equal likelihood of adopting the opposite orientation, with the C–O at  $\sim 140^\circ$  and the C–N  $\sim 70^\circ$ . This lack of preferred orientation of the functional groups at depths  $>5$  Å away from the surface is unsurprising given the adopted planarity of MEH. The parallel orientation of MEH's backbone along the surface plane enables solvation of the functional groups at a larger range of C–O and C–N bond angles. Additionally, this lack of preferred orientation deeper into the surface would greatly broaden the spectral response from the OH and  $\text{NH}_3^+$  modes, enabling their resonances to be hidden in the underlying water structure.

This difference in orientation between MEA and MEH, along with the differences in spectra between experimental and computed MEH suggest the surface of the acidified MEA solutions at pH~9.3 is still largely neutral MEA. The surface pressure increase and the subtle VSF spectral changes likely arise from MEH residing deeper into the surface and slightly reorienting surface MEA and water.

## Conclusions

The equilibrium between MEA and its protonated form, MEH, exists in aqueous solutions but also greatly impacts CO<sub>2</sub> uptake. In order to understand changes occurring from reaction with the acidic gas versus changes that arise from surface acidification alone, the pH study of this chapter was conducted. The results of these studies show the spectral changes observed upon acidification of the surface are minor and subtle. These minor spectral changes suggest that the presence of MEH minimally affects the overall surface composition and behavior, even though the bulk %MEH is ~65%.

The experimental results of this chapter indicate the underlying water structure is perturbed upon acidification, resulting in increased intensity in the OH stretching and bending regions. Additionally, the acidification of MEA causes the surface pressure to increase, likely due to the presence of MEH deeper into the surface. The computational results show MEH resides deeper into the surface and favors bulk solvation. This difference in depth between MEA and MEH indicates layering of the two species could occur in the real system, with MEA residing in the top surface and MEH further down. VSF spectra would therefore mostly capture surface MEA features, while surface tension could capture the presence of both. The

mismatch between the computed MEH spectrum and the experimental acidified spectra supports this idea.

This chapter provides a needed assessment of the MEA surface behavior upon acidification. The results of this chapter ultimately show that the surface is predominantly neutral MEA even if the bulk concentration is largely protonated MEA. The subsequent chapters will build on this picture of MEA acidification, examining surface changes due to reactivity with acidic  $\text{CO}_2$  and  $\text{SO}_2$ . This ability to probe the surface as bulk dynamics evolve will guide our interpretations in the subsequent chapters.



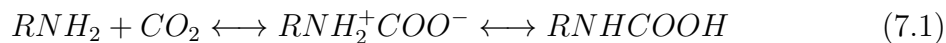
## CHAPTER VII

### SURFACE BEHAVIOR OF MEA-CO<sub>2</sub>

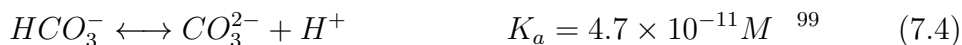
Chapters V and VI detailed the unique surface properties of MEA, laying the groundwork for the gaseous uptake studies of the current and following chapter. The experiments herein detail the behavior of the MEA surface during and after reaction with CO<sub>2</sub>. The chapter will begin by detailing the spectral response in the bending and stretching region, and discussing spectral changes due to carbamate formation. Deuterated MEA and a surface-active carbamate are used to aid in the assignments of the spectral modes. Computational studies began by Dr. Nicholas Valley will detail the VSF spectral contributions from product species. The chapter will conclude by detailing the behavior of MEA-CO<sub>2</sub> reacting surfaces. I designed and conducted all experiments, interpreted all data, and wrote all aspects of the manuscript. This work will be published in a forthcoming paper.

#### Introduction

The reaction of CO<sub>2</sub> gas with aqueous amine solutions follows different reaction mechanisms depending on the surrounding functionalities near the amine moiety.<sup>147</sup> Primary amines, such as MEA, are widely used in industry due to their fast reactivity with CO<sub>2</sub> to form stable carbamates via a zwitterionic intermediate similar to Equation (7.1).<sup>107,148-150</sup>



As these CO<sub>2</sub> uptake reactions occur in aqueous media, the aqueous-phase equilibria of these reacting species must be considered.

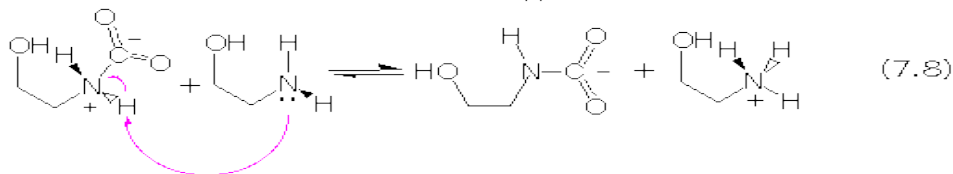
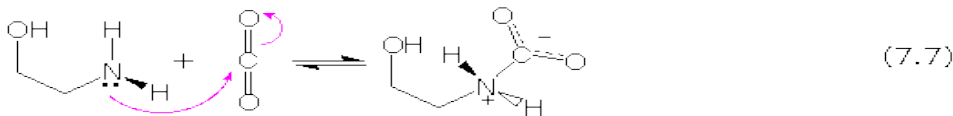


Under most industrial conditions, these side reactions are thought to contribute negligibly to the overall reaction, but there has been mounting evidence that side reactions will occur at some concentrations, temperatures, and pressures.<sup>105,147</sup> For MEA much uncertainty still exists regarding the dominant mechanism of CO<sub>2</sub> uptake. Whether CO<sub>2</sub> reacts initially with MEA according to Equation (7.1),<sup>150–152</sup> or whether water facilitates CO<sub>2</sub> uptake forming bicarbonate and carbonate ions that then react with MEA<sup>40,112,153</sup> is a subject of continued study.

Recent C<sup>13</sup> NMR analysis examined the reaction intermediates of CO<sub>2</sub> uptake into MEA. The analysis showed that the mechanism of carbamate formation from MEA changes depending on the amount of CO<sub>2</sub> in solution.<sup>112</sup> CO<sub>2</sub> absorption was found to be mediated by reaction with MEA at low CO<sub>2</sub> loadings, but hydration of CO<sub>2</sub> and the formation of bicarbonate and carbonate dominate at high CO<sub>2</sub> loadings. Regardless of mechanism, water plays a vital role in the chemistry occurring during CO<sub>2</sub> uptake to MEA, as shown by the side reactions of Equations (7.2)–(7.6). Water is known to stabilize the MEA<sup>+</sup>COO<sup>-</sup> zwitterion, catalyze proton transfer to form more stable products, and play a critical role in CO<sub>2</sub> desorption.<sup>40,105,107</sup>

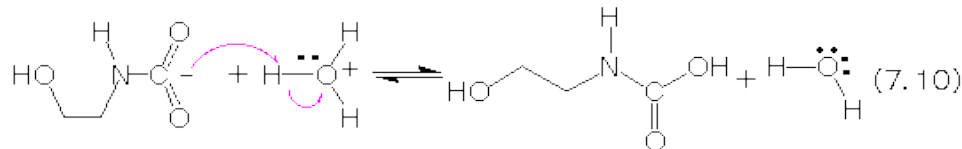
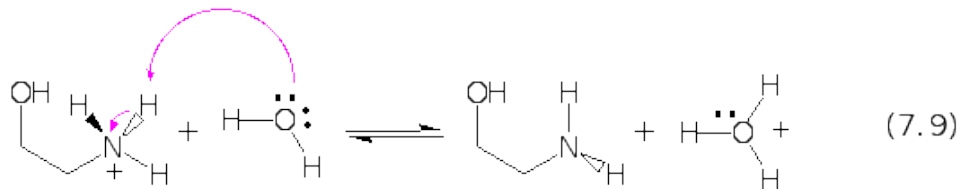
Even more uncertain is the role of the interface in hindering or enhancing CO<sub>2</sub> uptake, or in determining the various aqueous reactions that occur. The interface is a water-poor region compared to the bulk, suggesting that the bulk chemistry detailed above may evolve differently at the surface. Soft-X-ray photoelectron spectroscopy measurements of aqueous MEA and CO<sub>2</sub>-treated aqueous MEA solutions have, in fact, shown direct MEA-CO<sub>2</sub> chemistry (Equation (7.1)) could be facilitated in the interface.<sup>14,154</sup> The proposed mechanism for CO<sub>2</sub> uptake in those studies involved surface adsorption and reaction leading to charged product migration away from the surface. In this scenario, the surface would remain mostly neutral, unreacted MEA.

The mechanism of bulk MEA-CO<sub>2</sub> chemistry follows the zwitterion intermediate from Equation (7.1) with immediate proton transfer according to Equations (7.7) and (7.8).<sup>40</sup>



The MEA-H<sup>+</sup> (MEH) and MEA-COO<sup>-</sup> (carbamate, CBM) are additionally in equilibria with water, according to Equations (7.9) and (7.10), with associated pK<sub>a</sub> of 9.55 for MEA-H<sup>+</sup> and pK<sub>b</sub> of 5.8 for MEA-COO<sup>-</sup>.<sup>14</sup>

The studies of the previous chapters have detailed the surface behavior of MEA and how it changes upon acidification. MEA inhabits the surface region in concentrations mirroring the bulk, where it occupies a large interfacial footprint, and orients such that its methylene backbone is pointing out of the surface. Upon acidification (Equation 7.9), the MEA surface is largely unperturbed. Protonated



MEA is suspected to exist in the sub surface region where it affects water and MEA orientation, but has minimal influence on the VSF spectra. The uptake of gaseous  $\text{CO}_2$  to aqueous surfaces (Equations 7.2–7.4) was equally shown to have little bearing on the structure of the surface water, as discussed in Chapter IV. Instead, evidence for bicarbonate and carbonate formation was seen through small changes in modes arising from water participating in strong hydrogen bonding.

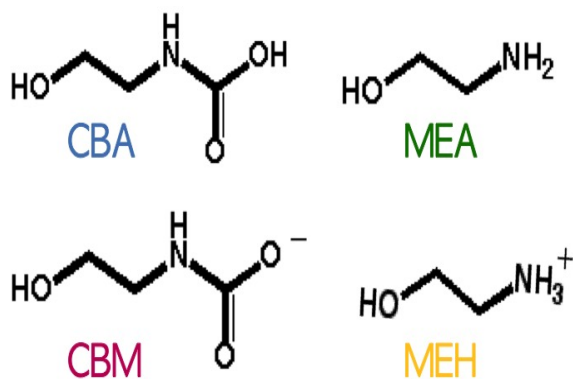


FIGURE 32. Structures of molecules examined in this chapter. CBA = carbamic acid; MEA = monoethanolamine; CBM = carbamate; and MEH = protonated MEA

The experiments in this chapter seek to understand how MEA and  $\text{CO}_2$  react at the surface, how the reaction evolves, how charged species affect the interface, and how species migration impacts further gas uptake. As with the other chapters in this dissertation, the combination of VSF spectra, surface tension, and computational methodology will allow for assembling the picture of this

highly complex chemistry. The surface presence and behavior of the four main species involved in MEA- $\text{CO}_2$  reactions will be examined: MEA, protonated MEA (MEA-

H<sup>+</sup> or MEH), carbamate (MEA-COO<sup>-</sup> or CBM), and carbamic acid (MEA-COOH or CBA), as shown in Figure 32.

The CO<sub>2</sub>-MEA reaction is found to have long time dynamics, with surface pressure stabilizing after 12 hours. The surface spectra, however, show immediate change that is invariant for the remainder of the reaction. CO<sub>2</sub> is allowed to react with the MEA surface for ~15 hours at a flow rate of 0.6 liters per minute. Spectra at short and long CO<sub>2</sub> exposure, as well as after the reaction has ceased will be discussed and compared to computed spectra for pure solutions of the products in Figure 32.

### Surface Dynamics During CO<sub>2</sub> Uptake to MEA

The surface pressure of a solution provides information on interfacial population, changes in water's hydrogen bonding network, and time dynamics of species migration to or from the surface. During CO<sub>2</sub> uptake to MEA, a number of products are formed, as shown in Equations (7.1)–(7.8). Depending on their charge and functional group, some product species have unique preference to the surface versus the bulk solution. The surface pressure of 10 M MEA during reaction with CO<sub>2</sub> was therefore monitored as a function of time, as shown in Figure 33.

Recall that the surface pressure of 10 M MEA, as outlined in Chapter V, is  $13.4 \pm 0.7$  mN/m. MEA reaches this surface pressure within the first few minutes of surface formation. This surface pressure value corresponds to a surface mole fraction roughly equal to the surface mole fraction of bulk solution, as discussed in Chapter V, indicating the surface concentration of MEA tracks with the bulk solution concentration. When CO<sub>2</sub>(g) is introduced above the MEA surface, the surface pressure of the solution rises over a period ~12 hours before reaching an equilibrium value of  $28.2 \pm 1.6$  mN/m, as shown in red in Figure 33.

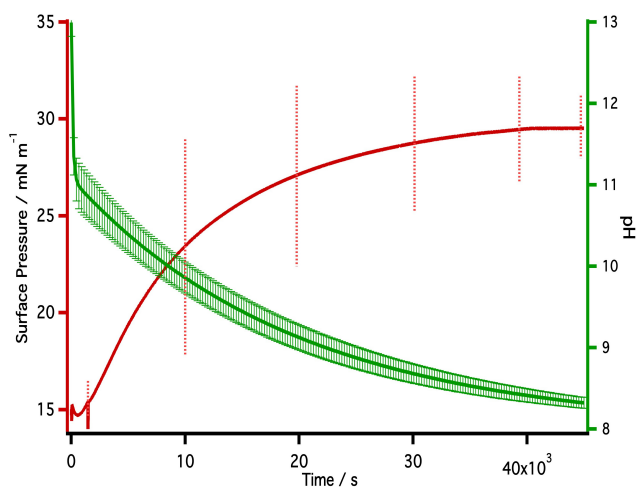


FIGURE 33. Surface pressure of 10 M MEA vs. time under  $\text{CO}_2$  exposure (red) alongside the change in solution pH during reaction (green). Vertical lines are errors bars at  $\pm 1\sigma$  from the average.

pH $\sim 8.5$  (green). Acidification of the MEA surface was shown in Chapter VI to cause the surface pressure to increase to  $18.9 \pm 1.5$  mN/m at pH 9.3. However, the MEA- $\text{CO}_2$  system shows an even higher surface pressure than the acidified solution at pH 9.3. In the acidified MEA study, the charged MEH was shown to be present in the coordinated surface layer, largely removed from the top surface. The increase in surface pressure in that study was indicative of charged MEH and neutral MEA present at the surface, and causing a rise in the surface pressure.

A similar layering is anticipated in the MEA- $\text{CO}_2$  system given the surface pressure data of Figure 33. When  $\text{CO}_2$  reacts with MEA, protonated MEA along with other product species such as carbamate (CBM) and carbamic acid (CBA) are formed. These products are likely to disrupt the hydrogen bonding network as a result of their needed solvation. This perturbation would result in an increase in the solution surface pressure if the products remain within the surface region.

This increase in the surface pressure is traditionally characteristic of an increased population of ions or organics adsorbing to the surface and disrupting the water H-bonding network. However, this simple trend likely does not capture the complexity of the number of chemical species reacting and forming in this system.

During reaction, the pH of the solution decreases from pH $\sim 12.5$  to

However, surface pressure studies during gaseous uptake are rare.<sup>155,156</sup> The inherent adsorption/desorption equilibria of gaseous uptake cause perturbations to the surface which can lead to false surface pressure values or result in large variance like that shown in Figure 33. More often, surface pressures are acquired before and after reaction, not during. In the MEA-CO<sub>2</sub> studies, the systems are reacted for at least 12 hours before CO<sub>2</sub> flow ceases. The solutions are then equilibrated for anywhere from 30 minutes to a few days before a post-CO<sub>2</sub> surface pressure is measured. This post-CO<sub>2</sub> MEA surface has a surface pressure of  $25.7 \pm 1.2$  mN/m, within error of the equilibrated system during CO<sub>2</sub> flow. This agreement between the equilibrated CO<sub>2</sub> data and the post-CO<sub>2</sub> data suggests the methodology employed for measuring surface pressure accurately captures the surface dynamics.

Yet, Melaaen and coworkers examined reacted MEA-CO<sub>2</sub> (“post-CO<sub>2</sub>”) solutions and found a decrease in surface pressure with increasing CO<sub>2</sub> loading.<sup>40,110,111</sup> This is the opposite trend observed in Figure 33. The Melaaen studies examined surface pressure using the bubble method of pendant drop. They consistently measured decreases in surface pressure, indicative of species migrating away from the surface or increased ordering of the water network. The Wilhelmy plate method was used in the surface pressure studies shown in Figure 33, and is more likely than the Melaaen methodology to experience fluctuations in surface pressure due to off-gassing of CO<sub>2</sub>. However, preliminary corroborating studies employing the same methodology as Melaaen have shown a similar trend to those data in Figure 33 acquired via the Wilhelmy plate method.

Ultimately, the surface pressure methodology used in this thesis best matches the experimental system during VSF studies. While the surface and bulk dynamics may not be accurately probed via surface pressure due to difficulties in experimental

technique, system–gas exchange, and reactivity, VSF spectral analysis can provide accurate assessment of changes in the surface during gas uptake.<sup>20,101,140</sup>

### MEA–CO<sub>2</sub> Spectral Response

The change in VSF intensity of a 10 M MEA surface upon reaction with gaseous CO<sub>2</sub> is shown for the stretching region in *ssp*–polarization in Figure 34. In the bottom trace of Figure 34, characteristic modes due to the methylenes and amine of MEA (green) appear at  $\sim 3287\text{ cm}^{-1}$ ,  $\sim 2936\text{ cm}^{-1}$ , and  $\sim 2875\text{ cm}^{-1}$ . The neat air/water interface (grey) is shown for reference. When CO<sub>2</sub> is introduced above the MEA surface at a rate of 0.6 liters per minute, as shown by the second trace (pink), the intensity of the CH<sub>2</sub> and NH<sub>2</sub> modes of MEA decreases. Additionally, the water region at frequencies  $>3400\text{ cm}^{-1}$  increases in intensity. After the CO<sub>2</sub>–MEA reaction progresses for  $\sim 13$ – $15$  hours (red), the CH<sub>2</sub> stretches and the coordinated water region further decrease in intensity, as shown in the third trace of Figure 34. When reaction with CO<sub>2</sub> ceases, the reaction cell is purged of CO<sub>2</sub> for a minimum of 30 minutes to allow the reacted solution to equilibrate. The top trace shows the post–CO<sub>2</sub> spectra (blue). The post–CO<sub>2</sub> spectra shows a return of the intensity in the CH<sub>2</sub> stretching region, but a sustained loss of the NH<sub>2</sub> modes. The peak positions arising from the fits to these spectra are listed in Table 4.

The VSF spectra of the 10 M MEA surface during and after CO<sub>2</sub> flow reveal that the surface is perturbed during CO<sub>2</sub> uptake. If CO<sub>2</sub> is reacting with surface MEA, characteristic modes from MEA’s amine would disappear due to formation of a secondary amide. Additionally, changes to MEA’s methylene modes due to reorientation or new product formation, as well as changes in the water structure due to presence of charged species, are likely to occur. The amine NH<sub>2</sub> stretching



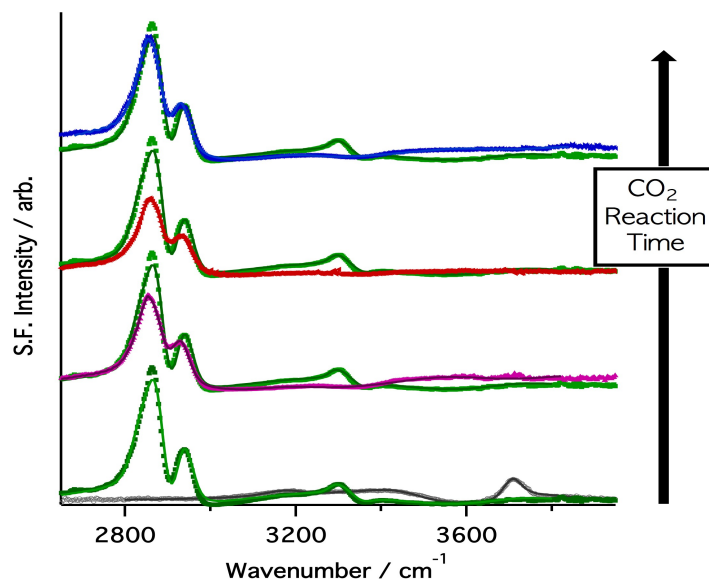


FIGURE 34. VSF spectra in *ssp*-polarization of 10 M MEA (bottom, green) during reaction with CO<sub>2</sub> (2nd, pink, ~3 hours; 3rd, red, ~15 hours), and after CO<sub>2</sub> (top, blue) has been purged and the reaction ceased. The neat water surface (grey) is shown in the bottom spectra for reference. Experimental data (shapes) and corresponding fits (solid lines) are shown. The spectra are offset for clarity.

modes of MEA, as shown in Figure 34 and Table 4, are indeed absent during and after CO<sub>2</sub> flow. This loss of the NH<sub>2</sub> feature is likely due to MEA reaction with CO<sub>2</sub>, but could also arise from reorientation of the surface species. Additionally, the methylene stretching modes decrease in intensity and broaden during CO<sub>2</sub> uptake. Broadening of the methylene modes occurs when charged species are present at the surface and cause reorientation of surface organics, water, or themselves. As was detailed in the previous chapter, loss of the amine modes as well as broadening and blue shifting of the methylene modes occurs with decreasing pH. This drop in pH, according to Equation (7.5), forms MEH in solution which resides in the strongly coordinated surface water region, affecting the MEA spectral response. However, the loss of methylene mode intensity during CO<sub>2</sub> uptake is not seen during the acidification studies of the previous chapter. These differences in spectral behavior could arise from differences in surface

TABLE 4. Frequencies and assignments of peaks from experimental *ssp* VSF spectra. Experimental frequencies are from global fits of spectra taken at incident angles 45° (visible) and 60° (IR). All frequencies are  $\text{cm}^{-1} \pm 10 \text{ cm}^{-1}$ .

10 M MEA	10 M MEA + CO <sub>2</sub> (3 hr)	10 M MEA + CO <sub>2</sub> (15 hr)	10 M MEA post-CO <sub>2</sub>	Assignment (mode)
1340	1345	1345	1345	CH <sub>2</sub> wag (+ NH <sub>2</sub> , CH <sub>2</sub> rock)
1412	1413	1413	1413	CH <sub>2</sub> wag (+ OH def.)
1478	1489	1489	1489	CH <sub>2</sub> scissor/bend
—	1563	1563	1563	Amide II
1601	—	—	—	NH <sub>2</sub> scissor/bend
2846	2855	2855	2855	SS-CH <sub>2</sub>
2875	2870	2870	2870	SS-CH <sub>2</sub>
2910	2910	2910	2910	AS-CH <sub>2</sub>
2936	2923	2923	2923	AS-CH <sub>2</sub> (or FR-CH <sub>2</sub> )
3200	3153	3153	3153	OH stretch
3287	—	—	—	SS-NH <sub>2</sub>
3345	—	—	—	AS-NH <sub>2</sub>
—	3650	3650	3650	OH stretch (broad)

structure due to the different acidities (pH 9.3 vs 8.5) of the two studies, from the presence of other products residing in the surface including CBA, CBM, bicarbonate or carbonate ions, or from differences in reaction dynamics and species migration. Regardless, the stretching region spectra alone do not capture the complete picture of the MEA surface upon reaction with CO<sub>2</sub>.

In the bending region, however, the spectral changes to the 10 M MEA surface upon CO<sub>2</sub> exposure show increases in MEA modes and the appearance of a new feature. As shown in Figure 35, characteristic MEA modes (green) appear, arising from the NH<sub>2</sub> bend ( $\sim 1601 \text{ cm}^{-1}$ ) and methylene bending motions ( $\sim 1478 \text{ cm}^{-1}$ ,  $\sim 1412 \text{ cm}^{-1}$ , and  $\sim 1340 \text{ cm}^{-1}$ ). The neat air/water interface (grey) is shown in the bottom trace for reference. When CO<sub>2</sub> is introduced above the MEA surface, as shown by the second trace (pink), MEA’s amine NH<sub>2</sub> bend at  $\sim 1601 \text{ cm}^{-1}$  disappears. This matches the loss of the amine modes in the stretching region, and indicates the NH<sub>2</sub>

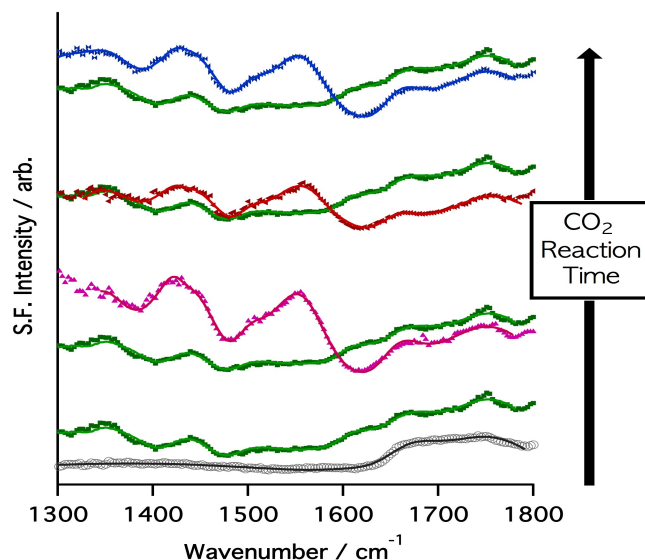


FIGURE 35. VSF spectra in *ssp*-polarization of 10 M MEA (bottom, green) during reaction with CO<sub>2</sub> (2nd, pink, ~3 hours; 3rd, red, ~15 hours), and after CO<sub>2</sub> (top, blue) has been purged and the reaction ceased. The neat water surface (grey) is shown in the bottom spectra for reference. Experimental data (shapes) and corresponding fits (solid lines) are shown. The spectra are offset for clarity.

oscillator is disordered or no longer at the surface. Furthermore, MEA's methylene bending modes increase in intensity and broaden upon CO<sub>2</sub> exposure. This increase in the CH<sub>2</sub> bending response contrasts the decrease in intensity of these modes in the stretching region. Yet similar to the stretching region, this change in CH<sub>2</sub> bending intensity is not seen upon acidification. Rather, at low pH the bending region only changes in intensity of the background water modes. These spectral changes would suggest unique surface behavior arises during CO<sub>2</sub> flow separate from changes solely due to decreased pH.

The most obvious change to the bending region spectrum upon CO<sub>2</sub> exposure is the presence of a new feature at ~1563 cm<sup>-1</sup>. This feature is present during the initial stages of the reaction (pink trace), but remains throughout even after the CO<sub>2</sub> is evacuated and the reaction has ceased (blue trace). If CO<sub>2</sub> were reacting with MEA

to form CBA or CBM at the surface, not only would the loss of MEA's amine modes be expected, but the presence of new modes due to the secondary amide (Equation 7.8) is likely. Amides have characteristic C=O and COO<sup>-</sup> stretches, secondary N-H deformations, and coordinated C-N stretches that form a suite of resonances called the amide bands. The C=O stretch appears from 1700–1660 cm<sup>-1</sup> in secondary amides,<sup>120</sup> and is known as the amide I band. The amide I has been observed in VSF spectra previously,<sup>53,157,158</sup> but is strongly overlapped with the water bending mode at ~1641 cm<sup>-1</sup>. FTIR studies of CO<sub>2</sub>-MEA systems show new modes appear during CO<sub>2</sub> exposure at ~1568 cm<sup>-1</sup> and ~1468 cm<sup>-1</sup>.<sup>119</sup> These new spectral features were assigned to the AS-COO<sup>-</sup> and SS-COO<sup>-</sup>, respectively, based on previous FTIR carbamate studies. Additionally, the secondary amide II band, arising from the N-H deformation, appears from 1570–1510 cm<sup>-1</sup>,<sup>120</sup> while the amide III, arising primarily from the C-N stretch, appears from 1400–1200 cm<sup>-1</sup>.<sup>157</sup>

The resonant mode fits in the bending region for 10 M MEA and 10 M MEA after CO<sub>2</sub> exposure are shown in Figure 36 and listed in Table 4. The post-CO<sub>2</sub> fits in the top trace of Figure 36 show the new mode at 1563 cm<sup>-1</sup> as well as the absence of the NH<sub>2</sub> feature at 1601 cm<sup>-1</sup>. According to the literature values, the mode at 1563 cm<sup>-1</sup> could arise from the AS-COO<sup>-</sup> or the amide II band. As the only new mode in the post-CO<sub>2</sub> data, the assignment of the 1563 cm<sup>-1</sup> feature will largely indicate the character of the product species at the surface. If the amide II, either carbamic acid (CBA) or carbamate (CBM) could be present and contributing to VSF intensity; if the AS-COO<sup>-</sup>, only CBM. (See Figure 32.) In order to accurately assign this feature, spectra of deuterated MEA and tert-butyl N-(2-hydroxyethyl)carbamate (“BOC”) were acquired.

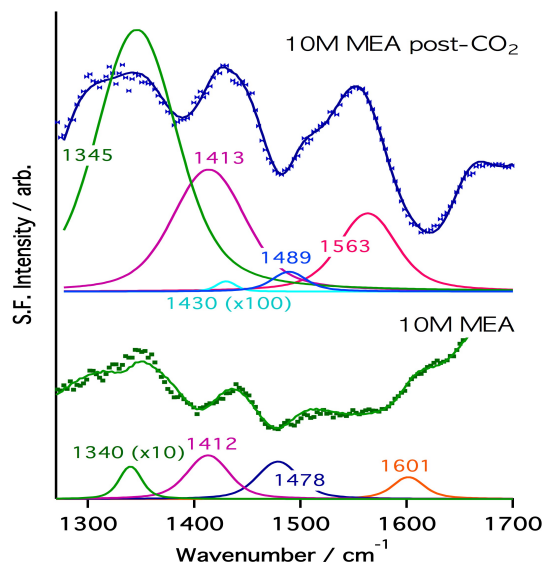


FIGURE 36. VSF spectra in the bending region in *ssp*-polarization of 10 M MEA (green, bottom) and 10 M MEA after reaction with CO<sub>2</sub> (blue, top). Experimental data (shapes) and corresponding fits (solid lines) are shown with individual component fits. The component fits arising from the water modes have been removed for clarity.

### Assignment of 1563 cm<sup>-1</sup> Feature

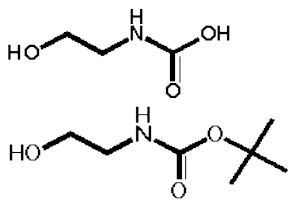


FIGURE 37. CBA (top) and BOC (bottom)

As shown in Figure 37, tert-butyl N-(2-hydroxyethyl)carbamate, or BOC, is structurally similar to the MEA carbamic acid CBA. BOC has an amide II resonance from its secondary N-H, but no carboxylate COO<sup>-</sup> due to

the presence of the tert-butyl group. Acquiring VSF spectra of BOC in the bending region will elucidate

whether the peak at 1563 cm<sup>-1</sup> arises from CBM or CBA. Figure 38 shows VSF spectra of 5 M BOC in the bending region, with 10 M MEA (green) and 10 M MEA post-CO<sub>2</sub> reaction (blue). The 5 M BOC spectrum shows characteristic features from the amide I (1675 cm<sup>-1</sup>), methyl bend and wags (1357 cm<sup>-1</sup>, 1271 cm<sup>-1</sup>), and methylene bends (1489 cm<sup>-1</sup> and 1413 cm<sup>-1</sup>).<sup>159</sup>

Additionally, the feature at  $1563\text{ cm}^{-1}$  appears in the BOC spectrum, overlaying with the same feature on the post- $\text{CO}_2$  MEA spectrum. The presence of the  $1563\text{ cm}^{-1}$  mode in the BOC spectrum strongly indicates this feature arises from the amide II mode, and points to CBA's surface presence. However, as a secondary check for this assignment, a deuteration study was also conducted.

Spectra of 10 M MEA in  $\text{H}_2\text{O}$  (dark blue) and in  $\text{D}_2\text{O}$  (teal) after  $\text{CO}_2$  exposure is shown in Figure 39.  $\text{D}_2\text{O}$  rapidly exchanges its protons with MEA's amine, causing a spectral red shift of  $\sim 1000\text{ cm}^{-1}$  in the stretching region.<sup>160</sup> In the bending region, these shifts are greatly lessened,<sup>98</sup> as was

discussed in Chapter IV. DFT calculations of deuterated MEA predict the  $\text{ND}_2$  bend to shift  $\sim 190\text{ cm}^{-1}$ , while the secondary ND deformation is expected to shift only  $\sim 10\text{--}30\text{ cm}^{-1}$ . In Figure 39, the post- $\text{CO}_2$  flow spectra show a red shift of  $\sim 20\text{ cm}^{-1}$  for the peak at  $1563\text{ cm}^{-1}$  when the amide NH becomes deuterated. If the feature at  $1563\text{ cm}^{-1}$  arose from the carboxylate  $\text{COO}^-$  stretch, this red shift isn't expected to occur.

Given the spectral evidence from the BOC and deuteration studies, we can confidently assign the feature at  $1563\text{ cm}^{-1}$  to the amide II mode. The presence of the amide II in the VSF spectra indicates CBA is present at the surface early during  $\text{CO}_2$  uptake, and remains there even after MEA- $\text{CO}_2$  reaction has ceased. During  $\text{CO}_2$  uptake, the pH of the aqueous MEA solution changes from  $\sim 12.5$  to

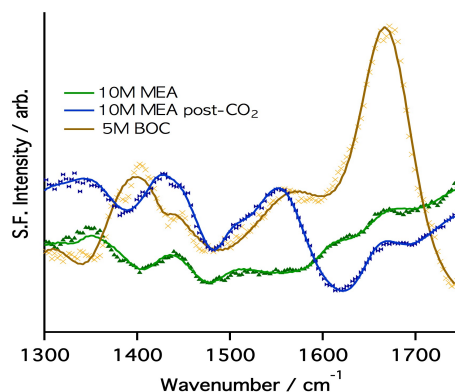


FIGURE 38. VSF spectra in *ssp*-polarization of 5 M BOC (yellow). The 10 M MEA (green) and 10 M MEA post- $\text{CO}_2$  (blue) spectra are shown for reference.

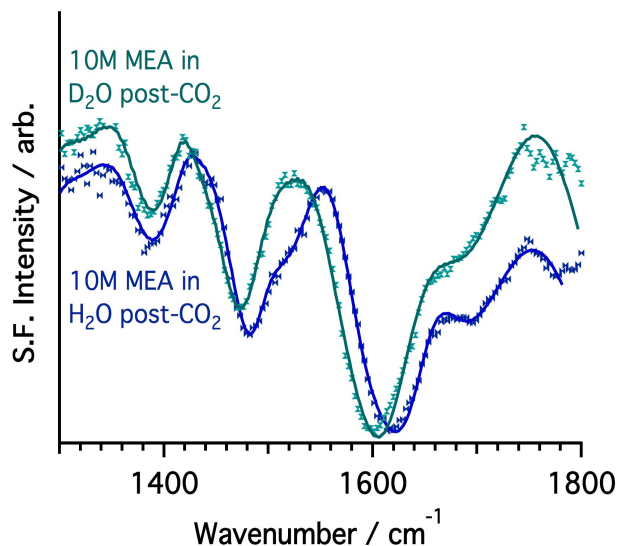


FIGURE 39. VSF spectra in the bending region in *ssp*-polarization of 10 M MEA after reaction with CO<sub>2</sub> in H<sub>2</sub>O (dark blue) and D<sub>2</sub>O (teal). Experimental data (shapes) and corresponding fits (solid lines) are shown.

~8.5. This pH value is just above the  $pK_a$  for CBA/CBM equilibria,<sup>14</sup> implying a little more than half of the MEA-CO<sub>2</sub> reaction product is neutral carbamic acid. At pH ~8.5, the MEA is largely in its protonated form, MEH, although the equilibria of MEA/MEH discussed in Chapter VI shifts due to other product equilibria. The VSF spectra indicate CBA resides and is ordered at the surface given the presence of the amide II mode and the loss of the amine NH<sub>2</sub>. What is not known is whether the surface is predominantly CBA or a mix of CBA and unreacted MEA. This surface ordering of unreacted MEA with a product was found to occur upon acidifying the MEA, as was detailed in the previous chapter. The surface pressure data indicate, like in the acidification studies, that more products are migrating to the surface or that the water network is strongly perturbed during CO<sub>2</sub> uptake. But due to the uncertainty of surface pressure data for reactive solutions, a different methodology for ascertaining the solution dynamics needs to be undertaken. Thus, a computational

study of pure  $\sim 1$  M CBA was conducted by Dr. Nicholas Valley in order to better understand the observed spectral changes.

### Computed Carbamic Acid (CBA)

The density profile of  $\sim 1$  M CBA solution (16 molecules) extracted from the molecular dynamics simulations is shown in blue in Figure 40 along with the profile for  $\sim 10$  M MEA in green for reference. In pure solutions, CBA is shown to be present at the surface, even in the topmost surface region (depths  $< 3$  Å).

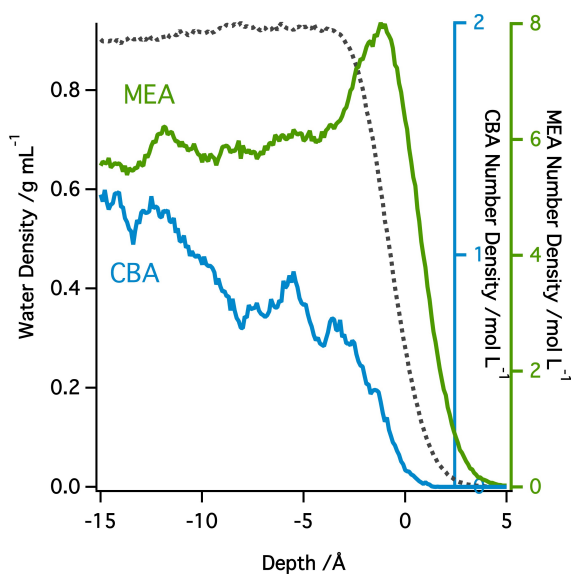


FIGURE 40. Density profile of water (grey dashed line) and  $\sim 1$  M CBA (blue) extracted after 54 ns of simulation time. The  $\sim 10$  M MEA (green) density from Figure 22 is shown for reference.

Compared to MEA, however, CBA does not show enhancement in the surface region but rather a gradual loss of density. This is likely due to the carboxylic acid moiety making the CBA considerably more polar and therefore causing it to partition more toward polar solvation environments. Nevertheless, the density profile of Figure 40 indicates CBA may reside in the surface, confirming the VSF spectral assignments that indicate its presence there.

The experimental spectral changes that occur upon MEA reaction with  $\text{CO}_2$  include 1) broadening of the  $\text{CH}_2$  bending and stretching modes; 2) decrease in the  $\text{CH}_2$  stretching intensity but increase in the  $\text{CH}_2$  bending intensity; 3) loss of  $\text{NH}_2$



bending and stretching modes; and 4) appearance of an amide II mode at  $1563\text{ cm}^{-1}$ . The presence of the amide II along with the loss of the  $\text{NH}_2$  modes is indicative of surface-adsorbed CBA. However, the remarkable similarity in the CH stretching region between 10 M MEA spectra and post- $\text{CO}_2$  spectra suggests unreacted MEA may still be present at the surface. The  $\text{CH}_2$  stretching modes in the post- $\text{CO}_2$  data show only slight broadening compared to those same modes in the aqueous MEA data. Additionally, the molecular tilt of the  $\text{CH}_2$  relative to the surface normal of the post- $\text{CO}_2$  system was found to be the same (within error) as the neat 10 M MEA system. (The details of the calculation of molecular tilt are found in Chapters II and V.)

A few scenarios could explain these changes. One, the surface is mostly CBA, which adopts a surface orientation very similar to neutral MEA, with its methylene backbone pointing into the vapor and its functional groups solvated in the water. Two, the surface is a mix of unreacted MEA and CBA. The spectral contributions in the  $\text{CH}_2$  region would therefore arise from the ordered MEA's methylene backbone which orients toward the vapor, while the CBA orients such that its NH gives rise to VSF signal. Examining the calculated *ssp* VSF signal from pure CBA (blue, middle) in light of the experimental post- $\text{CO}_2$  data (dark blue, top), shown in Figure 41, clarifies which scenario is most likely.

The computed  $\sim 1$  M CBA VSF signal in Figure 41 shows marginal  $\text{CH}_2$  signal in both the bending (a) and stretching (b) regions. Compared to the computed  $\sim 10$  M MEA signal (green), the CBA spectra does not fully capture the spectral components in the experimental post- $\text{CO}_2$  data. CBA does display a peak at  $1525\text{ cm}^{-1}$  from the amide II band, in line with our experimental observations and assignment. Yet, the experimental post- $\text{CO}_2$  spectra largely matches the computed  $\sim 10$  M MEA spectra

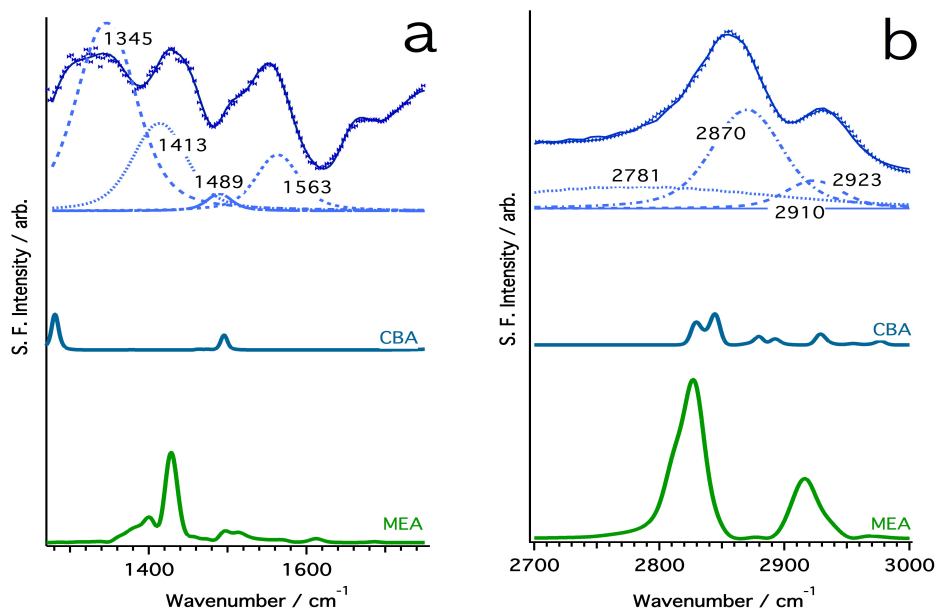


FIGURE 41. Computed VSF spectra of CBA in *ssp*-polarization (middle traces, blue) in the (a) bending region and (b) CH stretching region. The dark blue trace at top is the experimental VSF spectra of post- $\text{CO}_2$  exposure MEA solution, with component fits shown in light blue. The green, bottom trace is the computed  $\sim 10$  M MEA spectra for reference. The spectra have been off-set for clarity, and the y-axes for (a) and (b) are not comparable.

in both peak position and relative intensity of contributing modes. This spectral behavior of computed CBA can be understood in terms of CBA's surface orientation, as detailed in Figure 42.

In the surface, CBA is oriented along the interfacial plane. At the top surface, the functional groups are solvated such that their bond angles point slightly toward the bulk water. At a few angstroms into the surface, the pointing of the functional groups changes such that CBA's C-O and C-N bonds point toward the vapor phase. Based on the density profile of Figure 40, it is within this deeper surface region that CBA is most likely to reside. Additionally, within this region the methylene backbone of CBA is as likely to point up as down. This lack of preferred orientation

would result in  $\text{CH}_2$  oscillators adopting a range of environments, causing a reduction or cancellation in the VSF signal of the methylene modes.

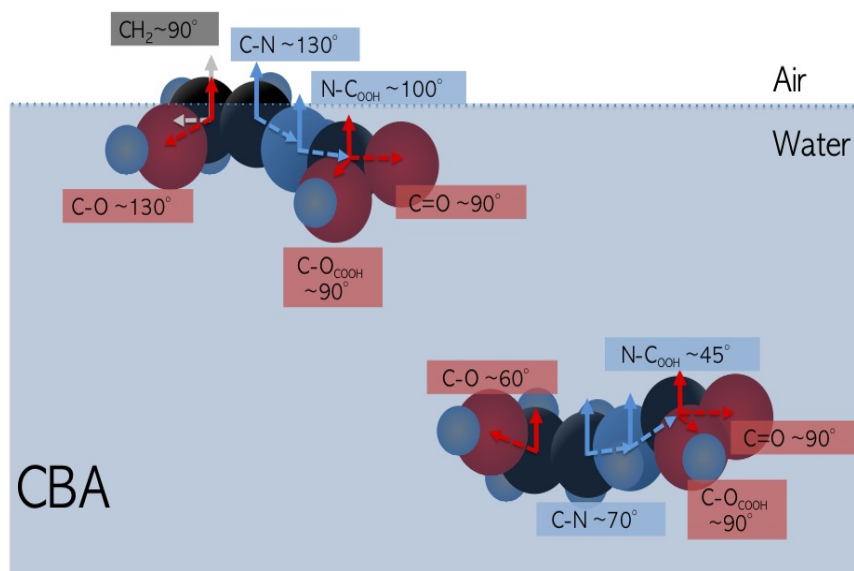


FIGURE 42. Generalized picture of  $\sim 1$  M CBA surface orientation in the top surface (left) and in the more coordinated surface (right).

Given CBA's density profile and VSF spectrum that matches the experimental spectrum in part, it is likely that CBA is present at the surface but oriented within the more coordinated surface layer. Its presence in the deeper surface results in broadening of the  $\text{CH}_2$  modes, as shown by the multiple contributions to the methylene spectra in Figure 41. Yet the surface largely remains neutral MEA. This neutral MEA surface persists even after the reaction has ceased in the bulk. Moreover, this MEA–CBA surface displays preference for CBA formation over other reaction products. The surface preference for CBA could speak to different reaction routes in the surface versus the bulk, as has been shown for  $\text{CO}_2$  uptake to amine–functionalized ionic liquids.<sup>15,161,162</sup> The reaction equilibria that result in CBA formation involve 1:1 molar uptake of  $\text{CO}_2$  : MEA (Equation 7.1). Whereas the reaction equilibria that produce the charged CBM and MEH involve 1:2 molar uptake (Equations 7.7 & 7.8).

Thus, a surface preference for the reaction leading to higher uptake capacity speaks to an untapped channel towards better overall CCS uptake efficiencies.

## Conclusions

The experiments in this chapter show that the MEA surface is clearly impacted as a result of CO<sub>2</sub> uptake. Surprisingly, this impact is mitigated by the continued surface presence of unreacted MEA. The surface behavior of MEA–CO<sub>2</sub> chemistry is complex, and results in changing surface and bulk dynamics, ion presence, solvation effects, and interfacial ordering. A simple depiction of the progression of the MEA–CO<sub>2</sub> reaction is shown in Figure 43 to aide in understanding how the surface evolves during this chemistry.

Initially, as described in Chapter V, MEA is present at the surface and oriented such that its methylene backbone is pointing toward the vapor phase. MEA, even at 10 M, has a large interfacial footprint and is primarily isolated from other MEA molecules. Upon introduction of CO<sub>2</sub> reactions at the surface and the bulk occur between MEA, CO<sub>2</sub>, and water, according to Equations (7.1)–(7.8). Initial reactions at the surface between MEA and CO<sub>2</sub> would result in CBA formation, while those in the bulk could additionally lead to charged product formation. As the CO<sub>2</sub> uptake progresses, reactions with water and charged species result in many ions and ion pairs in solution. Charged products are not present or ordered at the surface but instead are likely to retreat into the bulk,<sup>14</sup> while CBA and unreacted MEA are likely to migrate to the surface raising the surface pressure. After CO<sub>2</sub>–MEA reaction ceases, and the CO<sub>2</sub> atmosphere is purged, the surface is largely unchanged from its structure during initial stages of reaction except CBA now resides in the coordinated surface region.

Computational studies of mixed CBA and MEA systems are currently underway to better understand changes in surface structure and spectra when these two species are interacting. Nevertheless, the reaction of MEA and CO<sub>2</sub> at the interface is shown to proceed via CBA formation. The surface preference of CBA indicates a unique route toward more efficient carbon capture, given the higher uptake capacity via the CBA equilibrium. Additionally, the surface presence of CBA speaks to added challenges in removing CO<sub>2</sub> during the desorption step in CCS. Carbamic acid is a much more stable product than the zwitterion or carbamate, requiring more energy for CO<sub>2</sub> removal. Understanding the fundamental behavior governing the surface during reactions with gas phase species has been shown in these experiments to be essential for understanding the chemistry dictating this vital system. Furthermore, understanding the fundamental chemistry during CO<sub>2</sub>-amine reactions could aid in the future design of novel CO<sub>2</sub> sorbents to maximize the favorability of these surface phenomena.

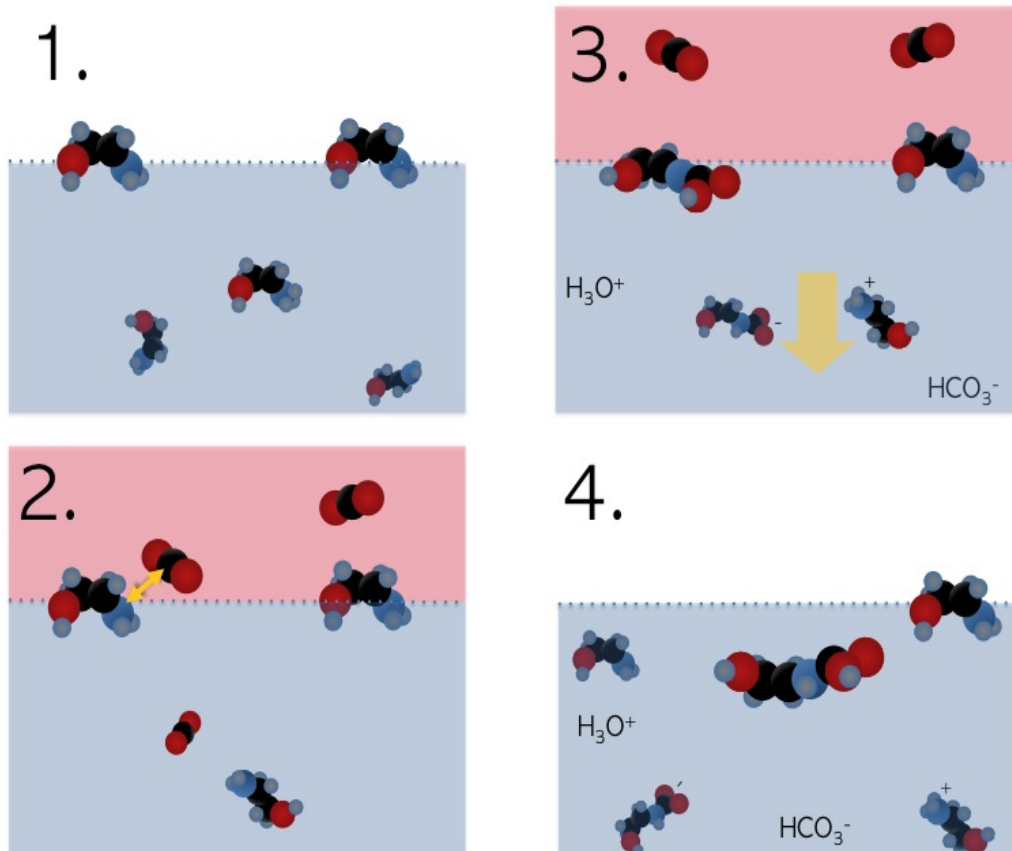


FIGURE 43. Depiction of the evolution of aqueous MEA surfaces in the presence of CO<sub>2</sub>. 1. MEA at the vapor/water interface. 2. Exposure to CO<sub>2</sub> results in CO<sub>2</sub> reacting with water and MEA to form CBM, MEH, and CBA. 3. The charged species (CBM and MEH) retreat from the surface while CBA remains. 4. After CO<sub>2</sub> flow ceases, the CBA remains at (or migrates to) the surface.

## CHAPTER VIII

### PRELIMINARY STUDIES: SURFACE BEHAVIOR OF MEA-SO<sub>2</sub>

The previous chapters have detailed the behavior of MEA at the vapor/water interface both isolated and in the presence of acids and ions. Isolated MEA was shown to be surface active and oriented at the vapor/water interface such that its methylene backbone points into the vapor phase. When perturbed either by acidic gas or acidified solution, the surface remains largely unaffected. This chapter examines the pervasiveness of this MEA surface behavior by examining uptake of another acidic gas, SO<sub>2</sub>. The studies in this chapter are preliminary, and are included to further describe this observed trend in MEA surface behavior. The chapter begins by detailing the spectral response of MEA surfaces under an SO<sub>2</sub> atmosphere. A brief discussion comparing the behavior of MEA surfaces during CO<sub>2</sub> and SO<sub>2</sub> uptake follows. This work will be published in a forthcoming communication.

#### **Introduction**

While aqueous monoethanolamine solutions are largely considered a benchmark in CO<sub>2</sub> capture, their reaction with other acidic gas is a subject equally worthy of examination. Flue gas lines, while predominately N<sub>2</sub> and CO<sub>2</sub>, often contain mixes of other acidic gases, including SO<sub>2</sub>, NO<sub>x</sub>, and H<sub>2</sub>S.<sup>2</sup> SO<sub>2</sub> is the main acidic impurity in scrubbing technologies, where it can quench reactions intended to scrub CO<sub>2</sub>. Depending on the sulfur content of the coal used, a typical coal-fired power plant will have flue streams composed of ~12% CO<sub>2</sub> and ~300 ppm SO<sub>2</sub>.<sup>163</sup> Yet in the US, EPA air quality standards mandate less than 75 ppb of SO<sub>2</sub> may be emitted from

stationary sources per hour.<sup>164</sup> Thus SO<sub>2</sub> scrubbing, especially at coal-fired power plants, is an industrial necessity in its own right.

In CO<sub>2</sub> capture systems, SO<sub>2</sub> contamination results in quenching MEA reactivity, either through direct reaction with MEA or through acidifying the solution. Increases in SO<sub>2</sub> concentration result in increases in the average energy consumed during the capture process and decreases in the CO<sub>2</sub> removal efficiency.<sup>163,165</sup> Moreover, the presence of SO<sub>2</sub> shifts the chemistry in flue lines, resulting in ammonia generation during subsequent scrubbing cycles.<sup>1</sup>

As a result, desulfurization is often proposed as a precursor to CO<sub>2</sub> removal in CCS technologies.<sup>165,166</sup> Power plants have employed desulfurization systems for decades, and are able to reduce SO<sub>2</sub> concentrations in flue lines by 50–98% depending on method employed.<sup>163</sup> In current power plants, desulfurization predominately occurs via SO<sub>2</sub> reaction with dry or wet limestone (CaCO<sub>3</sub>). However the operating conditions of these processes often have large variations, and are limited by the amount of SO<sub>2</sub> they can scrub (~75 ppm). This maximum scrubbing ability is much poorer than the current CCS requirements for SO<sub>2</sub> concentrations demand (~5 ppm).<sup>163,167</sup> As a consequence of MEA–SO<sub>2</sub> reaction favorability, MEA has also been proposed as a potential secondary scrubber in the desulfurization steps of CCS.<sup>163</sup>

Yet, the underlying chemistry of amine–SO<sub>2</sub> reactions is poorly understood. Sulfonic and sulfamic acids have been proposed as possible reaction products, as shown in Figure 44, but no experimental evidence for their formation has been found.<sup>168</sup> Rather, SO<sub>2</sub> reactions with water are thought to dictate the chemistry during these amine scrubbing processes, generating ammonium sulfite salts, according



to Equation (8.1).<sup>163,165,169</sup>



SO<sub>2</sub> is highly water soluble, quickly forming HSO<sub>3</sub><sup>-</sup> in aqueous solution, as was discussed in Chapter IV. Moreover SO<sub>2</sub> and its subsequent aqueous ions, HSO<sub>3</sub><sup>-</sup> and SO<sub>3</sub><sup>2-</sup>, have a very large impact on aqueous surfaces. SO<sub>2</sub> is known to form surface complexes with water at vapor/liquid surfaces, and is shown to greatly impact the structure of the coordinated water region as a result of

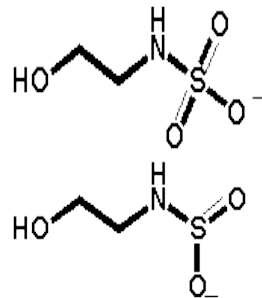


FIGURE 44. Possible SO<sub>2</sub>—MEA products<sup>1</sup>

aqueous ion solvation.<sup>19,101,170</sup> SO<sub>2</sub> has also been shown to impact organic-coated water surfaces, either through interaction with water in the presence of non-reactive organics<sup>140</sup> or through interaction with both the reactant and product species of reactive organics.<sup>20</sup> SO<sub>2</sub> is also known to rapidly exchange with carbonate at the vapor/water surface, leading to potential desulfurization methods.<sup>167</sup>

Therefore, understanding the surface behavior of MEA during SO<sub>2</sub> absorption and reactivity is not only important for understanding quenching during CO<sub>2</sub> capture, but also in desulfurization processes. Additionally, the reactions between MEA and SO<sub>2</sub> have important atmospheric relevance. Sulfates are the oxidation products of SO<sub>2</sub>, and are among the most abundant components to atmospheric aerosols.<sup>171</sup> Whereas amines are expected to significantly increase their atmospheric presence due to their use in CCS, as was mentioned in Chapter I. Thus, the reactions between MEA and SO<sub>2</sub>, sulfites, and sulfates pose important questions for future atmospheric

chemistry concerns, especially at aqueous aerosol surfaces where these species are likely to reside.

The experiments in this chapter explore the surface behavior of MEA during SO<sub>2</sub> uptake. Both the bending and stretching regions during and after SO<sub>2</sub> reaction will be examined, and spectral changes will be compared to the same system during CO<sub>2</sub> uptake. These studies will add further insight into the behavior of the MEA system under acidic conditions.

### MEA–SO<sub>2</sub> Spectra

VSF spectra of 10 M MEA during and after SO<sub>2</sub> gas flow were acquired in *ssp*-polarization, as shown in Figure 45. The bottom trace in Figure 45 shows the 10 M MEA surface (green) with the neat air/water interface (grey) in both the bending (a) and stretching (b) regions. The characteristic modes of MEA, as described in Chapter V, arise from the CH<sub>2</sub> stretches (2936 cm<sup>-1</sup>, 2910 cm<sup>-1</sup>, 2875 cm<sup>-1</sup>, and 2846 cm<sup>-1</sup>) and bends (1478 cm<sup>-1</sup>, 1412 cm<sup>-1</sup>, and 1340 cm<sup>-1</sup>); the NH<sub>2</sub> stretches (3345 cm<sup>-1</sup> and 3287 cm<sup>-1</sup>) and bend (1601 cm<sup>-1</sup>); and the OH stretches and bend of water and the hydroxyl group on MEA.

The middle trace of Figure 45 shows the 10 M MEA surface during reaction with SO<sub>2</sub>. Both the bending and stretching region spectra show a loss of the NH<sub>2</sub> modes. This loss, as was discussed in Chapters VI and VII, indicates either a reorientation of surface species or a depletion of amines in the interfacial region as a result of reaction or migration. The CH<sub>2</sub> stretching region, however, shows an overall increase in the intensity of the methylene modes. This CH<sub>2</sub> intensity increase in light of the NH<sub>2</sub> intensity loss suggests reorientation or reaction, not migration, of MEA likely occurs during SO<sub>2</sub> exposure. In the bending region, an overall loss in spectral intensity is

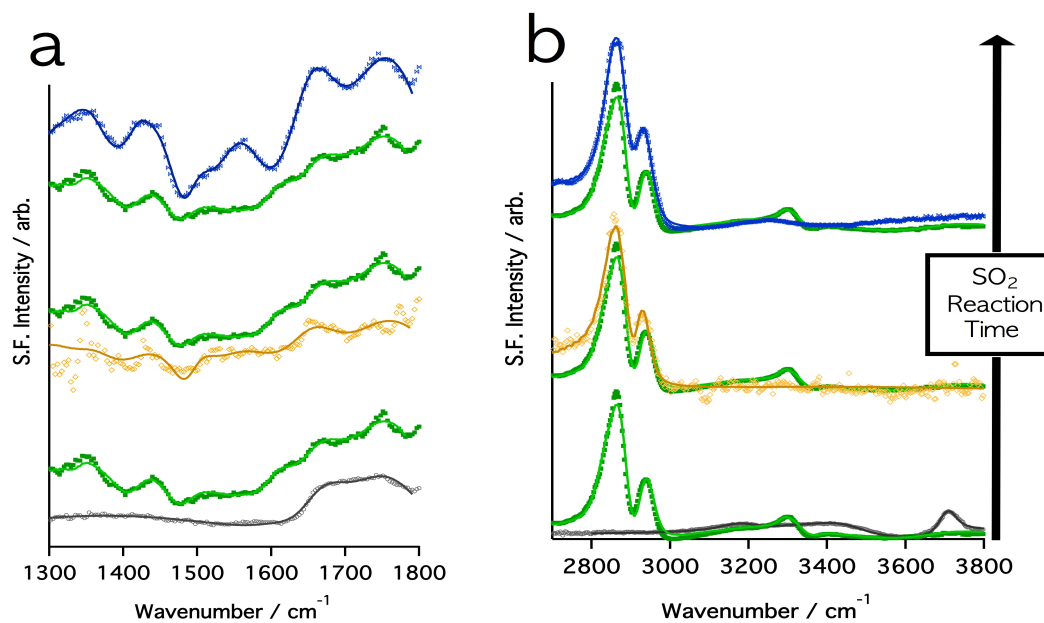


FIGURE 45. VSF spectra in the (a) bending region and (b) stretching region in *ssp*-polarization of 10 M MEA (bottom, green) during reaction with  $\text{SO}_2$  (middle, yellow), and after  $\text{SO}_2$  (top, blue) has been purged and the reaction ceased. The neat water surface (grey) is shown in the bottom spectra for reference. Experimental data (open shapes) and corresponding fits (solid lines) are shown. The spectra are offset for clarity.

observed. This intensity loss in the bending region arises from a depression of intensity from the water modes; the  $\text{CH}_2$  bending modes actually increase in intensity, in line with the changes observed in the stretching region. Taken together,  $\text{SO}_2$  exposure to water surfaces shows an overall depletion in the water modes with increases in the  $\text{CH}_2$  modes of MEA. This depression of the water structure is unique from other organic- $\text{SO}_2$  systems.<sup>20,140</sup> In those studies, the addition of  $\text{SO}_2$  resulted in an overall increase in the water structure due to bisulfite formation, electric field effects, and increased alignment of surface waters. In the MEA system, the depression of the water modes with the subsequent increase in methylene intensity suggests the surface MEA actually becomes more ordered or compact at the surface during reaction with  $\text{SO}_2$ , leading to a depression in water intensity. These differences between the MEA and previously

examined organics could arise from experimental differences in concentration and solution pH, or from inherent physical differences in the systems.

Additional changes to the MEA–SO<sub>2</sub> system occur when the SO<sub>2</sub> is turned off and the solutions are equilibrated over 8 hours, as shown in the top trace of Figure 45 (blue). In the post–SO<sub>2</sub> spectra, both the CH<sub>2</sub> modes and the water modes increase in intensity in both the bending and stretching regions. Moreover, the presence of the amide II mode at 1563 cm<sup>-1</sup> is seen in the bending region data, indicating MEA reacts with SO<sub>2</sub> or its ion to form a secondary amine (NH). The spectral changes observed between SO<sub>2</sub> flow and post–SO<sub>2</sub> flow could speak to surface interactions that might occur between water and SO<sub>2</sub> and MEA and SO<sub>2</sub>, as was observed in past studies.<sup>20</sup>

For instance, one possible reaction scenario could involve the surface adsorption of SO<sub>2</sub>. MEA is surrounded by water at the vapor/water interface as was shown in Chapter V. SO<sub>2</sub> could adsorb to the interface, interacting with surface water and reacting with MEA. The presence of surface–adsorbed SO<sub>2</sub> could reorient the surface water and MEA such that an overall depression in the water structure is observed, as shown in the middle trace of Figure 45. After the SO<sub>2</sub> is turned off, and the surface–adsorbed SO<sub>2</sub> desorbs, both the MEA and water structure return to their preferred alignment in ambient air. The post–SO<sub>2</sub> system also contains HSO<sub>3</sub><sup>-</sup> and H<sub>3</sub>O<sup>+</sup> ions which are present at the surface aligning interfacial waters and MEA. This ion–induced alignment causes an overall increase in the observed spectral response in the post–SO<sub>2</sub> system, as shown in the top trace of Figure 45. Despite the reasonableness of this scenario, other surface behavior scenarios involving ion pair migration or charge separation of sulfite species could match the spectral changes observed in Figure 45.

Further experiments would need to be conducted in order to ascertain dynamics and long term effects in these systems.

Nevertheless, the presence of the amide II in the post-SO<sub>2</sub> data suggests formation of a sulfamic acid species at the surface, further indicative of possible unique reaction behavior at the surface versus the bulk. Interestingly, the post-SO<sub>2</sub> solutions are at pH  $\sim$ 7–8. Sulfamic acid groups typically have pK<sub>a</sub>s around 1-3,<sup>172</sup> indicating sulfamic acid should be entirely deprotonated (i.e. charged) in the post-SO<sub>2</sub> solution. However, charged species rarely reside at the surface in the absence of charge screening, further indicating other dynamics and cooperative effects might be at play.

### Comparing Surface Impact of SO<sub>2</sub> and CO<sub>2</sub>

Ultimately, the chemistry occurring between SO<sub>2</sub> and MEA at the surface appears characteristically similar to that occurring during CO<sub>2</sub> uptake. After reaction is complete, the surface shows the presence of reactant species (amide II band) as well as ordered MEA (methylene modes). However, the effects to the water structure and CH<sub>2</sub> modes are different for the different gases. The spectral differences observed in post-CO<sub>2</sub> and post-SO<sub>2</sub> solutions are compared in Figure 46.

In the stretching region (b), both the post-CO<sub>2</sub> (dark blue) and post-SO<sub>2</sub> (teal) spectra show a depletion of the OH stretching modes ( $> 3000 \text{ cm}^{-1}$ ). Whereas in the bending region (a), the post-SO<sub>2</sub> spectrum shows greater increase in the water modes compared to the post-CO<sub>2</sub> spectrum. This difference in water mode intensity could arise from differences in solvation structure of HSO<sub>3</sub><sup>-</sup> and HCO<sub>3</sub><sup>-</sup>, difference in surface orientation of the two MEA reactant products, or differences in electric field effects due to difference in interfacial preference and pK<sub>a</sub> between sulfite

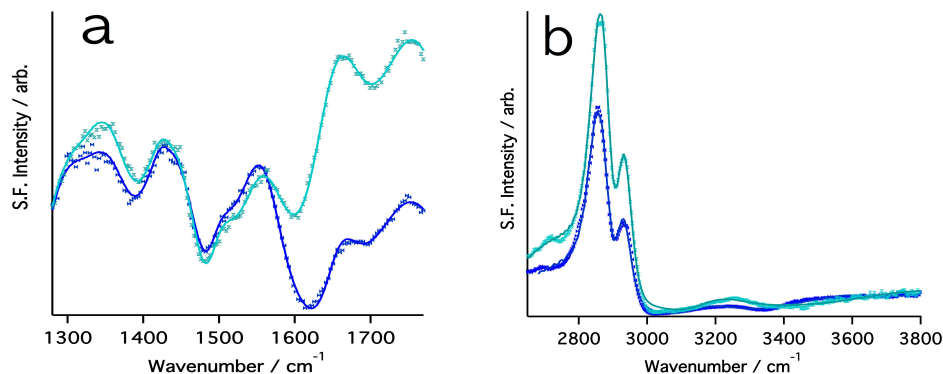


FIGURE 46. VSF spectra in the (a) bending region and (b) stretching region in *ssp*-polarization of 10 M MEA after reaction with  $\text{SO}_2$  (teal) and after reaction with  $\text{CO}_2$  (dark blue). Experimental data (open shapes) and corresponding fits (solid lines) are shown.

and bicarbonate, as was discussed in Chapter IV. The methylene modes also show differences in spectral intensity between the post- $\text{SO}_2$  and post- $\text{CO}_2$  solutions. In both the bending and stretching region, the  $\text{CH}_2$  modes are more intense in the post- $\text{SO}_2$  spectra than those in the post- $\text{CO}_2$ , although this change in intensity is marginal in the bending spectrum. This intensity difference could arise from a greater surface population of MEA (or MEA- $\text{SO}_2$  product) during  $\text{SO}_2$  uptake than in  $\text{CO}_2$  uptake, or from reorientation of surface species. Most likely, the intensity changes arising from surface water and the intensity changes arising from the organic methylene modes are cooperative, and speak to differences in surface structure inherent in these two systems. Understanding the fundamental cause of these differences is a subject for continued study.

## Conclusions

$\text{SO}_2$  chemistry with aqueous MEA has been shown to influence the surface behavior in a similar manner to the other studies of this dissertation. This surface behavior of MEA seems to be intrinsic and not depend on the acidic gas used. Similar

to the CO<sub>2</sub> studies of Chapter VII, the uptake of SO<sub>2</sub> results in product formation, depression of water structure, and the continued presence of unreacted MEA at the aqueous surface. While these trends are generally similarly across reactant gas species, spectral changes indicate differences between the SO<sub>2</sub> and CO<sub>2</sub> systems that speak to unique solvation, orientation and surface preference between the two systems. Understanding these fundamental differences could elucidate behavior that allows for selectivity or tunability in similar scrubbing systems.

## CHAPTER IX

### CONCLUSIONS

Our ability to combat the increasing amount of atmospheric CO<sub>2</sub> relies on a multitude of strategies. These strategies must address commercial and private interests, arise from government and individuals, and require both industry and consumer rethinking in order to be successful. Implementing the variety of strategies capable of addressing these various sectors will take decades of planning and shifts in cultural opinion. Yet, there are some mitigation strategies that are currently viable. One proposed immediate strategy is carbon capture and sequestration (CCS). CCS involves capturing CO<sub>2</sub> before it is emitted, then storing it for future use. Most CCS technologies are proposed to retrofit existing infrastructure, from power plants to commercial manufacturing. Since stationary sources, i.e. buildings like power plants, emit the majority of global CO<sub>2</sub>, capping their emissions will be a positive step toward CO<sub>2</sub> mitigation. However, a number of engineering and fundamental science issues prevent current implementation of CCS in some sectors.

The experiments in this dissertation address one aspect of the fundamental chemistry occurring during CO<sub>2</sub> uptake, specifically what happens at the interface between gases and liquids during carbon capture. Some CCS technologies involve capturing CO<sub>2</sub> by scrubbing with aerosolized aqueous amines. In these systems, CO<sub>2</sub> is absorbed into the liquid solution, reacts, and is trapped until a later cycle. Few studies have examined this uptake of CO<sub>2</sub> at the surface, relying instead on bulk phenomena to draw generalizations about the system chemistry. Yet as the complexity of these CO<sub>2</sub> capture systems grows, understanding the foundational



dynamics and chemistry at play as the gas crosses into the liquid could be crucial to effectively engineering better and more efficient technologies.

The experiments starting in Chapter V developed the interfacial picture of one CCS scrubber, aqueous monoethanolamine or MEA. Chapter V outlined MEA's surface behavior and dynamics. The studies presented therein showed MEA adsorbs to the aqueous surface immediately. MEA's surface concentration closely matches its bulk concentration, even at 10 M. MEA was found to orient at the surface such that its functional groups were solvated in the aqueous phase while its methylene backbone pointed out toward the vapor. This preferred orientation was enduring, even if the surface concentration changed by an order of magnitude. This orientation indicated MEA does not pack like a traditional surfactant at the interface. Rather, MEA occupies a relatively large interfacial footprint ( $\sim 126 \text{ \AA}^2/\text{molecule}$ ), suggesting it resides at the surface predominantly surrounded by water molecules. Moreover, this orientation of MEA causes the lone pair electrons on MEA's nitrogen atom to be pointing toward the vapor. This orientation would be advantageous for reaction with gaseous  $\text{CO}_2$  at the surface.

The studies of Chapter VI examined how this MEA surface changes upon acidification. The chemistry of  $\text{CO}_2$  uptake is dictated by a number of factors, with decreases in solution pH being a fundamental directing force. The studies in Chapter VI, however, showed the MEA surface remains largely neutral even as the bulk pH changed by over three orders of magnitude. This surface neutrality suggests charged amine species migrate away from the surface, and that surface behavior is largely unaffected by bulk pH. These differences in bulk and surface behavior indicate the surface chemistry could evolve uniquely from what dominates in the bulk.

The acidification studies of Chapter VI laid the foundation for the CO<sub>2</sub> uptake experiments of Chapter VII. Those experiments examined the surface behavior during CO<sub>2</sub> uptake, and sought to understand how the highly ordered MEA surface might inhibit or enhance reaction with CO<sub>2</sub>, or facilitate the migration of product species. The chemistry during CO<sub>2</sub> uptake is complex, with changing pH and formation and migration of charged and neutral product species affecting interfacial behavior. Nevertheless, the experiments presented therein showed the surface begins as MEA, and after reaction is a mix of carbamic acid and unreacted MEA. Carbamic acid (CBA) is shown to reside at the surface, while other reaction products migrate into the bulk. The favoring of carbamic acid at the surface over other product species primarily arises from the charged species being less stabilized at the surface than the bulk. Yet, the exclusive surface presence of CBA also demonstrates the uptake capacity at the surface is higher than the bulk. This exclusivity could be manipulated for more efficient CCS.

The dissertation concluded by examining the reaction of SO<sub>2</sub> with MEA, seeking to further probe the universality of the MEA surface during acidic perturbation. Although preliminary, the SO<sub>2</sub> study of Chapter VIII once more affirmed the interfacial picture of MEA. MEA exists in its neutral form at the surface, even when pH and chemical equilibria shift the concentration of other species in the bulk. This surface neutrality suggests the uptake of acidic gas isn't inhibited by interfacial species; rather, surface MEA largely remains ready for further reaction. The ability of the surface to remain neutral throughout reaction is largely a consequence of solvation effects. Probing how these dynamics change as a function of solvent, surface area, or interfacial capacity could open new avenues for more efficient uptake strategies necessary in CCS.

## APPENDIX A

### FITTING PARAMETERS FOR WATER

The fitting parameters for water used throughout this thesis, and specifically discussed in Chapter IV.

TABLE 5. Frequencies, gaussian widths, and assignments of peaks from experimental *ssp* VSF spectra at incident angles 45° (visible) and 60° (IR).

Frequencies ( $\text{cm}^{-1} \pm 10 \text{ cm}^{-1}$ )	Gaussian Broadening ( $\text{cm}^{-1} \pm 20 \text{ cm}^{-1}$ )	Assignment (mode)
1480	220	water libration
1642	38	free OH water bend
1765	57	strongly coordinated water bend
3203	55	strongly coordinated water OH stretch
3330	114	strongly coordinated water OH stretch
3450	83	companion OH stretch
3705	20	free OH stretch
3730	100	OH necessary for fit

TABLE 6. Frequencies, gaussian widths, and assignments of peaks from experimental *ssp* VSF spectra at incident angles 63° (visible) and 55° (IR).

Frequencies ( $\text{cm}^{-1} \pm 10 \text{ cm}^{-1}$ )	Gaussian Broadening ( $\text{cm}^{-1} \pm 20 \text{ cm}^{-1}$ )	Assignment (mode)
3203	55	strongly coordinated water OH stretch
3330	114	strongly coordinated water OH stretch
3450	83	companion OH stretch
3705	20	free OH stretch

TABLE 7. Frequencies, gaussian widths, and assignments of peaks from experimental *sps* VSF spectra at incident angles 63° (visible) and 55° (IR).

Frequencies ( $\text{cm}^{-1} \pm 10 \text{ cm}^{-1}$ )	Gaussian Broadening ( $\text{cm}^{-1} \pm 20 \text{ cm}^{-1}$ )	Assignment (mode)
1480	220	water libration
1622	38	free OH water bend
1765	57	strongly coordinated water bend

## APPENDIX B

### FITTING PARAMETERS FOR MEA STUDIES

The fitting parameters for 10 M MEA, 10 M EDA, and 10 M ETG; and 10 M MEA in *sps* are presented here, as discussed in Chapter V.

TABLE 8. Frequencies, gaussian widths, and assignments of peaks from experimental *ssp* VSF spectra of **10 M MEA** at incident angles 45° (visible) and 60° (IR).

Frequencies ( $\text{cm}^{-1} \pm 10 \text{ cm}^{-1}$ )	Gaussian Broadening ( $\text{cm}^{-1} \pm 20 \text{ cm}^{-1}$ )	Assignment (mode)
1250	100	hydroxyl OH deformation
1340	11	CH <sub>2</sub> wag
1412	22	CH <sub>2</sub> wag
1478	22	CH <sub>2</sub> bend/deformation
1480	250	water libration
1601	13	NH <sub>2</sub> bend
1641	33	free OH water bend
1760	57	strongly coordinated water OH bend
2846	28	SS-CH <sub>2</sub>
2875	23	SS-CH <sub>2</sub>
2910	70	AS-CH <sub>2</sub>
2936	24	AS-CH <sub>2</sub> or FR-CH <sub>2</sub>
3171	100	hydroxyl OH of MEA/strongly coord. water
3200	200	hydroxyl OH of MEA/strongly coord. water
3287	19	SS-NH <sub>2</sub>
3345	27	AS-NH <sub>2</sub>
3304	40	strongly coordinated water OH stretch
3699	120	large, OH stretches of hydroxyl and water

TABLE 9. Frequencies, gaussian widths, and assignments of peaks from experimental *ssp* VSF spectra of **10 M EDA** at incident angles 45° (visible) and 60° (IR).

Frequencies ( $\text{cm}^{-1} \pm 10 \text{ cm}^{-1}$ )	Gaussian Broadening ( $\text{cm}^{-1} \pm 20 \text{ cm}^{-1}$ )	Assignment (mode)
1250	100	hydroxyl OH deformation
1340	11	CH <sub>2</sub> wag
1412	27	CH <sub>2</sub> wag
1478	17	CH <sub>2</sub> bend/deformation
1480	250	water libration
1579	10	NH <sub>2</sub> bend
1601	13	NH <sub>2</sub> bend
1641	33	free OH water bend
1760	57	strongly coordinated water OH bend

TABLE 10. Frequencies, gaussian widths, and assignments of peaks from experimental *ssp* VSF spectra of **10 M ETG** at incident angles 45° (visible) and 60° (IR).

Frequencies ( $\text{cm}^{-1} \pm 10 \text{ cm}^{-1}$ )	Gaussian Broadening ( $\text{cm}^{-1} \pm 20 \text{ cm}^{-1}$ )	Assignment (mode)
1250	100	hydroxyl OH deformation
1340	11	CH <sub>2</sub> wag
1433	10	CH <sub>2</sub> wag
1487	22	CH <sub>2</sub> bend/deformation
1480	250	water libration
1641	33	free OH water bend
1760	57	strongly coordinated water OH bend

TABLE 11. Frequencies, gaussian widths, and assignments of peaks from experimental *sp<sub>s</sub>* VSF spectra of **10 M MEA** in CH region at incident angles 63° (visible) and 55° (IR).

Frequencies ( $\text{cm}^{-1} \pm 10 \text{ cm}^{-1}$ )	Gaussian Broadening ( $\text{cm}^{-1} \pm 20 \text{ cm}^{-1}$ )	Assignment (mode)
2846	25	SS-CH <sub>2</sub>
2875	20	SS-CH <sub>2</sub>
2910	25	AS-CH <sub>2</sub>
2936	24	AS-CH <sub>2</sub> or FR-CH <sub>2</sub>
3165	210	hydroxyl OH of MEA/strongly coord. water

## APPENDIX C

### FITTING PARAMETERS FOR CO<sub>2</sub> UPTAKE

The fitting parameters for 10 M MEA in CO<sub>2</sub>, as discussed in Chapter VII, are presented here. These parameters were determined from a global fit, and therefore apply to the fits to spectra taken during CO<sub>2</sub> after 3 hours and 15 hours, as well as post-CO<sub>2</sub> spectra.

TABLE 12. Frequencies, gaussian widths, and assignments of peaks from experimental *ssp* VSF spectra of **10 M MEA with CO<sub>2</sub>** at incident angles 45° (visible) and 60° (IR).

Frequencies (cm <sup>-1</sup> ±10 cm <sup>-1</sup> )	Gaussian Broadening (cm <sup>-1</sup> ±20 cm <sup>-1</sup> )	Assignment (mode)
1296	34	hydroxyl OH deformation
1345	43	CH <sub>2</sub> wag
1413	39	CH <sub>2</sub> wag
1430	10	CH <sub>2</sub> wag
1489	15	CH <sub>2</sub> bend/deformation
1563	28	amide II band
1641	24	free OH water bend
1760	59	strongly coordinated water OH bend
2781	126	RN-CH <sub>2</sub>
2855	10	SS-CH <sub>2</sub>
2870	34	SS-CH <sub>2</sub>
2910	50	AS-CH <sub>2</sub>
2923	25	AS-CH <sub>2</sub> or FR-CH <sub>2</sub>
3153	88	hydroxyl OH of MEA/strongly coord. water
3600	300	hydroxyl OH of MEA/coord. water
3650	156	hydroxyl OH of MEA/coord. water

## APPENDIX D

### DIHEDRAL MATCHES FROM MD TO DFT

The MD conformers' dihedral distributions were extracted from the simulations and matched to representative DFT structures. The optimized DFT structures correspond to peaks in the MD dihedral distributions. MEA has 18 DFT structures; MEH, 2; CBM, 15; and CBA, 56. Only the most populous conformers are listed for brevity.

TABLE 13. DFT structures and energies calculated at B3LYP/6-311++G(2d,2p) level of theory for  $\sim 10$  M MEA. Conformer ranges for MD simulations that matched the DFT structures.

MD Conformer	DFT Dihedral Angle ( $^{\circ}$ )				Dihedral Range ( $^{\circ}$ ) for MD Assignments			
	D1	D2	D3	D4	D1	D2	D3	D4
MEA1	-179.5	-68.7	-72.7	168.2	150–180	0–180	0–180	0–180
MEA10	57.9	-43.8	-163.6	77.1	30–90	0–60	150–180	30–90
MEA11	70.5	-172.6	-168.9	72.3	30–90	150–180	150–180	30–90
MEA13	60.3	-76.4	-64.6	56.9	30–90	30–90	30–90	30–90
MEA14	60.0	-177.6	-56.0	61.7	30–90	150–180	30–90	30–90
MEA15	58.2	71.1	-51.3	65.9	30–90	30–90	30–90	30–90
MEA16	63.1	71.9	-55.4	-174.6	30–90	30–90	30–90	150–180
MEA17	54.2	-72.6	-84.5	157.6	30–90	30–90	60–120	130–180
MEA18	64.8	-169.9	-60	-178.2	30–90	150–180	30–90	150–180

TABLE 14. DFT structures and energies calculated at B3LYP/6-311++G(2d,2p) level of theory for  $\sim 1$  M MEH. Conformer ranges for MD simulations that matched the DFT structures.

MD Conformer	DFT Dihedral Angle ( $^{\circ}$ )					Dihedral Range ( $^{\circ}$ ) for MD Assignments				
	D1	D2	D3	D4	D5	D1	D2	D3	D4	D5
MEH1	180	180	60.3	180	-60.3	90–180	90–180	0–180	30–180	0–150
MEH2	48.5	173.2	-169.3	-49	69.3	0–90	90–180	20–180	30–180	0–180



TABLE 15. DFT structures and energies calculated at B3LYP/6-311++G(2d,2p) level of theory for  $\sim 1$  M **CBM**. Conformer ranges for MD simulations that matched the DFT structures.

MD Conformer	DFT Dihedral Angle ( $^{\circ}$ )				Dihedral Range ( $^{\circ}$ ) for MD Assignments			
	D1	D2	D3	D4	D1	D2	D3	D4
CBM1	20.5	-112	-176	-169.4	90–180	60–180	90–180	90–180
CBM2	-22	87	-172	66	90–180	60–180	30–180	30–90
CBM3	23.3	-89	-54	44	90–180	60–180	0–90	30–90
CBM4	-25	154	-53	31.6	90–180	90–180	0–90	0–90
CBM15	5	-171	58.6	-24.9	90–180	90–180	30–90	90–180

TABLE 16. DFT structures and energies calculated at B3LYP/6-311++G(2d,2p) level of theory for  $\sim 1$  M **CBA**. Conformer ranges for MD simulations that matched the DFT structures.

MD Conformer	DFT Dihedral Angle ( $^{\circ}$ )					Dihedral Range ( $^{\circ}$ ) for MD Assignments				
	D1	D2	D3	D4	D5	D1	D2	D3	D4	D5
CBA42	8.6	-157.2	-59.4	175.8	-8	0–30	150–180	30–90	150–180	0–30
CBA46	8	-170.4	-56.3	-75.2	-10.1	0–30	150–180	30–90	30–90	0–30

## REFERENCES CITED

- [1] Zhou, S.; Wang, S.; Chen, C. *Ind. Eng. Chem. Res.* **2012**, *51*, 2539–2547.
- [2] Ciais, P.; Sabine, C.; Bala, G.; Bopp, L.; Brovkin, V.; Canadell, J.; Chhabra, A.; DeFries, R.; Galloway, J.; Heimann, M.; Jones, C.; Quere, C. L.; Myneni, R. B.; Piao, S.; Thornton, P. In *Climate Change 2013: The Physical Science Basis*; of Working Group I to the Fifth Assessment Report of the Intergovernmental Panel on Climate Change, C., Ed.; Cambridge University Press, Cambridge, United Kingdom and New York, NY, USA., 2013; Chapter 2013: Carbon and Other Biogeochemical Cycles.
- [3] Surampalli, R. Y., Zhang, T. C., Tyagi, R. D., Naidu, R., Gurjar, B. R., ojha, C. S. P., Yan, S., Brar, S. K., Ramakrishnan, A., Kao, C. M., Eds. *Carbon Capture and Storage*; American Society of Chemical Engineers: 1801 Alexander Bell Dr., Reston, VA 20191, 2015.
- [4] Metz, B.; Davidson, O.; De Coninck, H.; Loos, M.; Meyer, L. *IPCC Special Report on Carbon dioxide capture and storage*; 2005.
- [5] Administration, E. I. *International Energy Outlook*; U.S. Department of Energy, 2014.
- [6] Figueroa, J. D.; Fout, T.; Plasynski, S.; McIlvried, H.; Srivastava, R. D. *Int. J. Greenh. Gas Control* **2008**, *2*, 9–20.
- [7] Espinal, L.; Poster, D. L.; Wong-Ng, W.; Allen, A. J.; Green, M. L. *Environ. Sci. Technol.* **2013**, *47*, 11960–11975.
- [8] Administration, E. I. *Annual Energy Review 2011*; 2011.
- [9] Matthews, H. D.; Solomon, S. *Science* **2013**, *340*, 438–439.
- [10] Rochelle, G. T. *Science* **2009**, *325*, 1652–1654.
- [11] Blomen, E.; Hendriks, C.; Neele, F. *Energy Procedia* **2009**, *1*, 1505–1512.
- [12] McCann, N.; Maeder, M.; Hasse, H. *J. Chem. Thermodyn.* **2011**, *43*, 664–669.
- [13] Patiño-Echeverri, D.; Hoppock, D. C. *Environ. Sci. Technol.* **2012**, *46*, 1243–1252.
- [14] Lewis, T.; Faubel, M.; Winter, B.; Hemminger, J. C. *Angew. Chem. Int. Ed.* **2011**, *50*, 10178–10181.

- [15] Niedermaier, I.; Bahlmann, M.; Papp, C.; Kolbeck, C.; Wei, W.; Krick Calderón, S.; Grabau, M.; Schulz, P. S.; Wasserscheid, P.; Steinrück, H.-P.; Maier, F. *J. Am. Chem. Soc.* **2014**, *136*, 436–441.
- [16] Shao, R.; Stangeland, A. *Amines Used in CO<sub>2</sub> Capture*; 2009.
- [17] McWilliams, L. E.; Valley, N. A.; Wren, S. N.; Richmond, G. L. *Physical Chemistry Chemical Physics* **2015**, *17*, 21458–21469.
- [18] Yang, J.; Yu, X.; Yan, J.; Tu, S.-T.; Dahlquist, E. *Applied Energy* **2013**, *112*, 755–764.
- [19] Ota, S. T.; Richmond, G. L. *J. Am. Chem. Soc.* **2011**, *133*, 7497–7508.
- [20] Ota, S. T.; Richmond, G. L. *Journal of the American Chemical Society* **2012**, *134*, 9967–9977.
- [21] Lambert, A. G.; Davies, P. B.; Neivandt, D. J. *Appl. Spectrosc. Rev.* **2005**, *40*, 103–145.
- [22] Shen, Y. R. *J. Phys. Chem. C* **2012**, *116*, 15505–15509.
- [23] Eisenthal, K. B. *Chem. Rev.* **1996**, *96*, 1343–1360.
- [24] Morita, A.; Hynes, J. T. *Chem. Phys.* **2000**, *258*, 371–390.
- [25] Richmond, G. L. *Chem. Rev.* **2002**, *102*, 2693–2724.
- [26] Tian, C. S.; Shen, Y. R. *Chem. Phys. Lett.* **2009**, *470*, 1–6.
- [27] Hirose, C.; Akamatsu, N.; Domen, K. *J. Chem. Phys.* **1992**, *96*, 997–1004.
- [28] Hirose, C.; Yamamoto, H.; Akamatsu, N.; Domen, K. *J. Phys. Chem.* **1993**, *97*, 10064–10069.
- [29] Löbau, J.; Wolfrum, K. *JOSA B* **1997**, *14*, 2505–2512.
- [30] Lü, R.; Gan, W.; Wu, B.-H.; Chen, H.; Wang, H.-f. *J. Phys. Chem. B* **2004**, *108*, 7297–7306.
- [31] Xu, M.; Liu, D.; Allen, H. C. *Environ. Sci. Technol.* **2006**, *40*, 1566–1572.
- [32] Ishiyama, T.; Takahashi, H.; Morita, A. *Journal of Physics: Condensed Matter* **2012**, *24*, 124107.
- [33] Nagata, Y.; Mukamel, S. *Journal of the American Chemical Society* **2010**, *132*, 6434–6442.

- [34] Medders, G. R.; Paesani, F. *Journal of the American Chemical Society* **2016**, *138*, jacs.6b00893.
- [35] Mifflin, A. L.; Velarde, L.; Ho, J.; Psciuk, B. T.; Negre, C. F. A.; Ebben, C. J.; Upshur, M. A.; Lu, Z.; Strick, B. L.; Thomson, R. J.; Batista, V. S.; Wang, H.-f.; Geiger, F. M. *The Journal of Physical Chemistry A* **2015**, *119*, 1292–1302.
- [36] Chase, H. M.; Rudshiteyn, B.; Psciuk, B. T.; Upshur, M. A.; Strick, B. F.; Thomson, R. J.; Batista, V. S.; Geiger, F. M. *The Journal of Physical Chemistry B* **2016**, *120*, 1919–1927.
- [37] Ishiyama, T.; Sokolov, V. V.; Morita, A. *The Journal of Chemical Physics* **2011**, *134*, 024510.
- [38] Kessler, J.; Elgabarty, H.; Spura, T.; Karhan, K.; Partovi-Azar, P.; Hassanali, A. A.; Kühne, T. D. *The Journal of Physical Chemistry B* **2015**, *119*, 10079–10086.
- [39] Cendagorta, J. R.; Ichiye, T. *The Journal of Physical Chemistry B* **2015**, *119*, 9114–9122.
- [40] Han, B.; Zhou, C.; Wu, J.; Tempel, D. J.; Cheng, H. *The Journal of Physical Chemistry Letters* **2011**, *2*, 522–526.
- [41] Plath, K. L.; Valley, N. A.; Richmond, G. L. *J. Phys. Chem. A* **2013**, *117*, 11514–11527.
- [42] Rosen, M. J. *Surfactants and interfacial phenomena*; Wiley Online Library, 2004; Vol. 3.
- [43] Mitropoulos, A. C. *J Eng Sci Technol Rev* **2008**, *1*, 1–3.
- [44] Tyrode, E.; Johnson, C. M.; Baldelli, S.; Leygraf, C.; Rutland, M. W. *J. Phys. Chem. B* **2005**, *109*, 329–341.
- [45] Schwier, A. N.; Viglione, G. A.; Li, Z.; Faye McNeill, V. *Atmospheric Chemistry and Physics* **2013**, *13*, 10721–10732.
- [46] Banerjee, S.; Hassenklöver, E.; Kleijn, J. M.; Cohen Stuart, M. A.; Leermakers, F. A. M. *The Journal of Physical Chemistry B* **2013**, *117*, 8524–8535.
- [47] Wren, S. N.; Gordon, B. P.; Valley, N. A.; McWilliams, L. E.; Richmond, G. L. *The Journal of Physical Chemistry A* **2015**, *119*, 6391–6403.
- [48] Gan, W.; Wu, D.; Zhang, Z.; Feng, R.-r.; Wang, H.-f. *The Journal of Chemical Physics* **2006**, *124*, 114705.

- [49] Hore, D. K.; King, J. L.; Moore, F. G.; Alavi, D. S.; Hamamoto, M. Y.; Richmond, G. L. *Applied Spectroscopy* **2004**, *58*, 1377–1384.
- [50] Shrestha, M.; Zhang, Y.; Ebben, C. J.; Martin, S. T.; Geiger, F. M. *The Journal of Physical Chemistry A* **2013**, *117*, 8427–8436.
- [51] Benedict, W. S.; Plyler, E. K. *Journal of Research of the National Institutes of Standards and Technology* **1951**, *Research Paper 2194*, 246–265.
- [52] Hanssen, L. M.; Zhu, C. In *Wavenumber Standards for Mid-infrared Spectrometry*; Chalmers, J. M., Griffiths, P. R., Eds.; John Wiley & Sons Ltd., 2002; Chapter Calibration Procedures and Standards for Vibrational Spectroscopy, pp 1–9.
- [53] Yan, E. C. Y.; Wang, Z.; Fu, L. *The Journal of Physical Chemistry B* **2015**, *119*, 2769–2785.
- [54] Buchbinder, A. M.; Gibbs-Davis, J. M.; Stokes, G. Y.; Peterson, M. D.; Weitz, E.; Geiger, F. M. *The Journal of Physical Chemistry C* **2011**, *115*, 18284–18294.
- [55] Bonn, M.; Nagata, Y.; Backus, E. H. G. *Angewandte Chemie* **2015**, *127*, 5652–5669.
- [56] Bain, C. D.; Davies, P. B.; Ong, T. H.; Ward, R. N.; Brown, M. A. *Langmuir* **1991**, *7*, 1563–1566.
- [57] Moore, F. G.; Becraft, K. A.; Richmond, G. L. *Appl. Spectrosc.* **2002**, *56*, 1575–1578.
- [58] Raymond, E. A.; Tarbuck, T. L.; Brown, M. G.; Richmond, G. L. *J. Phys. Chem. B* **2003**, *107*, 546–556.
- [59] Raymond, E. A.; Tarbuck, T. L.; Richmond, G. L. *J. Phys. Chem. B* **2002**, *106*, 2817–2820.
- [60] Ostroverkhov, V.; Waychunas, G.; Shen, Y. *Phys. Rev. Lett.* **2005**, *94*, 046102.
- [61] Vinaykin, M.; Benderskii, A. V. *J. Phys. Chem. Lett.* **2012**, *3*, 3348–3352.
- [62] Woutersen, S.; Emmerichs, U.; Bakker, H. J. *Science* **1997**, *278*, 658–660.
- [63] Nienhuys, H.-K.; van Santen, R. A.; Bakker, H. J. *J. Chem. Phys.* **2000**, *112*, 8487.
- [64] Monson, P. R.; Patumtevapibal, S.; Kaufmann, K. J.; Robinson, G. W. *Chem. Phys. Lett.* **1974**, *28*, 312–315.

- [65] Chieffo, L.; Shattuck, J.; Amsden, J. J.; Erramilli, S.; Ziegler, L. D. *Chem. Phys.* **2007**, *341*, 71–80.
- [66] Blower, P. G.; Ota, S. T.; Valley, N. A.; Wood, S. R.; Richmond, G. L. *J. Phys. Chem. A* **2013**, *117*, 130802123816004.
- [67] Valley, N. A.; Blower, P. G.; Wood, S. R.; Plath, K. L.; McWilliams, L. E.; Richmond, G. L. *J. Phys. Chem. A* **2014**, *118*, 4778–4789.
- [68] Valley, N. A.; Robertson, E. J.; Richmond, G. L. *Langmuir* **2014**, *30*, 14226–14233.
- [69] Wren, S. N.; Valley, N. A.; Gordon, B. P.; McWilliams, L. E.; Richmond, G. L. *J. Phys. Chem. A* **2015**, *119*, 6391–6403.
- [70] Malony, A. MRI-R2: Acquisition of an Applied Computational Instrument for Scientific Synthesis (ACISS). NSF Grant OCI-0960354.
- [71] Case, D. A. et al. AMBER 12. University of California, San Francisco, 2012.
- [72] Martinez, L.; Andrade, R.; Birgin, E.; Martinez, J. *J. Comput. Chem.* **2009**, *30*, 2157–2164.
- [73] Caldwell, J. W.; Kollman, P. A. *The Journal of Physical Chemistry* **1995**, *99*, 6208–6219.
- [74] Valiev, M.; Bylaska, E. J.; Govind, N.; Kowalski, K.; Straatsma, T. P.; van Dam, H. J. J.; Wang, D.; Nieplocha, J.; Apra, E.; Windus, T. L.; de Jong, W. A. *Comput. Phys. Commun.* **2010**, *181*, 1477–1489.
- [75] Frisch, M. J. et al. Gaussian 09 Revision D.01. Gaussian Inc. Wallingford, CT 2009.
- [76] Gangarapu, S.; Marcelis, A. T. M.; Zuilhof, H. *ChemPhysChem* **2013**, *14*, 3936–3943.
- [77] Biczysko, M.; Panek, P.; Scalmani, G.; Bloino, J.; Barone, V. *J. Chem. Theory Comput.* **2010**, *6*, 2115–2125.
- [78] Barone, V.; Biczysko, M.; Bloino, J. *Phys. Chem. Chem. Phys.* **2014**, *16*, 1759–1787.
- [79] Carnimeo, I.; Puzzarini, C.; Tasinato, N.; Stoppa, P.; Charmet, A. P.; Biczysko, M.; Cappelli, C.; Barone, V. *J. Chem. Phys.* **2013**, *139*, 074310.
- [80] Davies, J. T.; Rideal, E. K. *Interfacial Phenomena*, 2nd ed.; Academic Press: New York, 1963.

- [81] Du, Q.; Superfine, R.; Freysz, E.; Shen, Y. *Physical Review Letters* **1993**, *70*, 2313–2316.
- [82] Verreault, D.; Hua, W.; Allen, H. C. *The Journal of Physical Chemistry Letters* **2012**, *3*, 3012–3028.
- [83] Nagata, Y.; Hsieh, C.-S.; Hasegawa, T.; Voll, J.; Backus, E. H. G.; Bonn, M. *J. Phys. Chem. Lett.* **2013**, *4*, 1872–1877.
- [84] Ni, Y.; Skinner, J. L. *The Journal of Chemical Physics* **2015**, *143*, 014502.
- [85] Imoto, S.; Xantheas, S. S.; Saito, S. *The Journal of Physical Chemistry B* **2015**, *119*, 11068–11078.
- [86] Walker, D. S.; Richmond, G. L. *The Journal of Physical Chemistry C* **2007**, *111*, 8321–8330.
- [87] Sulpizi, M.; Salanne, M.; Sprik, M.; Gaigeot, M.-P. *The Journal of Physical Chemistry Letters* **2013**, *4*, 83–87.
- [88] Ishiyama, T.; Imamura, T.; Morita, A. *Chemical Reviews* **2014**, *114*, 8447–8470.
- [89] Vargaftik, N. B.; Volkov, B. N.; Voljak, L. D. *J. Phys. Chem. Ref. Data* **1983**, *12*, 817–820.
- [90] Auer, B. M.; Skinner, J. L. *The Journal of Physical Chemistry B* **2009**, *113*, 4125–4130.
- [91] Auer, B. M.; Skinner, J. L. *The Journal of Chemical Physics* **2008**, *129*, 214705.
- [92] Shen, Y. R.; Ostroverkhov, V. *Chemical Reviews* **2006**, *106*, 1140–1154.
- [93] Walker, D. S.; Hore, D. K.; Richmond, G. L. *The Journal of Physical Chemistry B* **2006**, *110*, 20451–20459.
- [94] Feng, R.-r.; Guo, Y.; Lü, R.; Velarde, L.; Wang, H.-f. *J. Phys. Chem. A* **2011**, *115*, 6015–6027.
- [95] Nihonyanagi, S.; Ishiyama, T.; Lee, T.-k.; Yamaguchi, S.; Bonn, M.; Morita, A.; Tahara, T. *Journal of the American Chemical Society* **2011**, *133*, 16875–16880.
- [96] Hsieh, C.-S.; Okuno, M.; Hunger, J.; Backus, E. H. G.; Nagata, Y.; Bonn, M. *Angewandte Chemie International Edition* **2014**, *53*, 8146–8149.
- [97] Nihonyanagi, S.; Kusaka, R.; Inoue, K.-i.; Adhikari, A.; Yamaguchi, S.; Tahara, T. *Journal of Chemical Physics* **2015**, *143*, 124707–124707.
- [98] Falk, M. *Spectrochimica Acta Part A: Molecular Spectroscopy* **1984**, *40*, 43–48.

- [99] Finlayson-Pitts, B. J.; Pitts, J. N. *Chemistry of the Upper and Lower Atmosphere*; Academic Press, 2000.
- [100] Boniface, J.; Shi, Q.; Li, Y. Q.; Cheung, J. L.; Rattigan, O. V.; Davidovits, P.; Worsnop, D. R.; Jayne, J. T.; Kolb, C. E. *The Journal of Physical Chemistry A* **2000**, *104*, 7502–7510.
- [101] Tarbuck, T. L.; Richmond, G. L. *Journal of the American Chemical Society* **2006**, *128*, 3256–3267.
- [102] Shamay, E. S.; Johnson, K. E.; Richmond, G. L. *The Journal of Physical Chemistry C* **2011**, *115*, 25304–25314.
- [103] Kumar, P. P.; Kalinichev, A. G.; Kirkpatrick, R. J. *The Journal of Physical Chemistry B* **2009**, *113*, 794–802.
- [104] Eklund, L.; Hofer, T. S.; Pribil, A. B.; Rode, B. M.; Persson, I. *Dalton Transactions* **2012**, *41*, 5209.
- [105] Hwang, G. S.; Stowe, H. M.; Paek, E.; Manogaran, D. *Physical Chemistry Chemical Physics* **2015**, *17*, 831–839.
- [106] Han, B.; Sun, Y.; Fan, M.; Cheng, H. *J. Phys. Chem. B* **2013**, *117*, 5971–5977.
- [107] Xie, H.-B.; Zhou, Y.; Zhang, Y.; Johnson, J. K. *The Journal of Physical Chemistry A* **2010**, *114*, 11844–11852.
- [108] Shim, J.-G.; Kim, J.-H.; Jhon, Y. H.; Kim, J.; Cho, K.-H. *Ind. Eng. Chem. Res.* **2009**, *48*, 2172–2178.
- [109] Vázquez, G.; Alvarez, E.; Navaza, J. M.; Rendo, R.; Romero, E. *J. Chem. Eng. Data* **1997**, *42*, 57–59.
- [110] Jayarathna, S. A.; Jayarathna, C. K.; Kottage, D. A.; Dayarathna, S.; Eimer, D. A.; Melaaen, M. C. *J. Chem. Eng. Data* **2013**, *58*, 343–348.
- [111] Jayarathna, S. A.; Weerasooriya, A.; Dayarathna, S.; Eimer, D. A.; Melaaen, M. C. *J. Chem. Eng. Data* **2013**, *58*, 986–992.
- [112] Lv, B.; Guo, B.; Zhou, Z.; Jing, G. *Environmental Science & Technology* **2015**, *49*, 10728–10735.
- [113] Lin, C.-C.; Liu, W.-T.; Tan, C.-S. *Ind. Eng. Chem. Res.* **2003**, *42*, 2381–2386.
- [114] Yu, C.-H. *Aerosol Air Qual. Res.* **2012**, *12*, 745–769.
- [115] Knop, S.; Lindner, J.; Vöhringer, P. *Z. Phys. Chem.* **2011**, *225*, 913–926.



- [116] Jackson, P.; Robinson, K.; Puxty, G.; Attalla, M. *Energy Procedia* **2009**, *1*, 985–994.
- [117] Samarakoon, P. A. G. L.; Andersen, N. H.; Perinu, C.; Jens, K.-J. *Energy Procedia* **2013**, *37*, 2002–2010.
- [118] da Silva, E. F.; Kuznetsova, T.; Kvamme, B.; Merz, K. M. *J. Phys. Chem. B* **2007**, *111*, 3695–3703.
- [119] Richner, G.; Puxty, G. *Ind. Eng. Chem. Res.* **2012**, *51*, 14317–14324.
- [120] Socrates, G. *Infrared and Raman Characteristic Group Frequencies: Tables and Charts*, 3rd ed.; John Wiley & Sons: Chichester, West Sussex, England, 2001.
- [121] Kubelka, J.; Keiderling, T. A. *J. Phys. Chem. A* **2001**, *105*, 10922–10928.
- [122] Torii, H.; Tatsumi, T.; Tasumi, M. *J. Raman. Spectrosc.* **1998**, *29*, 537–546.
- [123] Grahnen, J. A.; Amunson, K. E.; Kubelka, J. *J. Phys. Chem. B* **2010**, *114*, 13011–13020.
- [124] Bougie, F.; Iliuta, M. C. *J. Chem. Eng. Data* **2014**, *59*, 355–361.
- [125] Hilliard, M. D. A predictive thermodynamic model for an aqueous blend of potassium carbonate, piperazine, and monoethanolamine for carbon dioxide capture from flue gas. Ph.D. thesis, University of Texas at Austin, 2008.
- [126] Weiland, R. H.; Dingman, J. C.; Cronin, D. B.; Browning, G. J. *J. Chem. Eng. Data* **1998**, *43*, 378–382.
- [127] Amundsen, T. G.; Øi, L. E.; Eimer, D. A. *J. Chem. Eng. Data* **2009**, *54*, 3096–3100.
- [128] Chacon, E.; Tarazona, P. *Phys. Rev. Lett.* **2003**, *91*, 166103.
- [129] Jorge, M.; Jedlovszky, P.; Cordeiro, M. N. D. S. *J. Phys. Chem. C* **2010**, *114*, 11169–11179.
- [130] Jorge, M.; Hantal, G.; Jedlovszky, P.; Cordeiro, M. N. D. S. *J. Phys. Chem. C* **2010**, *114*, 18656–18663.
- [131] Pártay, L. B.; Jedlovszky, P.; Vincze, Á.; Horvai, G. *J. Phys. Chem. B* **2008**, *112*, 5428–5438.
- [132] Willard, A. P.; Chandler, D. *J. Phys. Chem. B* **2010**, *114*, 1954–1958.
- [133] Bian, H.-t.; Feng, R.-r.; Xu, Y.-y.; Guo, Y.; Wang, H.-f. *Phys. Chem. Chem. Phys.* **2008**, *10*, 4920.

- [134] Hua, W.; Chen, X.; Allen, H. C. *J. Phys. Chem. A* **2011**, *115*, 6233–6238.
- [135] Brown, M. G.; Walker, D. S.; Raymond, E. A.; Richmond, G. L. *J. Phys. Chem. B* **2003**, *107*, 237–244.
- [136] Roy, S.; Gruenbaum, S. M.; Skinner, J. L. *J. Chem. Phys.* **2014**, *141*, 22D505.
- [137] Abel, B. *Annu. Rev. Phys. Chem.* **2013**, *64*, 533–552.
- [138] Levering, L. M.; Sierra-Hernández, M. R.; Allen, H. C. *The Journal of Physical Chemistry C* **2007**, *111*, 8814–8826.
- [139] Tarbuck, T. L.; Ota, S. T.; Richmond, G. L. *Journal of the American Chemical Society* **2006**, *128*, 14519–14527.
- [140] Blower, P. G.; Ota, S. T.; Valley, N. A.; Wood, S. R.; Richmond, G. L. *The Journal of Physical Chemistry A* **2013**, *117*, 7887–7903.
- [141] Blower, P. G.; Shamay, E.; Kringle, L.; Ota, S. T.; Richmond, G. L. *The Journal of Physical Chemistry A* **2013**, *117*, 2529–2542.
- [142] Marsh, A. R. W.; McElroy, W. J. *Atmospheric Environment* **1985**, *19*, 1075–1080.
- [143] dos Santos, A. P.; Levin, Y. *The Journal of Chemical Physics* **2010**, *133*, 154107–5.
- [144] Robertson, E. J.; Richmond, G. L. *Langmuir* **2013**, *29*, 10980–10989.
- [145] Souchon, V.; Aleixo, M. d. O.; Delpoux, O.; Sagnard, C.; Mougín, P.; Wender, A.; Raynal, L. *Energy Procedia* **2011**, *4*, 554–561.
- [146] Leroy, P.; Lassin, A.; Azaroual, M.; Andre, L. *Geochimica et Cosmochimica Acta* **2010**, *74*, 5427–5442.
- [147] Conway, W.; Wang, X.; Fernandes, D.; Burns, R.; Lawrance, G.; Puxty, G.; Maeder, M. *J. Phys. Chem. A* **2011**, *115*, 14340–14349.
- [148] Chakraborty, A. K.; Bischoff, K. B.; Astarita, G.; Damewood, J. R. *J. Am. Chem. Soc.* **1988**, *110*, 6947–6954.
- [149] Sartori, G.; Savage, D. W. *Ind. Eng. Chem. Fundam.* **1983**, *22*, 239–249.
- [150] McCann, N.; Phan, D.; Wang, X.; Conway, W.; Burns, R.; Attalla, M.; Puxty, G.; Maeder, M. *J. Phys. Chem. A* **2009**, *113*, 5022–5029.
- [151] Arstad, B.; Blom, R.; Swang, O. *The Journal of Physical Chemistry A* **2007**, *111*, 1222–1228.

- [152] García-Abuín, A.; Gómez-Díaz, D.; López, A. B.; Navaza, J. M.; Rumbo, A. *Industrial & Engineering Chemistry Research* **2013**, *52*, 13432–13438.
- [153] da Silva, E. F.; Svendsen, H. F. *Industrial & Engineering Chemistry Research* **2004**, *43*, 3413–3418.
- [154] Maier, F. *Angew. Chem. Int. Ed.* **2011**, *50*, 10133–10134.
- [155] Bhatnagar, S. S. *The Journal of Physical Chemistry* **1920**, 716–735.
- [156] Masterton, W. L.; Bianchi, J. *The Journal of Physical ...* **1963**, 615–618.
- [157] Ye, S.; Li, H.; Yang, W.; Luo, Y. *Journal of the American Chemical Society* **2014**, *136*, 1206–1209.
- [158] Wang, Z.; Morales-Acosta, M. D.; Li, S.; Liu, W.; Kanai, T.; Liu, Y.; Chen, Y.-N.; Walker, F. J.; Ahn, C. H.; Leblanc, R. M.; Yan, E. C. Y. *Chemical Communications* **2016**, *52*, 2956–2959.
- [159] Stuart, B. *Infrared spectroscopy*. John Wiley & Sons, Ltd., 2005.
- [160] Schäfer, T.; Kandratsenka, A.; Vöhringer, P.; Schroeder, J.; Schwarzer, D. *Physical Chemistry Chemical Physics* **2012**, *14*, 11651.
- [161] Perez-Blanco, M. E.; Maginn, E. J. *The Journal of Physical Chemistry B* **2010**, *114*, 11827–11837.
- [162] Perez-Blanco, M. E.; Maginn, E. J. *The Journal of Physical Chemistry B* **2011**, *115*, 10488–10499.
- [163] Yang, J.; Yu, X.; Yan, J.; Tu, S.-T.; Dahlquist, E. *Applied Energy* **2013**, *112*, 755–764.
- [164] Broder, J. M. *The New York Times* **2010**,
- [165] Gao, J.; Wang, S.; Wang, J.; Cao, L.; Tang, S.; Xia, Y. *International Journal of Greenhouse Gas Control* **2015**, *37*, 38–45.
- [166] Scholes, C. A.; Smith, K. H.; Kentish, S. E.; Stevens, G. W. *International Journal of Greenhouse Gas Control* **2010**, *4*, 739–755.
- [167] Krebs, T.; Nathanson, G. M. *Proceedings of the National Academy of Sciences* **2010**, *107*, 6622–6627.
- [168] Beyad, Y.; Burns, R.; Puxty, G.; Maeder, M. *Energy Procedia* **2013**, *37*, 1262–1266.
- [169] Khoma, R. E.; Shestaka, A. A.; Gel'mbol'dt, V. O. *Russ. J. Appl. Chem.* **2012**, *85*, 1667–1675.

- [170] Ishiyama, T.; Morita, A. *The Journal of Physical Chemistry C* **2011**, *115*, 13704–13716.
- [171] Hua, W.; Verreault, D.; Allen, H. C. *Journal of the American Chemical Society* **2015**, *137*, 13920–13926.
- [172] Brittain, H. G. *Profiles of Drug Substances, Excipients and Related Methodology: Critical Compilation of  $pK_a$  values for Pharmaceutical Substances*; Academic Press, 2007; Vol. 33.